SEDIMENT CONSOLIDATION AND PERMEABILITY AT THE CENTRAL OREGON MARGIN, OCEAN DRILLING PROGRAM SITES 891 AND 892

William Geoffrey Douglas Gray

Submitted in Partial Fulfilment of the Requirements
for the Degree of Bachelor of Science
Department of Earth Sciences
Dalhousie University, Halifax, Nova Scotia
March 1994

Dalhousie University

Department of Earth Sciences
Halifax, Nova Scotia
Canada B3H 3J5
(902) 494-2358
FAX (902) 494-6889

DATE February 13, 1995

AUTHOR William Geoffrey Douglas Gray

TITLE Sediment Consolidation and Permeability at the Central Oregon Margin, Ocean Drilling Program Sites 891 and 892

Degree B.Sc. (Adv. Major) Convocation May Year 1995

Permission is herewith granted to Dalhousie University to circulate and to have copied for non-commercial purposes, at its discretion, the above title upon the request of individuals or institutions.

Distribution License

DalSpace requires agreement to this non-exclusive distribution license before your item can appear on DalSpace.

NON-EXCLUSIVE DISTRIBUTION LICENSE

You (the author(s) or copyright owner) grant to Dalhousie University the non-exclusive right to reproduce and distribute your submission worldwide in any medium.

You agree that Dalhousie University may, without changing the content, reformat the submission for the purpose of preservation.

You also agree that Dalhousie University may keep more than one copy of this submission for purposes of security, back-up and preservation.

You agree that the submission is your original work, and that you have the right to grant the rights contained in this license. You also agree that your submission does not, to the best of your knowledge, infringe upon anyone's copyright.

If the submission contains material for which you do not hold copyright, you agree that you have obtained the unrestricted permission of the copyright owner to grant Dalhousie University the rights required by this license, and that such third-party owned material is clearly identified and acknowledged within the text or content of the submission.

If the submission is based upon work that has been sponsored or supported by an agency or organization other than Dalhousie University, you assert that you have fulfilled any right of review or other obligations required by such contract or agreement.

Dalhousie University will clearly identify your name(s) as the author(s) or owner(s) of the submission, and will not make any alteration to the content of the files that you have submitted.

If you have questions regarding this license please contact the repository manager at dalspace@dal.ca.

Grant the distribution license by signing and dating below.

______________________________	______________________________
Name of signatory	Date

ABSTRACT

Sediment hydraulic conductivity is a critical and highly variable control on the consolidation of accretionary prism materials. The consolidation state and pore pressure conditions within an accretionary prism ultimately determine its geometry and rate of deformation. This study uses back-pressured consolidometer and flow-pump permeameter testing with Shipboard physical property data to provide *in situ* hydraulic conductivity values for Ocean Drilling Program (ODP) Sites 891 and 892. These data augment a very limited data set for accretionary prism material and improve understanding of prism water budgets. Results from this study indicate an *in situ* hydraulic conductivity range of 10^{-5} to 10^{-7} cm/s for sediments at the central Oregon portion of the Cascadia convergent margin. These low hydraulic conductivities are insufficient to dissipate excess pore pressures developed within underthrust sediments at this location. This study identifies excess pore pressures in the range of 2.5 to 4.5 MPa for underthrust sediment. These findings support models that rank tectonic loading, rather than tectonic compression, as the largest influence on overpressuring. Excess pore pressures of this magnitude indicate a high potential for sediment failure, such as fold and fault formation, and thus, deformation early in accretion history.

Key Words: Cascadia margin, accretionary prism, ODP, hydraulic conductivity, consolidation, overconsolidation ratio, excess pore pressure

DEDICATION

This thesis is dedicated in memory of Robert Stevens, born at Ox Narrows,
Ontario, in the year of "the big snow", approximately 100 years ago.

He was known to nearly everyone, related or not, simply as Uncle Bob.

His love of the ancient lakes and hills of the Canadian
Shield introduced me to the wonders of the earth,
starting me on my path towards the study of geology.

Remaining unheeded, however, is his advice to
"forget looking at the ground, the future's in the sky".

TABLE OF CONTENTS

CHAPTER 1: INTRODUCTION

CHAPTER 2: REGIONAL GEOLOGY

CHAPTER 3: THEORY AND METHODOLOGY

CHAPTER 4: RESULTS AND OBSERVATIONS

CHAPTER 5: INTERPRETATION AND DISCUSSION

CHAPTER 6: CONCLUSIONS

TABLE OF FIGURES

TABLE OF TABLES

Acknowledgements

This study was initiated on the encouragement of Kate Moran. I am grateful for her confidence in my ability to complete the study, for her advice and support, and for access to her personal library and resources. Kate Jarrett provided invaluable assistance in the laboratory, as well as advice on analysis of data. Kevin MacKillop generously shared his experience in this area as well. I would like to thank the employees of the Bedford Institute of Oceanography for access to laboratory, library and computing resources there. Dr. D.B. Clarke of Dalhousie University guided construction of this manuscript, while my peers there encouraged its completion. Special thanks to V.C. DeWolfe and E.W. Pearson. Gratefully acknowledged is the ongoing emotional and financial support of my family, which made my studies at Dalhousie possible.

CHAPTER 1: INTRODUCTION

1.1 INTRODUCTION

The Ocean Drilling Program is an international consortium of government and educational institutions that employ the drillship *JOIDES Resolution* to address earth science objectives. The four major research themes of the Ocean Drilling Program (ODP) are paleoceanography, sedimentary and geochemical processes, studies of the lithosphere, and tectonics.

Towards this latter theme, the shipboard scientists of ODP Leg 146 set out to investigate one aspect of tectonics: the interaction of convergence, sediment deformation, and fluid flow. The Cascadia convergent margin, located along the Pacific Northwest region of North America (Fig. 1.1), is the study area chosen for Leg 146.

Lithospheric plate boundaries, such as the Cascadia margin, are the most dynamic tectonic environments on earth. These boundaries are of three types: divergent margins, transform margins, and convergent margins. Linear belts of mountains and trenches, volcanic and plutonic igneous activity, and large wedges of deformed and faulted sediments characterize convergent margins. Gaining insight into the nature of fluid flow within these sediment wedges was the focus of Leg 146.

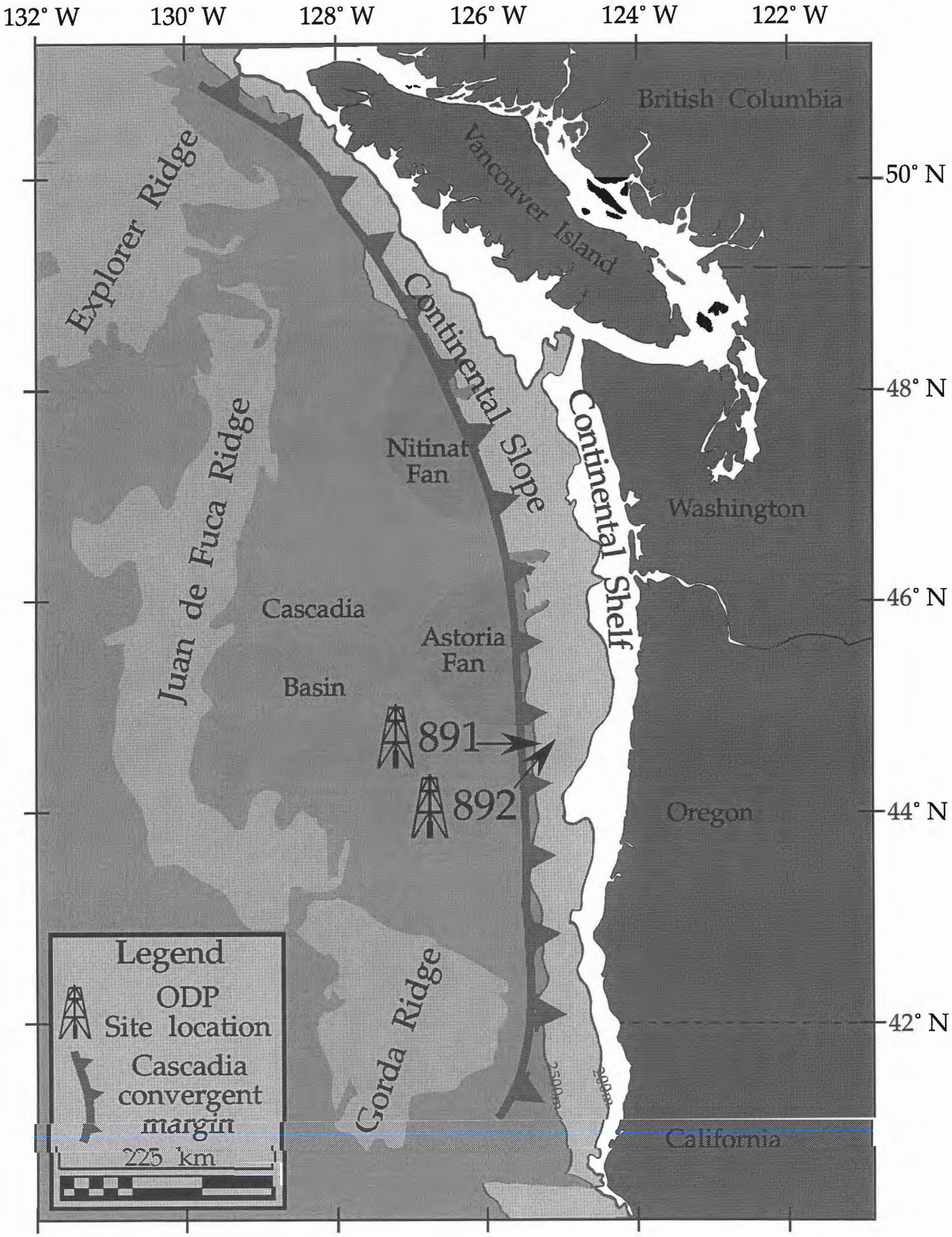

FIGURE 1.1. Location of study area, off central Oregon, showing submarine ridge spreading centres and the Cascadia convergent margin. Site 891 lies at the base of the continental slope. Site 892 lies on the continental slope.

1.2 LOCATION OF STUDY AREA

The Cascadia convergent margin lies along western North America, between northern California and central British Columbia (Fig. 1.1). The nature of fluid flow within the margin sediments appears to differ between the region off Vancouver Island, and the region off central Oregon (Davis et al. 1990, Kulm et al. 1986). Consequently, Leg 146 investigated both regions. This study, however, only concerns two cored locations, Sites 891 and 892 (Fig. 1.1), in the central Oregon margin.

Near Sites 891 and 892, the continental slope off Oregon has a width of approximately 50 km, increasing northwards along the margin. Site 891 lies at the base of the continental slope, on the westernmost ridge of the Oregon margin (Fig. 1.2), at a depth of 2663 metres below sea level (mbsl). Site 892 lies near the crest of the second ridge of the Oregon margin (Fig. 1.2), at a depth of 670 mbsl. The relief of the bathymetry in the study area is high, and is punctuated by the presence of two ridges, known to be anticlinal (MacKay et al. 1992).

1.3 REGIONAL OVERVIEW

The Cascadia margin is the zone of convergence between North America and ocean crust produced at three seafloor spreading ridges, the Explorer Ridge, the Gorda Ridge, and the Juan de Fuca Ridge (Fig. 1.1).

Convergence at this margin transports sediments deposited in the

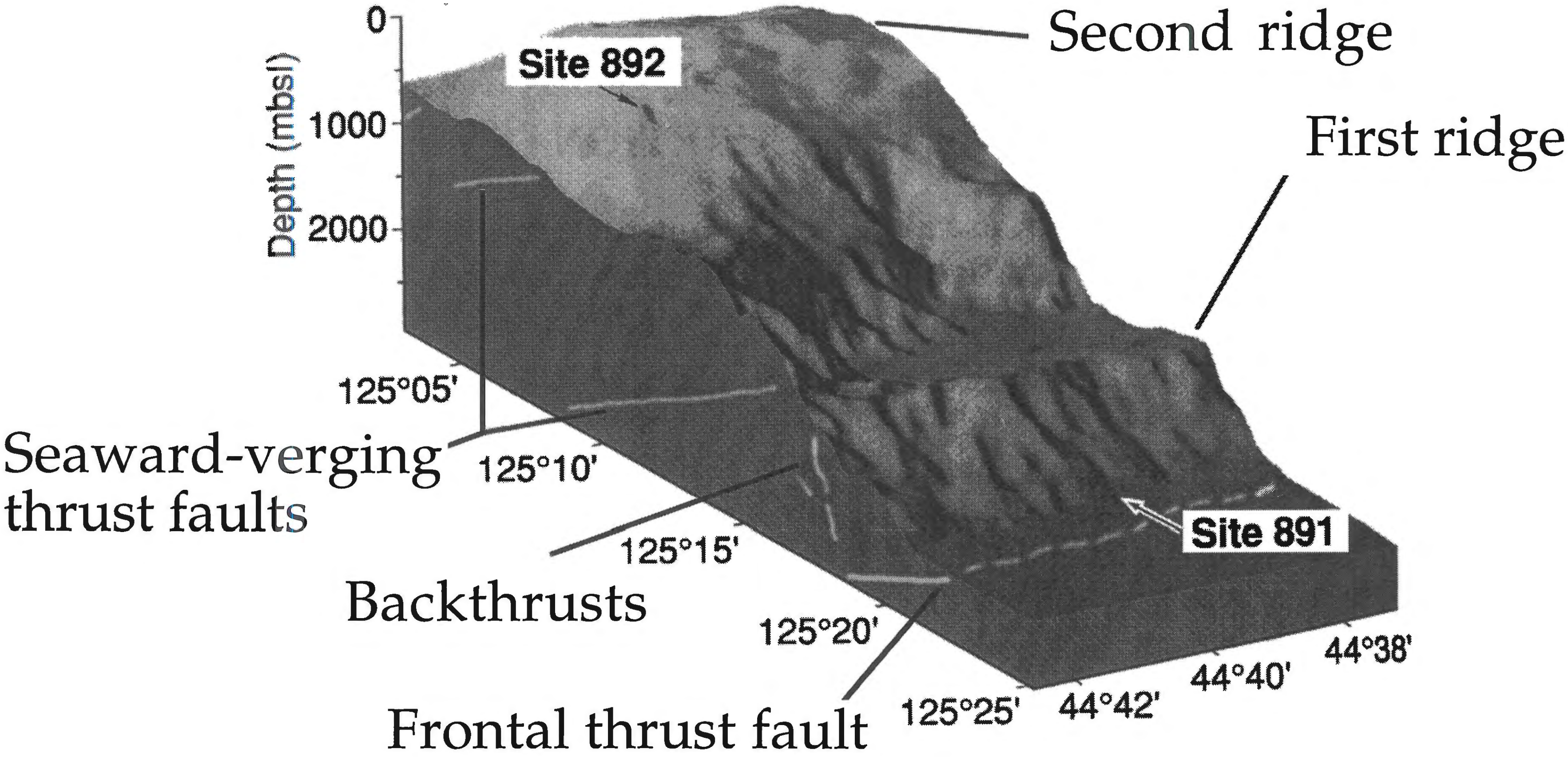

FIGURE 1.2. Shaded-relief bathymetry of the study area. Labeled are the locations of the first and second ridges. ODP Site 891 is located at the base of the first ridge, and Site 892 is located near the top of the second ridge, as shown. Overlain are the approximate locations of the frontal thrust fault and several backthrusts near the first ridge. Also shown are other seaward-verging thrust faults. Depth is in metres below sea level. Viewing perspective is from the northwest. (after Cochrane et al. 1994)

Cascadia basin (Fig. 1.1) towards the North American continental margin, where they accumulate in a sediment wedge known as an accretionary prism. The convergence causes deformation and tectonic consolidation in the sediments (Carson 1977). Several factors govern the processes of deformation and consolidation, but among the most important is the rate of expulsion of pore fluids (MacKay et al. 1992).

1.4 FLUIDS IN SEDIMENTS

Fluids are present within sediments as both interstitial fluids, occupying pore spaces between sediment particles, and as a component of hydrated mineral structures, such as clays. As a result of the relatively incompressible nature of liquids, the rate of fluid expulsion from sediments is a factor governing their deformation. At convergent margins, the expulsion of interstitial fluid, including fluid liberated during dehydration reactions of hydrated minerals, is evident from direct and indirect observations.

Direct observations of fluid flow include seafloor vents discharging fluid and seafloor mud volcanoes. These surficial features are commonly spatially related to anomalous or disrupted geothermal gradients within boreholes, compaction of sedimentary units seen in seismic sections, and pore-fluid chemical anomalies. Pore-fluid chemistry may also indicate the fluid source region, as water liberated during dehydration reactions contains no dissolved ions, whereas interstitial fluids contain dissolved ions, with levels tending to increase with residency time.

Although the above observations provide evidence for the existence of fluid expulsion and flow within sediments at convergent margins, the capacity for these sediments to transmit fluid, known as their intrinsic permeability, is unknown. The coefficient of intrinsic permeability is a property of a porous medium, dependent on the amount, size, shape, and inter-relationship of void spaces. In practice, measuring intrinsic permeability requires accounting for the density and viscosity of the fluids flowing through a known cross-sectional area of sediment. This property, which combines the nature of the fluid and the medium, is known as hydraulic conductivity, and it is measured in M^3/day/M. Commonly, hydraulic conductivity is referred to simply as permeability.

The hydraulic conductivity of a sediment governs fluid expulsion rates, and these in turn govern consolidation and deformation rates (MacKay et al. 1992). ODP Leg 146 directly measured hydraulic conductivity at one site by means of a borehole packer test. This test was a major accomplishment, however, as these tests are technically challenging and expensive at ocean floor depths. As a result, the seafloor permeability data set is very limited . This study provides permeability values for three samples of sediment cored within the Cascadia margin, using laboratory consolidation and flow-pump permeameter tests. These results complement the shipboard data set resulting from extensive physical, geochemical, and geophysical tests performed during the Leg. These data address the primary goals of Leg 146, which were to determine the mechanisms and relative importance of dispersed fluid flow, which travels through the sediment matrix, and focused fluid flow, which exploits fractures in the sediment. By providing quantitative constraints to fluid flow, Leg 146 also sought insight into the physical and chemical nature of gas clathrate (hydrate) zones.

1.5 PURPOSE OF STUDY

For some time, it has been suggested that pore fluids play an important role in sediment wedge and accretionary prism deformation (Hubbert and Rubey 1959, Davis et al. 1983), particularly with regards to the wedge geometry and critical angles. The extent of the role pore fluids play is still, however, not fully understood (Langseth and Moore 1991). Realistic modelling of accretionary prism deformational behaviour requires knowledge of pore-fluid expulsion and migration, on which an important constraint is sediment permeability. However, published data on permeability characteristics of deep-sea and accretionary prism sediments are limited (Clukey and Silva 1982, Taylor and Fisher 1993). Providing both calculated and measured permeability data for Cascadia margin accretionary prism sediments is one purpose of this study. These data supplement the limited database of deep-sea permeability values. As well, tectonic stresses within accretionary prism sediments can result in permeability characteristics different from those of other deep-sea materials. Data from this study allows tighter constraints to be placed upon the modelling of pore-fluid pressures and expulsion, and the relative importance of dispersed and focused fluid flow within the Cascadia margin.

Additionally, this study provides overconsolidation ratios for three samples from the Cascadia margin. The overconsolidation ratio (OCR) is the ratio of the preconsolidation stress, or the maximum past stress, to the existing vertical effective overburden stress (Holtz and Kovacs 1981). These data, coupled with the permeability data, provide insight into the rates of fluid flow and deformation at the Cascadia margin, as sediments that are relatively impermeable tend to develop low OCR's if subject to tectonic stresses.

1.6 SCOPE OF STUDY

The central Oregon portion of the Cascadia convergent margin displays structural features and active fluid venting at faults (MacKay et al. 1992) not found universally throughout the margin. These suggest different conditions here than elsewhere in this margin. The scope of this thesis, therefore, is limited to the central Oregon margin. However, the permeability data, and the relationship between measured and calculated permeabilities, will be of more general application.

This thesis deals primarily with sample physical index properties, consolidation behaviour and hydraulic conductivity. Use in this study of geophysical and geochemical data from Ocean Drilling Program shipboard testing is only to support interpretations resulting from physical property and laboratory data.

1.7 ORGANIZATION

The first two chapters of this study introduce the purpose of the study, the location of the study area, and the regional geology. Chapter 3 provides details of the theory and methodology of the laboratory procedures used. The fourth chapter presents results from shipboard tests, and consolidation and permeability tests performed at the Bedford Institute of Oceanography. The fifth chapter provides discussion and interpretation of these results. Chapter 6 summarizes the conclusions and suggests further research directions.

CHAPTER 2: REGIONAL GEOLOGY

2.1 INTRODUCTION

Accretionary prisms consist of material transferred from an underthrusting plate to an overthrusting plate at a convergent margin (Moore and Langseth 1986). In this study, the process of accretion at the base of the margin slope in a zone of convergence is known as offscraping, and the material accreted in this manner is called offscraped, following the usage of Scholl et al. (1980) (Fig. 2.1)

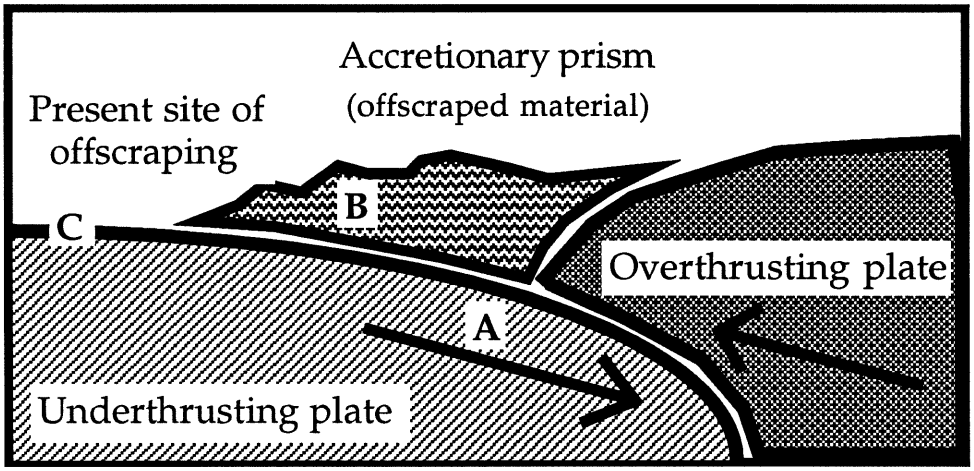

FIGURE 2.1. Simple diagram illustrating the major components of accretionary prism geometry. Material at point B was incorporated into the prism, by offscraping, from an original position at point A. Material at point C will become incorporated into the prism in the future.

Offscraped sediments in the Cascadia margin contain a relatively large component of coarse-grained terrigenous clastic material (Scheidegger et al. 1984). This terrigenous input does not occur in all accretionary prisms. For example, the northern Barbados Ridge accretionary prism consists primarily of fine-grained pelagic and hemipelagic sediment, whereas the Guatemala and Mariana forearc regions display little or no accreted sediment whatsoever (Moore and Lundberg 1986). The Cascadia margin accretionary prism sediments are, therefore, thought to represent the coarse-grained end-member of the accretionary prism environment (Shipboard Scientific Party 1994). Sediment lithology is a major control upon permeability, and one objective of accretionary prism study is a further understanding of the effect of lithology on the development of accretionary prism geometry.

2.2 CASCADIA MARGIN

This study concerns the convergent margin between crust of the Juan de Fuca plate, formed at the Juan de Fuca Ridge, and North America. At present, this convergence rate is approximately 42 mm per year, in the direction N69°E (DeMets et al. 1990). Subduction is the descent of one tectonic unit under another. Convergent motion has produced subduction at the Cascadia margin since the Eocene (MacKay et al. 1992). The oldest crust of the Juan de Fuca plate currently subducting is upper Miocene (8 Ma) in age (Kulm et al. 1984). This subduction zone has no topographic expression where a trench would usually be evident (Fig. 1.1), as the region is overlain by turbidite fill of the Cascadia Basin (Kulm et al. 1984).

2.3 CASCADIA BASIN

Sediments in the Cascadia basin consist of eastward thickening turbidites of Pliocene and Pleistocene age (Kulm et al. 1984). Seismic stratigraphy suggests two basic divisions: an upper unit consisting of very fine- to medium-grained sandy turbidites, and a lower unit of eastward-dipping silty turbidites (Kulm et al. 1984). The lower unit of turbidites is typical of abyssal plain deposits, whereas the upper unit is more terrigenous, representing sediment from distal portions of the Astoria Fan (Fig. 1.1) (Shipboard Scientific Party 1994). Rapid clastic influxes characterize deposition in these submarine fan systems (Shipboard Scientific Party 1994).

Accreted sediments of the lower continental slope off Oregon form a series of thrust-bounded anticlinal ridges (MacKay et al. 1992, Carson 1977). Interpreted as Cascadia basin strata deformed against the continental slope (Silver 1972), seismic reflection profiling of these ridges identifies individual reflectors traceable across the boundary between the continental slope and the Cascadia basin (MacKay et al. 1992, Silver 1972). Exceptions include draped sediment and local areas of turbidite fill ponded on the landward side of the marginal ridges (Fig. 2.2) (MacKay et al. 1992).

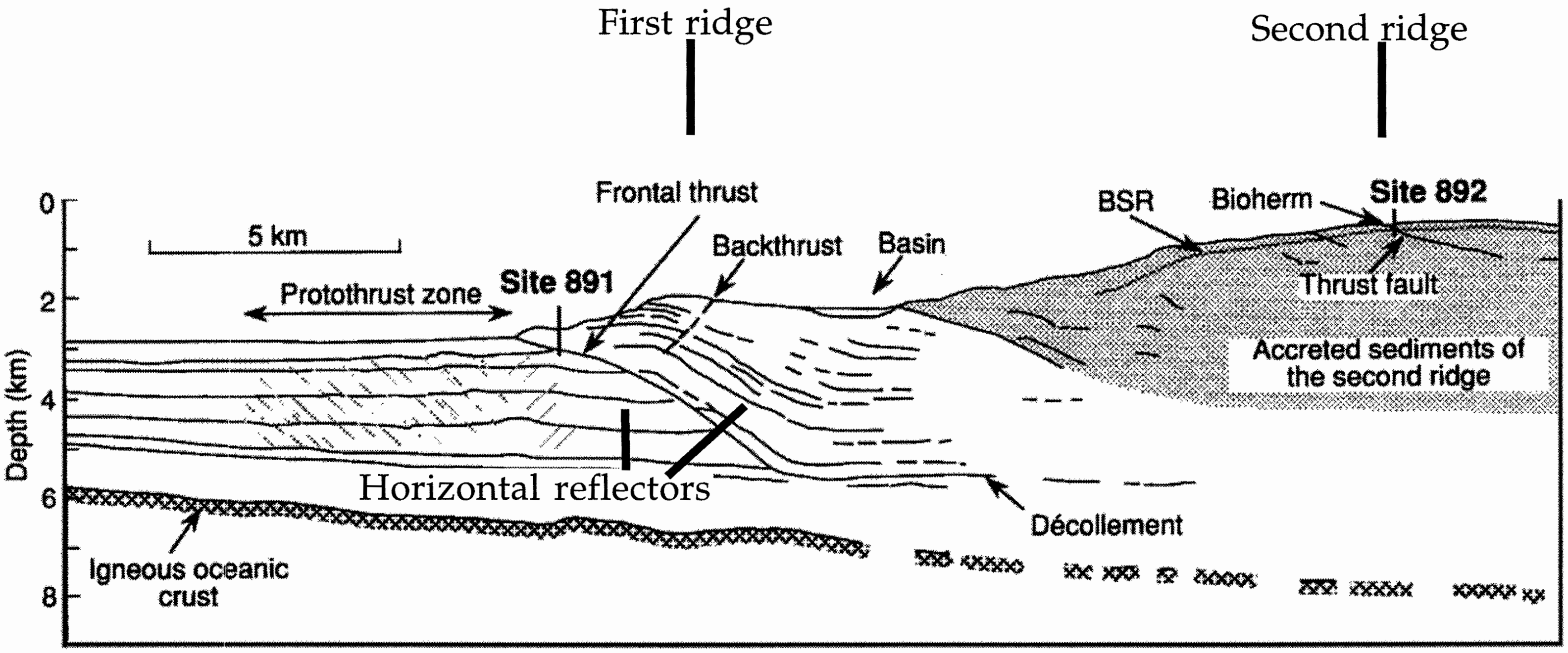

FIGURE 2.2. Generalized morphology of the Oregon margin near Sites 891 and 892. Thrust faulting has produced a pair of anticlinal ridges, labelled first ridge and second ridge. Horizontal seismic reflectors within Cascadia Basin sediments in the protothust zone continue onto the first ridge, where they are deformed. Seismic profiles also image the frontal thrust fault, back thrusts, decollement and an older thrust fault at Site 892, as labelled. Between the first and second ridge, a small ponded basin contains turbidite fill and draped sediments (after Shipboard Scientific Party 1994).

2.4 ACCRETIONARY PRISM

Offscraping of sediment at convergent margins forms accretionary prisms, stressing the accreted sediments and resulting in excess pore pressure and fluid flow. Additionally, fault zones develop to accommodate structural shortening, through tectonic thickening. Evidence that fluid flow occurs within these fault zones comes from several observations. These include the presence, at the surface expression of faults, of benthic communities of clams and worms that depend upon nutrients in venting fluid (Lewis and Cochrane 1990). Also found near fault surface expressions are crusts of sediment that have been cemented by biogenic carbonate, which combined with the benthic communities form complexes known as bioherms (Kulm et al. 1986). Bioherms require constant, nutrient-rich fluid flow along faults to support them. Additional evidence for fault-zone fluid flow is in the form of high heat flow values, as advective flow of warm fluid along a fault zone produces these anomalous values (Langseth and Hobart 1984).

In the central Oregon margin, subduction of the Juan de Fuca plate produces well-defined belts of folded ridges and thrust faults within the overlying sediments as these sediments offscrape from the subducting plate (Fig. 2.2). This process is ongoing, resulting in continued deformation and uplift of the ridges (MacKay et al. 1992, Moore et al. 1991). This deformation and uplift accretes sediment onto the lower continental slope, adding from 30 km to 50 km of slope width in the past 2 Ma (Carson 1977, Silver 1972).

2.4.1 Central Oregon Margin Vergence

The structural style of sediment deformation expressed within the Cascadia margin displays a transition in vergence in the central Oregon margin (MacKay et al. 1992). Seely (1977) defined vergence as the relative sense of motion of overthrusting sediments (Fig. 2.3).

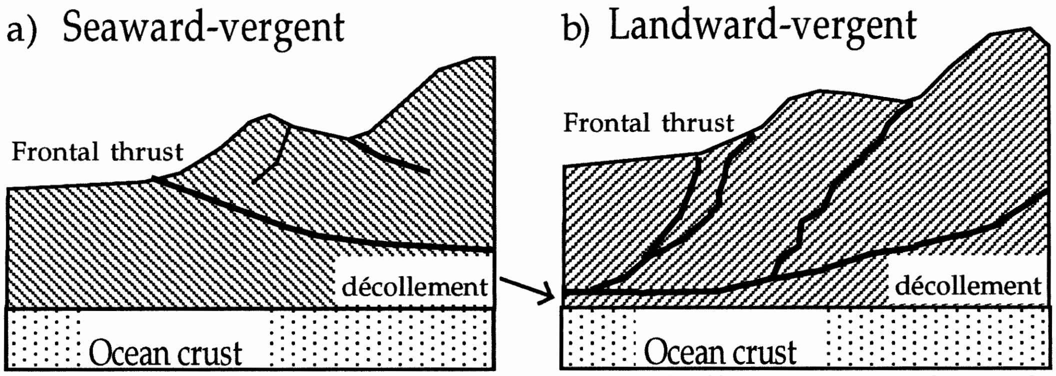

FIGURE 2.3. Simple diagram illustrating the concept of vergence, defined by the relative sense of motion of overthrusting sediments. Region a) displays seaward-vergence, as in the central Oregon and Vancouver Island regions of the Cascadia margin, whereas b) displays landward-vergence, as is evident in the Cascadia margin between these regions. Seaward-vergent regions have a shallower decollement.

Accretionary prisms usually display seaward-vergence, that is, the overthrusting sediments of a seaward-vergent thrust sheet move seaward along a landward dipping thrust fault (MacKay et al. 1992) (Fig. 2.3). Vergence direction affects the depth of the décollement, which is the plane of dislocation caused by an upper unit of material folding and sliding over a lower series of material. At the central Oregon margin, seaward-vergent regions display décollement depths approximately 1.4 km above the underlying oceanic crust. Landward-vergent regions to the north of the study area display décollement depths only several hundred metres above the oceanic crust, resulting in nearly the entire thickness of incoming sediment overthrusting the preceding thrust sheet (MacKay et al. 1992). The direction of vergence therefore has important implications regarding the source and migration paths of pore-fluid within the prism, as different accretionary prism thicknesses result from the two regimes. The thicker landward-vergent packages of accreted sediments contain larger volumes of fluid than in seaward-vergent sections. However, the greater thicknesses of sediment present also create longer drainage paths. Permeability results from the central Oregon margin (seaward-vergent), therefore, may not be directly applicable to the adjacent, but landward-vergent, portions of the Cascadia margin. The cause of changes in vergence direction at the Cascadia margin is not fully understood, but discussion of this is beyond the scope of this study.

2.4.2 Site 891

The westernmost ridge of the Oregon continental margin is a seaward-vergent, anticlinal thrust sheet formed by movement along the landward-dipping frontal thrust fault (Fig. 2.2). Site 891 lies approximately 1.9 km to the landward side of the surface expression of this thrust fault, at 2663 mbsl (Fig. 2.4). Seismic reflection profiles image the frontal thrust fault at 375 mbsf (Fig.2.4). Coring at Site 891 intersected this frontal thrust, which was a primary factor in locating the Site. Sampled lithologies at this Site consist of clayey silts and fine to medium sand. The sediment is of post-middle Pleistocene age,

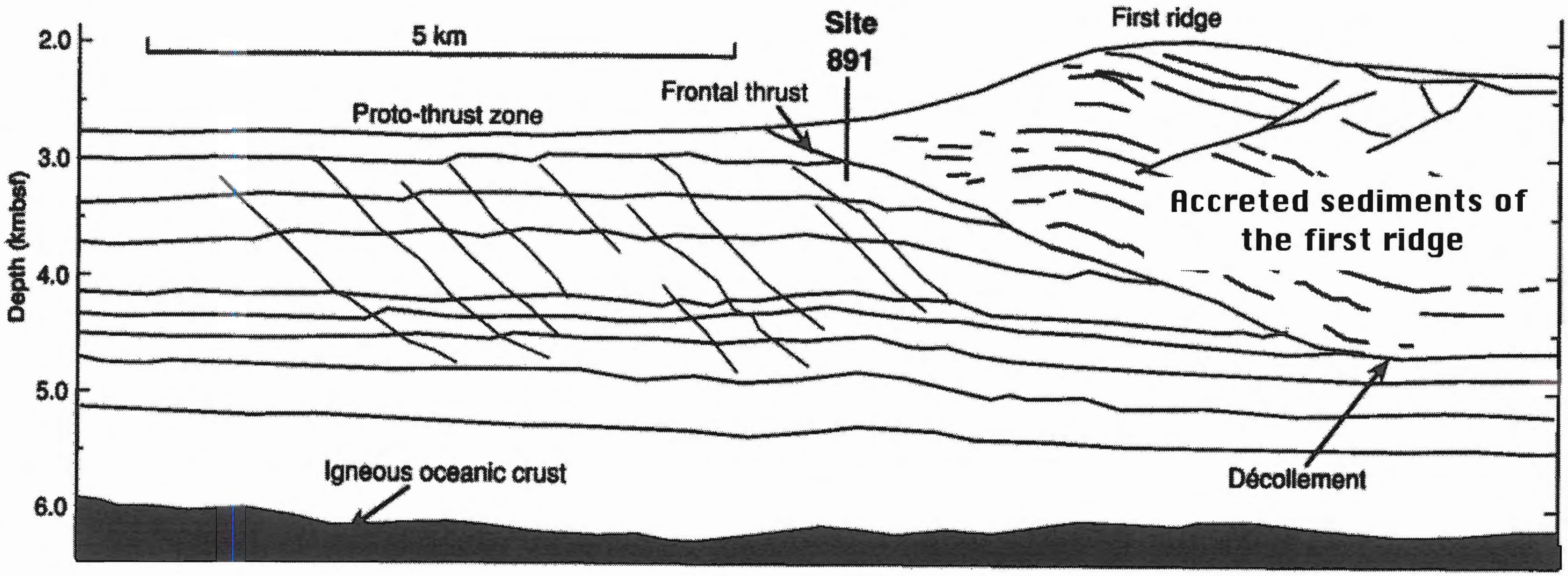

FIGURE 2.4. Schematic diagram of Site 891 and the first ridge. Illustrated are the locations of Site 891 and the frontal thrust fault. (after Shipboard Scientific Party 1994)

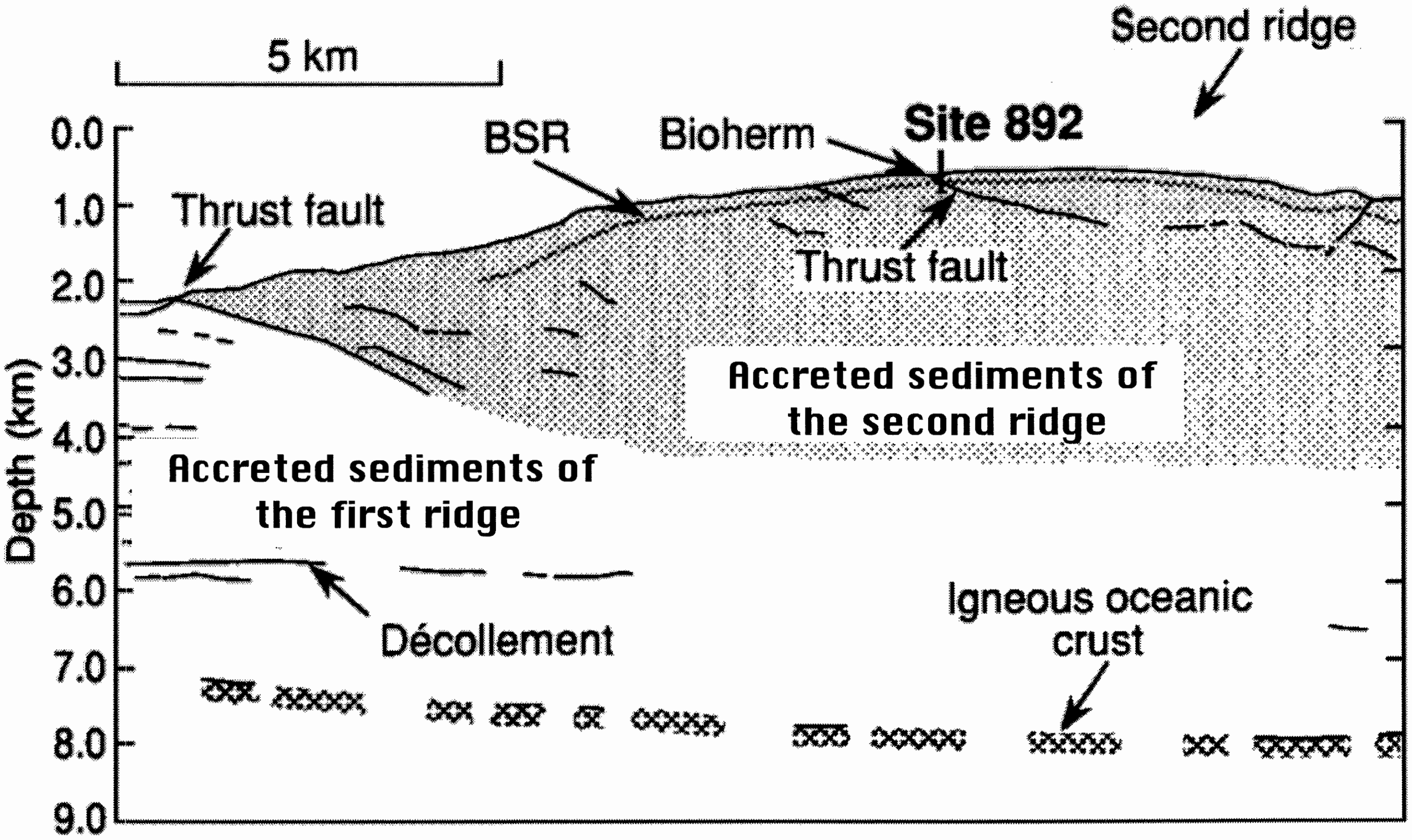

FIGURE 2.5. Schematic diagram of Site 892 and the second ridge. Labeled are the locations of Site 892, a thrust fault penetrated at the Site, and the bottom-simulating reflector (BSR) produced by gas clathrates. Also shown are the Pliocene and younger accreted sediments of the second ridge, and the basal décollement of the margin. The presence of a bioherm at the thrust fault suggests fluid venting occurs here. (after Shipboard Scientific Party 1994)

interpreted as deposits proximal to the Astoria fan before uplift (Shipboard Scientific Party 1994).

2.4.3 Site 892

Site 892 lies near the crest of the second ridge of the accretionary prism off central Oregon, at 670 mbsl (Fig. 2.5). The site is approximately 350 metres east of the surface expression of a landward-dipping, hydrologically active fault associated with a bioherm (Shipboard Scientific Party 1994). Site 892 sediment consists of terrigenous silty clay and clayey silt with scattered sand layers, interpreted as Pliocene abyssal-plain deposits (Shipboard Scientific Party 1994). Seismic reflection profiling at this site images the thrust fault at 105 mbsf. This site displays a seismic bottom-simulating reflector at 68 mbsf (Fig. 2.5), the existence of which was a factor in locating this site, as investigating the nature of the gas hydrates (clathrates) that produce these reflectors was an objective of ODP Leg 146.

2.5 GAS CLATHRATES

Gas clathrates are ice-like compounds in which methane and other gases are trapped within crystalline structures formed by water molecules (MacDonald 1992). Upon freezing, water ordinarily forms a hexagonal crystal structure. However, water that is fully saturated with methane, or several other gases, and under moderate pressures, crystallizes to form a cubic

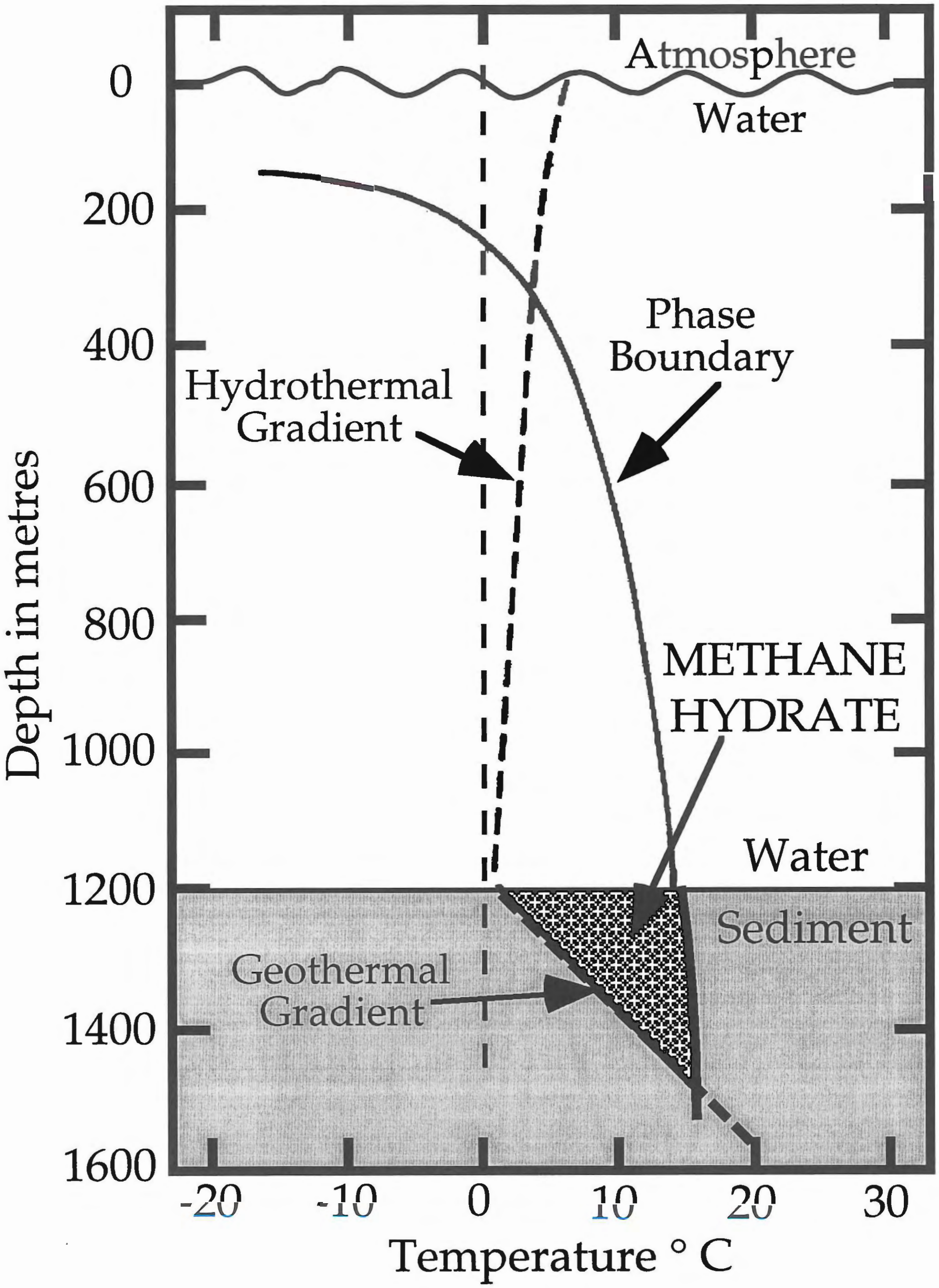

FIGURE 2.6. An example of a depth-temperature stability zone for methane hydrate in a continental margin setting. The phase boundary is that of methane hydrate in pure water. Hydrates may occur in the patterned region provided sufficient concentrations of methane. (after Kvenvolden 1988)

structure upon freezing (MacDonald 1992). This cubic crystal structure has large interatomic spacings which accommodate gas molecules. The clathrate structure of interest in this study is that which is able to trap methane. This structure has the abbreviated formula $CH_4 \bullet 5.75\ H_2O$ and contains 46 water molecules and up to 8 molecules of methane, as not all spaces need be filled with gas (MacDonald 1990). In physical appearance, clathrates are similar to wet snow or ice, and occur commonly as small crystals or nodules dispersed throughout a host sediment.

Clathrates have a stability field dependent on three major factors. The most important factor in geologic environments is the presence of sufficient methane. Whereas not all of the interatomic spaces of the clathrate structure need be filled by methane, less than 80% saturation of these spaces results in the destabilization of the clathrate (MacDonald 1992). The formation of clathrates, therefore, requires large amounts of methane, on the order of 122 kg to produce 1 cubic metre of clathrate.

The other two factors governing clathrate stability are temperature and pressure, and Figure 2.6 illustrates the relationship between these factors. The appropriate temperature and pressure conditions for clathrate stability occur beneath wide regions of the ocean floor. Their distribution is much more limited, however, as a result of low concentrations of methane, which is the critical factor for the formation of clathrates. Areas of confirmed methane clathrate occurrences commonly coincide with sedimentary environments of recent tectonic consolidation or rapid sedimentation. These environments are also sites of active fluid expulsion, and Hyndman and Davis (1992) proposed a mechanism for the concentration of methane by removal from expelled fluid, within the clathrate stability zone. Support for this mechanism of methane concentration is provided by the fact that the same environments of fluid expulsion associated with clathrates are also marked by the presence of bottom-simulating reflectors (Hyndman and Davis 1992).

2.6 BOTTOM-SIMULATING REFLECTORS

The sharply defined seismic reflection (Fig. 2.5) is termed a bottom simulating reflector (BSR) because the trace of the reflector on a seismic profile mimics, or simulates, the bathymetry of the sea floor. Recent investigations by Hyndman and Spence (1992) suggest that the BSR results from a contrast in acoustic velocity between sediments that contain gas clathrates within their pore spaces and underlying sediments that contain no clathrates. As clathrate formation can not occur until methane concentrations are sufficient, this interpretation of BSR formation requires a transitional upper boundary and a sharp lower boundary to clathrates within sediments. The sharp lower boundary produces a strong seismic-velocity contrast at the base of the stability zone that images as the BSR. Support for this model comes from comparison of calculated clathrate stability fields to analysis of the seismically imaged BSR, which indicate similar depths within sediments

(Hyndman and Spence 1992).

At Site 892, a fluid-venting thrust-fault zone disrupts the BSR (Shipboard Scientific Party 1994) (Fig. 2.5). This observation suggests that relatively warmer fluids flowing in the thrust-fault zone disturb the temperature conditions at which gas clathrates are stable, as the BSR is associated with the base of the stability field for methane clathrate (Hyndman and Spence 1992). The absence of a BSR in the slightly warmer thrust-fault zone (Fig. 2.5) suggests that gas clathrates are not present in this interval, and that anamalous variations in temperature have some effect on clathrate stability. Anamalous pressure variations, however, are negligible in the clathrate stability field. The distribution of gas clathrates is, therefore, not only dependent on diffuse fluid flow for the concentration of methane, but also on concentrated flow and the associated thermal anomalies found in fault zones. Permeability data provided in this study may help constrain the process of fluid expulsion, and consequently, the formation of gas clathrates. However, modelling of this process is complex and not attempted in this study.

2.7 ODP SAMPLING AND PROCESSING METHODS

Sediments for this study were sampled using rotary drilling techniques and the Extended Core Barrel (XCB) tool. The XCB allows coring in firm sediments when piston coring is no longer effective, as it is equipped with a saw-toothed cutting shoe which can extend beyond or retract within the bit, depending on the resistance encountered. Standard ODP coring procedures use 10 metre long barrels. Once brought to the surface, cores were allowed to reach ambient temperatures on the deck of the ship. Cores were then sampled for geochemistry, to indicate if potentially explosive or toxic levels of hydrocarbon or hydrogen sulphide gases were present. Cores were split lengthwise into archive and working halves, except for small intervals left whole for consolidation testing. Pore fluid geochemistry work was performed on the cores at this time, then the archive halves were photographed, described for their sedimentological and structural features, and were colour analyzed digitally. Paleomagnetic tests were then performed on the archive halves using a cryogenic magnetometer.

The working halves of the core were tested for bulk density, porosity and acoustic velocity using a multi-sensor track device. Pocket penetrometer testing was performed to derive shear strengths for the sediments, and biostratigraphic analysis using microfossils was conducted. The cores were finally cut into shorter sections for later land-based laboratory analysis, sealed in wax and stored in 4° C seawater.

2.8 SUMMARY

The Cascadia margin accretionary prism comprises Pliocene and younger turbidite and distal fan sediments deposited in the Cascadia basin. Convergent plate motion at the Cascadia margin subducts the Juan de Fuca plate, and offscrapes the overlying basin sediment into the accretionary prism. This process stresses the sediments, resulting in excess pore pressures and fluid flow. The permeability of the accreted sediment constrains the rate and mechanisms of this fluid flow, which in turn has implications for the formation of gas clathrates. Permeability, therefore, is an important characteristic of the Cascadia margin. Because of the dissimilar structural evolution of different portions of this margin, however, the permeability data provided in this study may not be universally applicable throughout the margin.

CHAPTER 3: THEORY AND METHODOLOGY

3.1 INTRODUCTION

Two important concepts in the study of the physical world are those of stress and strain. Stress is simply a measurement of force per unit area. Strain is deformation that results from an applied force. Therefore, strain is a result of stress, and within the elastic limits of a material, strain is proportional to stress. The deformation, or strain, of sediment is divided into an elastic component and an inelastic component. The elastic component is temporary and reversible, only existing while strain is applied. The inelastic component of deformation is permanent, remaining strained after the deforming stress is removed. As strain is proportional to stress, this permanent component of strain records valuable information about past maximum stress conditions. This study uses laboratory consolidation testing to determine these past maximum stress conditions, known as the preconsolidation stress, or $P_{c.}'$. These values are used in this study to return sediment to close to the stress conditions that existed *in situ*, in order to perform permeability measurements that will better reflect permeabilities *in situ*.

Moreover, stresses higher than the P_c' strain sediment in a relationship that is determined by consolidation testing. This relationship is known as the compression index (C_c).

Consolidation tests measure the elastic component of deformation, by recording decreases in strain upon the removal of a stress. These values, known as elastic rebound values, allow correction of shipboard physical property results to better represent those that existed *in situ.*, because many physical properties change as a sample is brought to the surface (MacKillop et al in press).

As discussed in Chapter 2, fluid flow and expulsion within accreted sediments are important factors controlling their deformation patterns. This fluid flow is governed by sediment permeability. In this study, sediment permeabilities are deduced, by analysis of consolidation test height data, and directly measured, at close to *in situ* stress levels, by means of flow-pump permeameter testing.

3.2 DEFINITIONS AND BASIC EQUATIONS

Before proceeding to the theory of consolidation testing, it is useful to review several definitions. One important concept in this study is that of void ratio. The void ratio, e , is the volume of voids over the volume of solids, or

$$e = V_v \; / \; V_s \qquad (3.1)$$

where e = void ratio,
V_v = volume of voids, and
V_s = volume of solids within sediment sample.

Basic sediment physical properties used to correlate or quantify changes within sediments are known as index properties. One important index property is porosity, n , which is related to void ratio and is the volume of voids over the total volume of a sample, expressed as a percentage, or

$$n = V_v \;/\; V_t \quad \text{x } 100\ (\%) \tag{3.2}$$

where n = porosity in percent,
V_v = volume of voids, and
V_t = total volume of sediment sample.

An additional index property is water content, w , which is the mass of water over the mass of solids, expressed as a percentage, or

$$w = M_w \;/\; M_s \quad \text{x } 100\ (\%) \tag{3.3}$$

where w = water content (%),
M_w = mass of water, and
M_s = mass of sediment solids

The final index property of interest to this study, bulk density, can now be derived by assuming water fills all voids. Bulk density, ρ_{sat}, is defined as the total mass (or the mass of solids plus mass of water) over total volume, or

$$\rho_{sat} = M_s + M_w \;/\; V_t = M_t \;/\; V_t \tag{3.4}$$

where ρ_{sat} = bulk density,
M_t = total mass of sediment, and other units are as defined earlier.

3.3 THEORY

Empirically derived relationships form the basis of many applied disciplines, not the least of which is the field of geotechnical engineering. Many of the relationships utilized in this field of study were derived empirically through careful analysis, and subsequently borrowed a mathematical basis from other disciplines, such as thermodynamics. The constant refinement of these relationships, in the context of site-specific factors, leads to a high degree of confidence in their application.

3.3.1 Consolidation

The concept of consolidation can be elusive, as the term is used in many contexts, often incorrectly. Geologists frequently use the term to suggest a degree of cohesiveness within a sedimentary unit, perhaps better regarded as the degree of lithification. This study defines consolidation, following Terzaghi (1943), as the change in the volume of voids within saturated sediment that results from a decrease in water content. Consolidation of sediment occurs as a result of stress, a common source of which is the force of gravity acting on the mass of a sediment. Consolidation from this gravity-induced stress is commonly called gravitational compaction.

Thus consolidation, as defined by Terzaghi (1943), results in increasing bulk density, and decreasing porosity and water content. These changes in index properties produced by consolidation may also result from other factors, such as lithological changes or diagenetic effects such as cementation. Generally, however, index properties can be useful indicators of consolidation, and their interpretation provides estimates of the relative state of consolidation within a sediment. Specifically, the change in porosity resulting from consolidation has been of interest for some time, as a result of the implications porosity has for petroleum reservoir potential.

3.3.2 State Of Consolidation

Studies in the field of petroleum geology have made important contributions to our present understanding of consolidation. Athy (1930) and Hedberg (1936) analyzed data from oil wells and developed empirical relationships between porosity and depth (and thus pressure), for clays and shales (Fig. 3.1). These porosity-depth relationships took the form of logarithmic functions. Subsequent investigations have established the validity of these equations, although as Hedberg noted (1936), no exact solution is possible because of the large number of composition variables.

Central to the existence of a logarithmic relationship between depth, and porosity, or the other index properties, is the existence of a stress which varies in proportion to depth. The intergranular stress at any point is the total vertical stress minus the neutral, or hydrostatic, stress. This stress acts in the vertical plane only, and is known as the vertical effective stress, P_o'. The overburden stresses resulting from the force of gravity acting on the mass of each overlying interval of sediment determine P_o', a factor which varies approximately linearly with depth, depending on sediment homogeneity.

Thus P_o' is defined as

$$P_o' = \Sigma\{(\rho_{sat} - \rho_w)_i \times (z_i - z_{i-1}) \times g\} \tag{3.5}$$

where P_o' = vertical effective overburden stress,
ρ_w = density of water within sediment,
z = depth below seafloor,
g = gravitational acceleration, and other units as defined earlier.

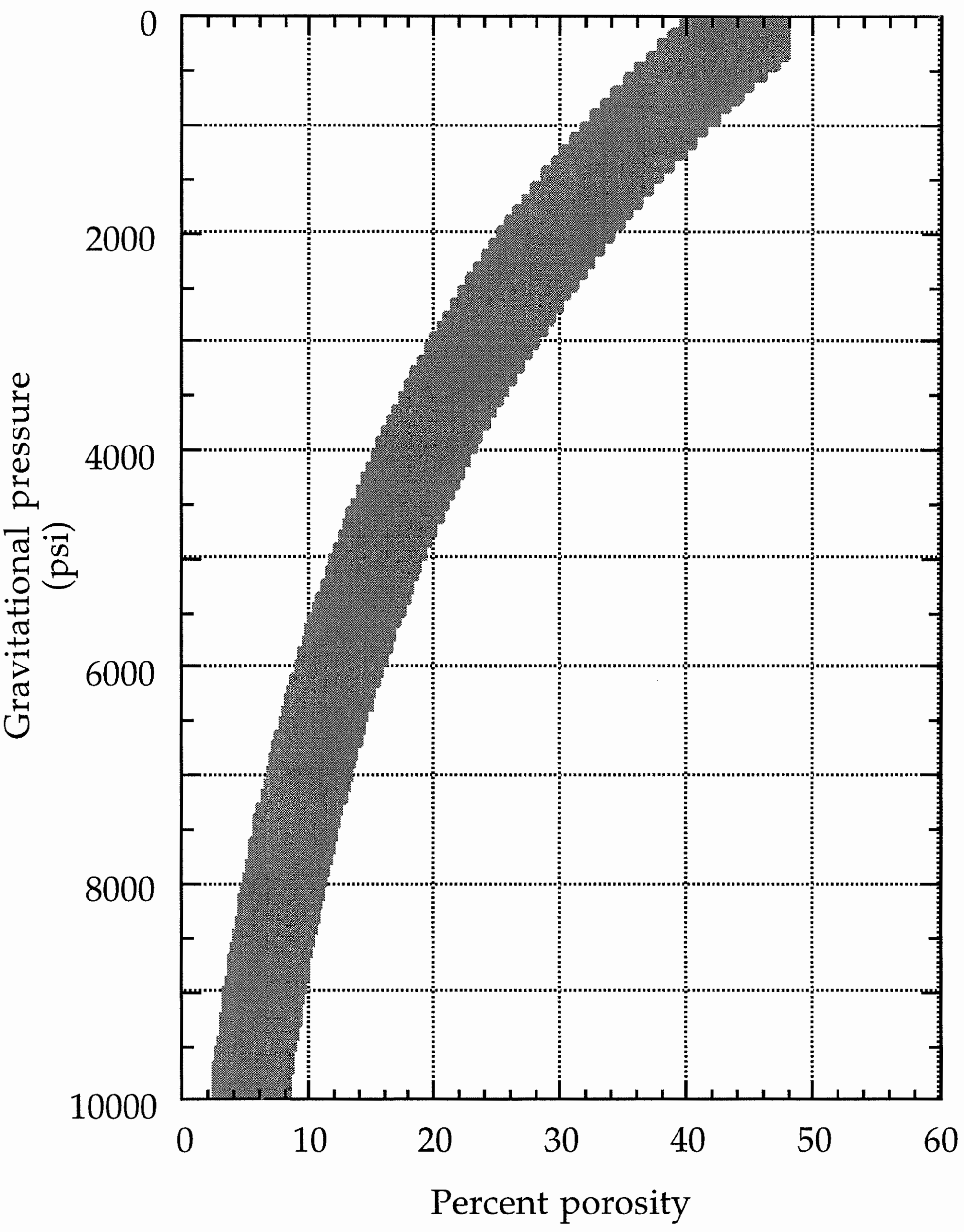

FIGURE 3.1. The relationship of pressure to the porosity of clays and shales, as determined through petroleum industry exploration work in Venezuela, and Kansas, USA. Early studies of this kind were instrumental in developing consolidation theory. (after Hedberg 1936)

The proportional increase in vertical effective overburden stress should, under normal circumstances, result in a proportional change in index properties within a sediment. As these index properties are indicators of consolidation, the concept follows that under normal circumstances, consolidation should progress at a rate that is proportional with depth. This understanding allows us to establish a consolidation rate which is considered normal for a particular lithology, and to designate sediment in that state as "normally consolidated".

Several methods can be utilized to indicate consolidation state. For example, comparison of porosity-depth data from within similar lithologies, or to porosity-depth functions established for those lithologies, can indicate relative consolidation states. As porosity decreases with consolidation, sediments that display lower porosity than is normal or predicted are labelled overconsolidated. Sediments that have a higher porosity than is predicted are underconsolidated. This idea is applied Section 4.2.2.3.

Another index of consolidation state is undrained shear strength (S_u), which is the shear stress at which a sediment fails. Although not directly proportional to any of the previously discussed index properties, shear strength tends to increase with depth in a uniform manner. Discussion of the relationship between shear strength and consolidation is lithologically influenced and complex. For this study, sufficient understanding of the relationship is provided by noting that the increase of shear strength with increasing vertical effective overburden stress (P_o') for normally consolidated materials consistently demonstrates S_u / P_o' ratios of approximately 0.25 (Mesri 1975). Ratios of less than 0.25 suggest underconsolidation, as a result of lower shear strengths than expected, whereas ratios of greater than 0.25 suggest overconsolidation and higher than expected shear strength. Section 4.2.3 reports shear strength test results.

3.3.3 Overconsolidation ratio

Described above are several simple methods for inferring relative consolidation states. These methods utilize physical property data that are commonly collected, and they can be performed quickly, requiring only simple equipment and calculation. These methods, however, provide only relative, qualitative assessments of consolidation. Determination of a quantitative measure of consolidation state requires consolidation testing. Analysis of consolidation test data allows the calculation of P_c', the preconsolidation stress. The ratio of the preconsolidation stress to the vertical effective overburden stress is known as the overconsolidation ratio, or OCR, defined as

$$\mathrm{OCR} = P_c' / \mathrm{P_o}' \tag{3.6}$$

where OCR = overconsolidation ratio, and other units as defined earlier,
and OCR = 1 indicates normal consolidation,
OCR < 1 indicates underconsolidation, and
OCR > 1 indicates overconsolidation.

3.3.4 Consolidation Testing

Laboratory consolidation testing measures the change in sample volume over time as a uniaxial loading stress is applied (Fig. 3.2). Changes in volume can result from the compression of fluids within voids, the deformation of sediment particles, and the reduction in void volume by the expulsion of contained fluids. The relatively low stresses applied during testing cause little deformation of sediment particles. Compression of void fluids is negligible, assuming saturation with water. Therefore, volume change during testing results mainly from, and at rates controlled by, the expulsion of fluid from voids. As samples are contained horizontally within a cylindrical chamber, any changes in volume occur as changes in sample height only (Fig. 3.2), with pore fluids draining from both the top and bottom of the sample chamber.

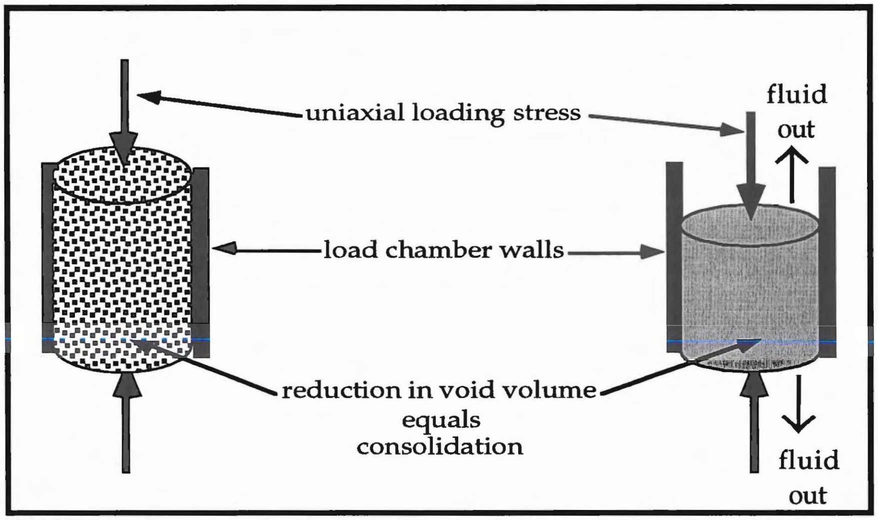

FIGURE 3.2. Illustration of void volume reduction during consolidation testing. Volume reduction occurs as decreases in sample height. Consolidation testing derives the relationship between time, load stress and sample height decrease.

Recording the change in sample height over time allows analysis of the rate of height decrease, to determine the point at which fluid expulsion is complete. This is the point of 100% primary consolidation. Any further reduction in sample height results from the relatively minor deformation of sediment particles. The method of analysis used in this study is that of Taylor (1948), which is fully described in Appendix A. Taylor's method identifies the point of, and provides the sample height (H_{90}) and time (t_{90}) at, 90% primary consolidation. Simple calculations then yield the sample height (H_{100}) and time (t_{100}) of 100% primary consolidation. The time of 100% primary consolidation allows the rate of consolidation to be determined, which is usually expressed as the coefficient of consolidation.

3.3.4.1 Coefficient Of Consolidation

The t_{90} and H_{90} data derived by Taylor's method (Appendix A) are useful for more than just identifying the point of 100% primary consolidation, however. These data also allow us to calculate the coefficient of consolidation, c_v . The coefficient of consolidation is the numerical relationship between the rates of void fluid expulsion, initial void ratio, and the ratio of void volume change with changes in effective stress. The exact derivation of the c_v requires the use of partial differentials, and is somewhat complex. By applying Terzaghi's (1925) one-dimensional theory of consolidation, however, which sets several variables as constants, we can calculate c_v as a function of a time factor, T, determined empirically (Holtz and Kovacs 1981).

T and c_v are related by

$$T = c_v\ t / H^2_{dr} \tag{3.7}$$

where T = time factor
c_v = coefficient of consolidation
t = time
H_{dr} = length of longest drainage path

Empirically derived relationships between consolidation and time allow the use of standard values for T (Taylor 1948). At 90% primary consolidation, as determined by Taylor's method, T is approximately 0.848. Substitution of T, at 90% primary consolidation, allows us to calculate c_v as

$$c_v = (0.848)H^2_{dr} / t_{90} \tag{3.8}$$

The length of the longest drainage path, H_{dr}, is considered the average sample height during a test, divided by 2, as consolidation testing in this study is doubly drained, allowing sample drainage from the top and bottom. All of the data required for calculating c_v are provided by consolidation testing and application of Taylor's method. In this study, c_v is mainly used to provide estimates of permeability.

3.3.4.2 The Casagrande Construction

Decreases in sample height during primary consolidation result only from a decrease in void volume. Therefore, a void ratio (Eqn. 3.1) can be calculated for the sediment that is specific to the stress applied during the test.

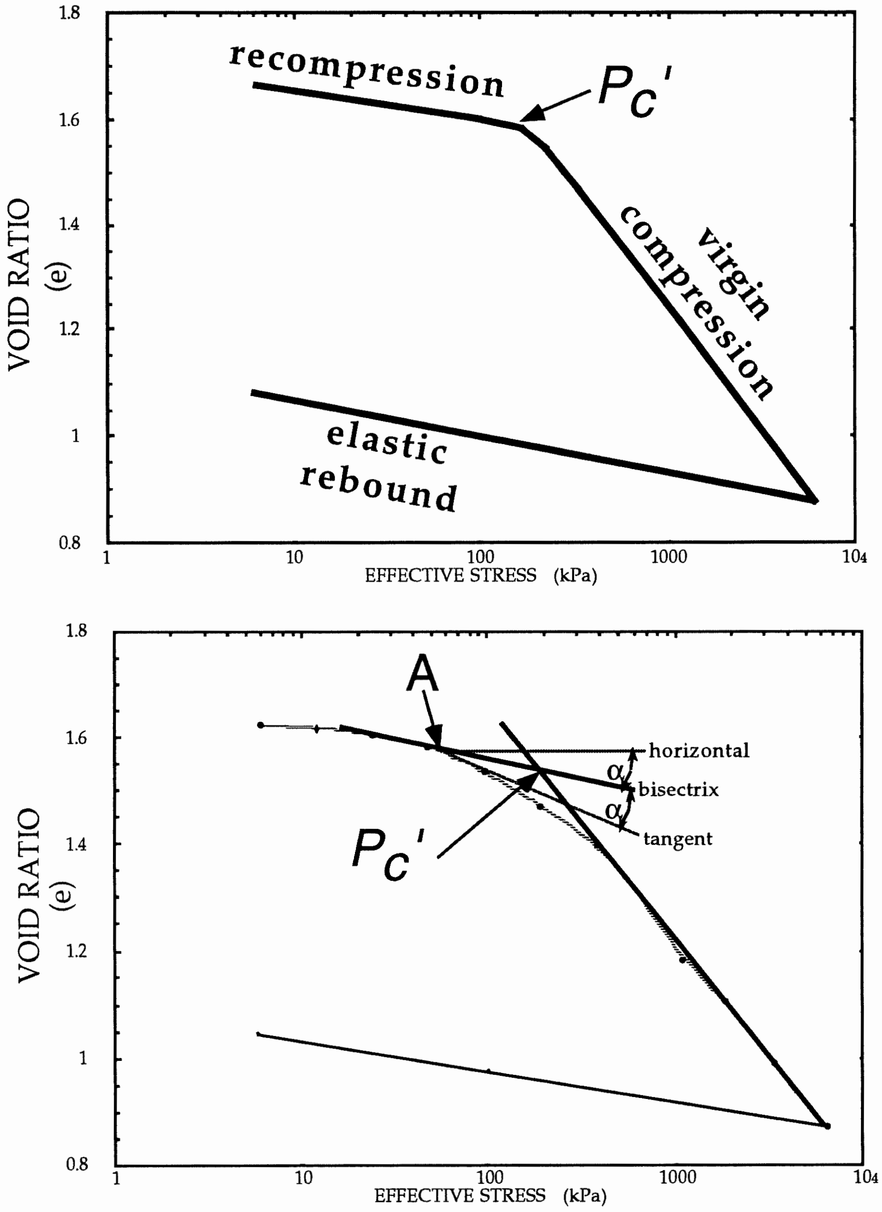

FIGURE 3.3. Void ratio versus log of effective stress plots. Results from consolidation tests form a curve with three parts, as in a). Shown are the recompression curve, the virgin compression curve, and the elastic rebound curve. The preconsolidation stress P_c' marks the transition from recompression to virgin compression. To determine the value of P_c' the Casagrande construction is used, as in b). A horizontal line is drawn to the point of maximum curvature, A. Then a line tangent to the curve at A is drawn. The intersection of a third line, bisecting the angle between the first two lines, with the extension of the virgin compression curve occurs at P_c' .

Repeated testing of the same sample, at increasing levels of stress, results in a pattern of decreasing void ratios. For stresses less than those that the sediment has previously encountered, void ratio decreases are relatively small, as most deformation at that stress has already occurred. For stresses greater than previously encountered, however, void ratio decreases are larger. The transition between these relationships occurs at the preconsolidation stress, P_c', the point of maximum past stress. To determine P_c', this study uses a technique of graphical analysis known as the Casagrande construction (Fig. 3.3) (Casagrande 1936). To facilitate this analysis, this study, following standard practice (ASTM D 2435 1988), doubles the applied stress at each interval (a load increment ratio of 1), so that the resulting data plots as equally-spaced points on a logarithmic graph. Plots of void ratio (vertical axis) against the log of effective stress (horizontal axis) produce a curve with three components, as illustrated in Figure 3.3. a). The portion of the curve from the start of the test to the point of maximum curvature is the recompression curve, representing the interval of small void ratio decreases described above. The approximately linear portion of the curve between the recompression curve and the point of maximum effective stress is the virgin compression curve. This corresponds to the interval of large void ratio decreases described above. The elastic rebound curve (labelled C) represents the increase in sample height resulting from the removal of stress.

Figure 3.3 b) illustrates use of the Casagrande construction to determine the P_c'. The first step in this procedure is to pick by eye the point of maximum curvature between the recompression and virgin compression curves, labelled as A in Figure 3.3 b). Next, draw a horizontal line through this point. Then draw a line tangential to the curve at point A. Draw a third line, bisecting the angle formed by the first two lines, and the point of intersection on the virgin compression curve is P_c'.

3.3.4.3 Other Consolidation Test Coefficients

The c_v, described in Section 3.3.4.1, depends on the effective stress applied at each increment, and is therefore most useful for calculating permeabilities at each increment. There are , however, several important coefficients that depend only on the properties of the sediment, and these are of greater utility and interest.

The first of these sediment-dependent coefficients is the compression index, C_c. The compression index is determined by picking an interval on the virgin compression curve, and from this interval, it is defined as

$$C_c = (e_1 - e_2) / \log (P_2' / P_1') \tag{3.9}$$

where C_c = compression index
e_1 = void ratio at start of interval
e_2 = void ratio at end of interval
P_2' = effective stress at end of interval
P_1' = effective stress at start of interval

The C_c value represents the slope of the virgin compression curve. A second useful coefficient is that of elastic rebound, which can be utilized to correct shipboard physical properties data to *in situ* conditions. Elastic rebound in this study is denoted by C_r, and should not be confused with the recompression coefficient, which is not calculated in this study. Elastic rebound is calculated in a manner identical to compression index, substituting the rebound portion of the consolidation curve, or

$$C_r = (e_1 - e_2) / \log (P_2' / P_1') \tag{3.10}$$

where C_r = coefficient of elastic rebound, and other units as defined earlier. A simple method of determining both values is to find the difference in void ratio for each portion of the curve over one log cycle. The slopes of the virgin compression regression lines represent the C_c, and the slopes of the elastic rebound curves represent C_r.

3.3.5 Permeability And Permeability Testing

The rate of fluid expulsion from void spaces has previously been identified as the most important factor governing consolidation. Hydraulic conductivity is the property of a sample which describes the rate at which fluid flows through it. Also known as or Darcy's coefficient of permeability, hydraulic conductivity is commonly referred to simply as permeability (Holtz and Kovacs 1981). Values of hydraulic conductivity are derived using Darcy's law, usually expressed in the form of:

$$v = Ki \tag{3.11}$$

where v = velocity of flow,
K = hydraulic conductivity, and
i = hydraulic gradient.

Note that the hydraulic gradient, representing the change in elevation over the length of a sample, is a dimensionless unit. Thus the hydraulic conductivity is measured in units of velocity. Laboratory testing for permeability actually measures the hydraulic conductivity, which incorporates both the properties of the material being tested as well as the properties of the liquid. The property of the sediment alone is known as the intrinsic permeability, and in this study will be referred to as such. The relationship between the hydraulic conductivity of a material and the intrinsic permeability of that material is given by the following equation:

$$K = k\rho g \ / \mu \tag{3.12}$$

where K = hydraulic conductivity,
k = intrinsic permeability,
ρ = density of fluid,
g = gravitational acceleration, and
μ = viscosity of fluid.

Hydraulic conductivity testing in the laboratory typically involves the use of either a constant-head permeameter or a falling-head permeameter. These devices pass water through a sediment sample of known height and cross-sectional area, allowing calculation of hydraulic conductivity using the following equation, developed from Darcy's law (equation 3.11):

$$K = Q \ / \ iA \tag{3.13}$$

where Q = discharge from permeameter,
A = cross-sectional area, and other units as defined earlier.

These permeameter devices are not suitable for use with very fine grained materials, however, as accurately measurable accumulations of discharge (Q) require such long periods of time that evaporation of water becomes a large source of error. For this reason, this study uses another technique to measure permeability.

The technique utilized establishes a precisely known rate of flow through a sample within a closed, saturated system. This known rate of flow replaces the requirement for measuring Q. Sensitive instruments capable of recording the pressure difference across the sample generated by this flow provide the information of i, as pressure can be easily converted into height of water. As the cross-sectional area of the testing chamber is known, calculation of K is possible.

Permeability values are also estimated in this study, by analysis of consolidation test height data. This technique involves the relationship of the coefficient of consolidation, c_v, with permeability and void ratio values. Analysis of consolidation test data allows the calculation of a_v, the coefficient of compressibility, which represents void ratio change with change in effective stress. a_v is defined (Holtz and Kovacs 1981) as:

$$a_v = -\Delta e \;/\; \Delta P' \tag{3.14}$$

where a_v = coefficient of compressibility,
Δe = change in void ratio, and
$\Delta P'$ = change in effective stress.

Once the a_v has been determined, calculation of the c_v is possible, using the equation (Holtz and Kovacs 1981)

$$c_v = K / \rho g \;\; \text{x} \;\; (1+ e_0)/ a_v \tag{3.15}$$

where c_v = coefficient of consolidation,
e_0 = initial void ratio, and other units as defined earlier.

From Equation 3.15, we may derive hydraulic conductivity, K, as

$$K = c_v \, \rho \, g \, a_v \;/(1 + e_0) \tag{3.16}$$

where units are as defined above. Conversion between intrinsic permeability and Darcy's permeability or hydraulic conductivity uses Equation 3.12.

3.4 METHODOLOGY

3.4.1 Laboratory Sample Preparation

Whole-round ODP samples from Sites 891 and 892 were stored at the Bedford Institute of Oceanography Core Laboratory in 4° C seawater. As each whole-round sample is large enough to provide several samples for consolidation testing, the samples were x-rayed to determine the portion most suitable for testing. Utilizing a hydraulic ram, these samples were extruded from the 7 cm diameter ODP core barrels into thin-walled, 6.2 cm diameter sample rings (approximately 4.5 cm high). These extruded samples were sealed in wax and stored in 4° C seawater until testing. For the testing procedure, extruded samples were trimmed, using a wire saw, to fit the consolidometers' consolidation ring, and then transferred to this ring. Trimmings were weighed, then dried and weighed again to determine water content. Dried trimmings were then processed for grain density using high precision balances and pycnometer testing to derive initial void ratios for the samples, required for plotting the Casagrande construction (Sect. 3.3.4.2) To prevent desiccation of samples, preparation work was performed immediately before testing.

3.4.2 Laboratory Consolidation Testing

Consolidation testing at the Atlantic Geoscience Centre (AGC) utilizes back-pressured consolidometers (Fig. 3.4). The AGC units are a variation of the standard Casagrande-type lever arm consolidometer (also called an oedometer), in which samples are stressed by a platen loaded via a lever. These standard units require continuous application of water to samples to preserve saturation, and loads are applied by adding weights to the lever.

The AGC units, however, are closed systems that saturate samples by filling the sample chamber with water and then applying a back pressure. This study used a back pressure of 300 kilopascals (kPa). A pascal is equal to

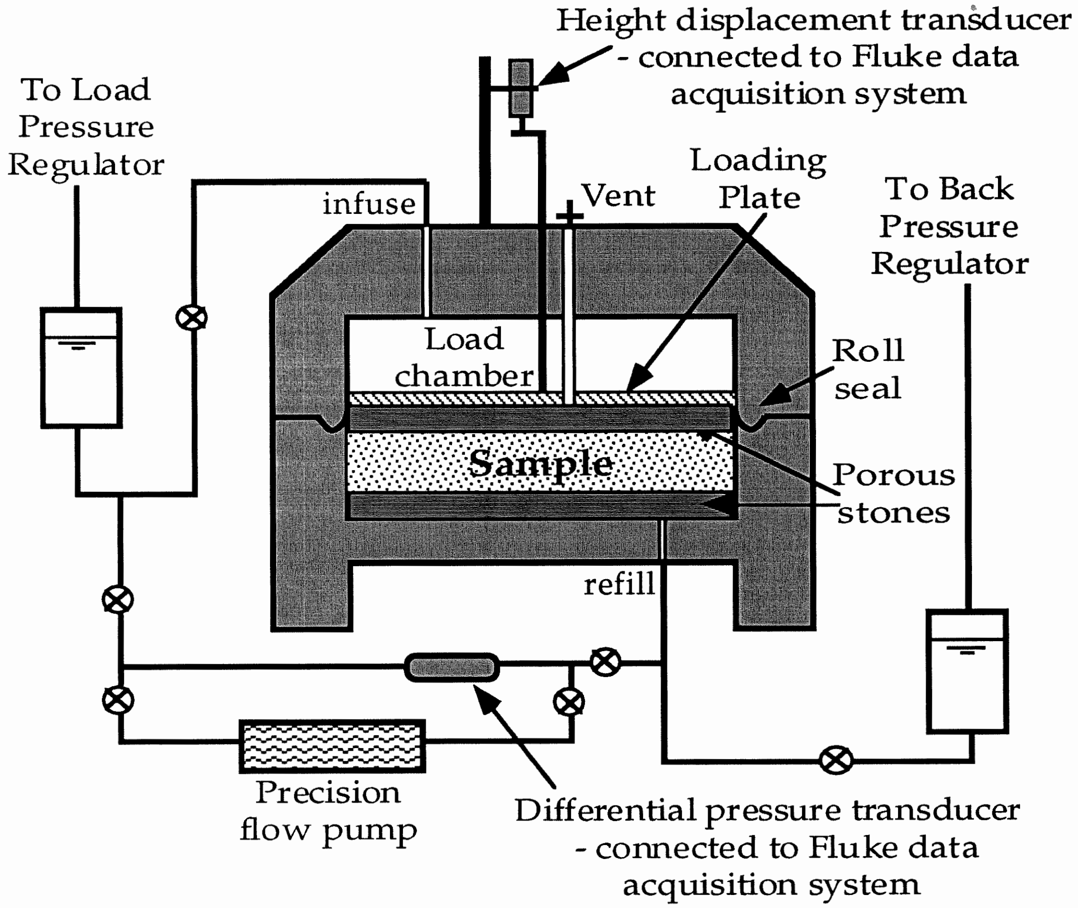

FIGURE 3.4 Schematic diagram of the Atlantic Geoscience Centre back-pressured consolidometer. Cylindrical samples are placed within the sample chamber, saturated with water, and back-pressured for 72 hours, to expel air from pore spaces and return the sample to *in situ* conditions. (after Smith 1993)

one newton of force applied to one square metre of surface area. The application of a back pressure redissolves air bubbles which may have entered into pore fluid within the sample, as it was brought to, or processed at the surface. The presence of such compressible air bubbles can adversely affect consolidation and permeability tests.

Consolidation stresses are applied hydraulically by the load pressure regulator to a loading plate in the load chamber (Fig. 3.4). Applied stresses of up to 7 megapascals are possible at AGC. The applied stress is the difference between the load stress and the backpressure. Changes in sample height within the consolidation ring are measured using a strain-gauge displacement transducer, as well as a dial gauge. The output from the transducer is scanned by a Fluke data acquisition unit and logged by a 486 PC-based datalogging program, simplifying data collection.

Consolidation tests consist of the application of incrementally increasing load stresses. Samples are first loaded to 6 kPa axial pressure. Loads are then incremented by a load increment ratio (LIR) of 1 (Sect. 3.3.4.2), resulting in a doubling of stress at each increment. Maximum axial pressures applied in this study were 6144 kPa. Samples are then incrementally unloaded with each increment being one quarter of the stress of the previous increment. Testing ends when a sample is returned to a 6 kPa axial pressure. Sample height data is logged continuously by the PC during each test. The Fluke data acquisition unit scans the sample height every 5 seconds during the first 3 minutes of each test; thereafter, a 1 minute scan interval is used.

Sample height data is plotted against the square root of time, using the method developed by Taylor (1942), to determine t_{90} and H_{90} values. Taylor's method (refer to Appendix A for a full description of Taylor's method, and the determinations used in this study) consists of drawing a straight line through the initial part of the compression curve, extrapolating the line back to the ordinate axis where time = 0. This intercept represents U_0, the point of 0% primary consolidation. The first data points may not plot on this line as sample height can be affected by swelling and load pressure variations between tests. A second straight line is drawn from this intercept such that the abscissas are 1.15 times those of the first line. The intersection of this second line and the sample height curve represents U_{90}, the point of 90% primary consolidation. The abscissa at this point represents $\sqrt{t_{90}}$, the square root of time at 90% consolidation, whereas the ordinate represents H_{90}, the sample height at 90% consolidation.

Once void ratio data are determined, these data are plotted against the effective stress at each consolidation test increment, and by using the Casagrande construction (Sect. 3.3.4.2), the preconsolidation stress and virgin compression curve slope are determined.

3.4.3 Laboratory Permeability Testing

Permeability testing took the form of hydraulic conductivity tests, as explained in Section 3.3.5. As permeability decreases with increasing consolidation, tests were performed on each sample after several consolidation test increments. Specific consolidation test increments were targeted for permeability tests, with the aim of performing several tests within both the recompression curve and the virgin compression curve.

Permeability tests at AGC utilize a Harvard Apparatus high precision micro-pump, similar to micro-pumps used in medical laboratories. This equipment configuration is referred to as a flow-pump permeameter in this study, following recent examples (Taylor and Fisher 1993). The device supplies accurately metered volumes of fluid, both into the top of the sample chamber (infuse cycle) and into the bottom of the chamber (refill cycle) (Fig. 3.4). A test consists of alternating infuse and refill cycles, allowing time between infuse and refill events for sample pressures to stabilize. Each permeability test consists of infuse and refill runs using three different metered-volume increments.

The fluid infusion or refilling process produces a pressure differential between both sides of the sample, or a pressure head, resulting from frictional forces which correspond to the sample hydraulic conductivity (refer to Sect. 3.3.4). This pressure is measured by a Validyne strain-gauge differential pressure transducer (Fig. 3.4). The output from this transducer is recorded on a Hewlett Packard strip chart recorder and scanned by the Fluke data acquisition unit. The pressure data from these tests, for each volume of flow, is converted using Equation 3.11 into hydraulic conductivity values. The graphs in Appendix B plot the differential pressure measured by the transducer (Fig. 3.4) against the induced flow rate. The equation of the best fit line also provides the slope of the pressure- flow rate relationship. This value is used to calculate hydraulic conductivity as it represents the hydraulic gradient during each test. Refer to Section B.1 for detailed information.

3.5 SOURCES OF ERROR

The techniques employed in this study follow either standard published techniques, such as those described by the American Society for Testing and Materials, or follow techniques developed through much experience by researchers at the Bedford Institute of Oceanography. These standard procedures are designed to create accurate, reproducible results. However, several unavoidable sources of error are inherent in these methods. One major source of error occurs when a sample is cored, extruded and trimmed. The most serious effect of this disturbance is enlargement of the region of maximum curvature on consolidation curves, used to determine P_c'. This effect, as well as sample irregularities within the consolidation cell, leads to a lesser degree of certainty with regard to the P_c'. However, experimentation with the placing of the P_c' value during this study suggests that negligible changes result from placing the P_c' elsewhere within the narrow range of possible values.

Permeability measurements obtained in this study are susceptible to slight errors from the use of fresh water within the consolidation cell. Ideally sea water is used within the cell, however sea water tends to corrode fittings within the consolidometer and is therefore not utilized. The errors resulting from this substitution are at most several percent. One other possible source of error with regard to permeability measurements are osmotic effects produced by swelling clays (Clukey and Silva 1982). This source of error, if present, would again be negligible in the context of this study.

3.6 SUMMARY

The importance of permeability on sediment consolidation can not be overstated. Consolidation is the reduction of void volume, achieved by the expulsion of fluids contained within voids. As permeability governs the rate of expulsion of this fluid, it also controls the rate of consolidation. This study makes use of two techniques of graphical analysis, the Taylor method and the Casagrande construction, to interpret consolidation test data. The results of these techniques are indices of consolidation state and overconsolidation ratios. As well, through the use of Terzaghi's one-dimensional consolidation theory and Darcy's law, both deduced and measured permeability values are obtained for three samples of Cascadia margin accreted sediment over a range of effective stresses. These data provide constraints to rates of fluid flow within the Cascadia margin accretionary prism.

CHAPTER 4: RESULTS AND OBSERVATIONS

4.1 INTRODUCTION

This section presents data gathered during ODP Leg 146, from September to November, 1992, as well as from laboratory testing conducted at the Bedford Institute of Oceanography from October 1993 until March 1994. The ODP data set for each Site includes a wide variety of information, of which only pertinent material is detailed in Section 4.2. Laboratory results are presented in Sections 4.3 and 4.4.

4.2 SHIPBOARD SCIENTIFIC PARTY RESULTS

The ODP utilizes 10 metre long core barrels for drilling and sampling, and expresses total recovery at a Site as a percentage of the total barrel length employed at that Site. Whereas recovery rates were low at Sites 891 and 892, this statistic does not provide any indication of the pattern of core recovery. Typically, each barrel recovers some core at the top of the barrel, with only rare instances of no recovery. The stratigraphic location of the recovered core is well constrained by the length of the drill string in use, allowing the cores to be placed within the framework of the entire borehole. Moreover, seismic profiles provide additional stratigraphic control. Although ODP actively develops innovative technology to improve core recovery, the drilling techniques used during Leg 146 are still considered state-of-the-art. The advent of future technology may improve core recoveries, providing a better understanding of processes and products. Until such time, however, laboratory analysis, such as this study, will have to work around the problem of low recovery rates.

To improve the quality of the samples that are eventually tested for consolidation and permeability, shipboard scientists identify well-recovered sections that are of interest. At AGC, whole-round samples are x-rayed before processing to further improve the quality of tested material, by avoiding clasts and fractured or disturbed regions.

4.2.1 Lithostratigraphy

At both Sites, lithostratigraphic analysis found sediment lithologies to be relatively uniform, and as such, only one lithostratigraphic unit was defined at each Site. Whereas the sediment lithology appears uniform, differences in recovery rate may result from different zones of tectonic disturbance or from mechanical factors related to drilling equipment.

4.2.1.1 ODP Site 891

Core recovery at Site 891 was poor, at less than 11% (Shipboard Scientific Party 1994), with total penetration to a depth of 472.3 metres below sea floor (mbsf). This low recovery precluded detailed lithostratigraphy. As well, recovered material is texturally and compositionally homogeneous and, therefore, defines only one lithostratigraphic unit. However, this unit is subdivided into 3 subunits on the basis of mineralogic and lithologic composition. Biostratigraphic and paleomagnetic analysis constrain sediments at Site 891 to Pleistocene and later age. Of the two holes cored at Site 891, this study uses samples from 891B.

Clayey silt layers at Site 891 commonly contain pebbles of basalt, carbonate concretions, and quartzite. Silts and sands contain up to 40% quartz, 10 to 25 % feldspars, 2 to 12% mica, and up to 30% lithic fragments. Lithic fragments are typically fine-grained igneous rocks of intermediate to basic composition, although chert and schist fragments occur. Accessory minerals include volcanic glass, amphibole and pyroxene. Opaque minerals, in amounts up to 5%, include sulphides and magnetite grains. Biogenic material in core 891B is rare, consisting mainly of diatoms, with only rare occurrences of foraminifera. Carbonate grains, determined to be dolomite, are present in most of the sand and coarse silt fractions.

Fine-grained silts and clays were examined using smear slides and by X-ray diffraction (XRD). Compositions are similar to the coarser-grained fractions, however, more quartz is present in the fine-grained material, and less feldspar and lithic fragments. The clay minerals present include mixed layer (illite/smectite), chlorite, illite/micas and kaolinite. XRD analysis suggests that chlorite is somewhat more abundant than kaolinite.

Subunit 1A (Fig. 4.1) (0-198.2 metres below sea floor) consists of clayey silt interbedded with silt and fine to medium sand. Parallel lamination, as well as rare convolute and cross-lamination, is faintly visible in the silts and sands. Colour of the unit ranges from olive green to a very dark greenish gray. Sediment firmness increases with depth. An interval of disseminated pyrite and dolomite enrichment occurs from 162.7 to 171.6 mbsf.

Subunit 1B (Fig. 4.1) (198.2-383.9 mbsf) consists of firm, fractured unsorted clayey silt, typically dark greenish gray in colour. Minor amounts of dark gray silt and sand are present. Some inclined lamination is visible, with dips of 15 to 20°. Rare wood fragments are present from 207 to 321 mbsf. A disrupted interval from 260.2 to 263.1 mbsf is present, characterized by sediment broken into 0.5 to 1 cm sized pieces and enclosed in black mud matrix.

The upper boundary of subunit 1B is sharp at 198.2 mbsf, marked by the contrast of undisturbed subunit 1A sediments overlying fractured and poorly sorted subunit 1B sediments. This boundary is reflected in physical properties data. The lower subunit boundary is transitional and is delineated by decreased fracturing and better sorting with increasing depth.

Subunit 1C (Fig. 4.1) (383.9-472.3 mbsf) contains dark greenish gray to dark gray clayey silts, sandy silts and fine to medium sands. The sediment is less firm than subunit 1B, with the exception of the interval from 445.8 to 463.5 mbsf, which is firm and somewhat fissile. Wood fragments, carbonate concretions, black sulphides and pebbles are present throughout subunit 1C.

Planar, convolute and cross-lamination are visible in the lowest units, below 463.5 mbsf. This study uses sample from depths of approximately 297 m and 436 m, within subunits 1B and 1C, respectively.

4.2.1.2 ODP Site 892

ODP drilled five holes at Site 892, the deepest of which had a penetration depth of 176.5 mbsf. Recoveries ranged from several to over 50 percent, however overlap from the five separate cores allowed good lithostratigraphic analysis. Nevertheless, this analysis defined only one lithostratigraphic unit, as recovered sediment was lithologically uniform. On the basis of visual descriptions, XRD, and grain-size analysis, this unit was divided into two subunits. Biostratigraphic and paleomagnetic analysis constrain sediments at Site 891 to Pliocene and younger age. This study uses samples from core 892D, for which the recovery rate was 54%.

Sediments cored at Site 892 are dark gray to very dark greenish gray, consisting mainly of fine-grained terrigenous and hemipelagic clayey silts and silty clays. The sediment is typically firm and slightly fissile. Original sedimentary structures are rarely visible, however scattered, subhorizontal bedding is defined by slight colour or grain size variations.

Compositionally, the sediments vary slightly between subunits, but in general are dominated by clay minerals, quartz, and feldspars. The clay minerals present are chlorite, illite/mica, mixed-layer clays, and minor amounts of kaolinite. Biogenic components include diatoms and radiolarians, as well as foraminifera, and in intervals account for 20 to 60% of the sediment. Glauconitic sands occur in both subunits as either thin sandy layers or diffuse patches.

Subunit 1A (Fig. 4.2) (0-69.3 mbsf) consists of dark gray to very dark greenish gray clayey silt, interbedded in places with fine sand and coarse silt layers. The clayey silt is mainly clay minerals, quartz, and feldspar, with a 5 to 15% biogenic component consisting mainly of siliceous microfossils. 1- to 10-cm scale bedding is defined by changes in colour. Glauconitic sands occur as 1- to 3-cm thick layers or as irregular patches. Glauconite grains are distributed evenly throughout the clayey silt. XRD analysis of the glauconite indicates it is of a mixed chlorite-smectite type, believed to have formed *in situ* . Carbonate cementation is common from 19 to 69 mbsf, forming patches of sediment up to 4 cm in size.

Gas clathrates are present in the upper 28.5 metres of subunit 1A. The gas component of these clathrates consists mainly of hydrogen sulphide with some methane. Clathrates in subunit 1A decompose within several minutes at surface conditions, resulting in collapsed, dewatered sediment having a soft or "soupy" texture. More than 8% of the volume of these upper sediments may be in the form of hydrates (Shipboard Scientific Party 1994). The sediments below 28.5 metres depth are fractured into 0.1- to 1-cm sized angular pieces, and in firmer sections these are disrupted by subhorizontal

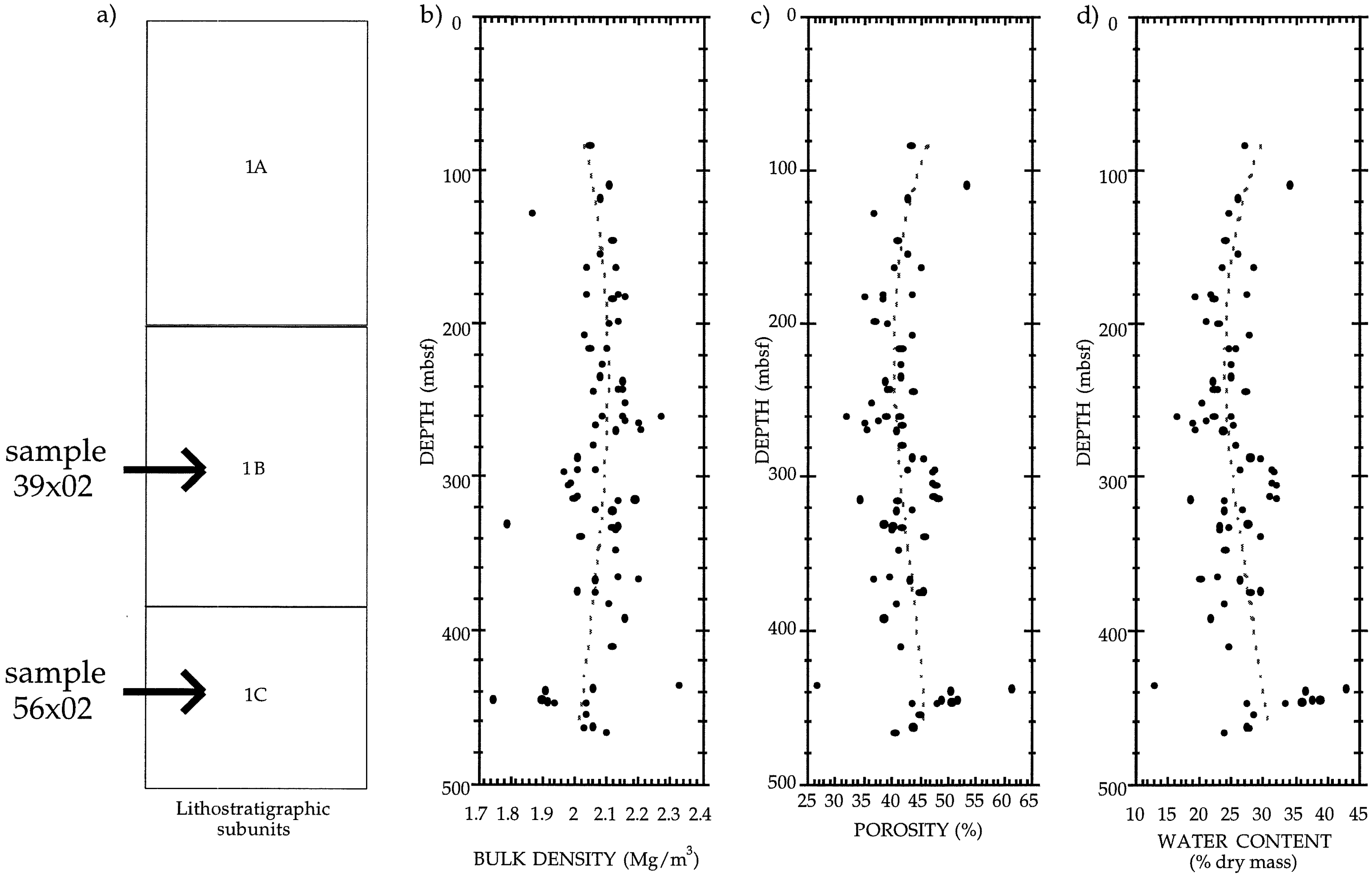

FIGURE 4.1. Lithostratigraphy and index property plots for Site 891B. a) Lithostratigraphic subunits, b) bulk density (Mg/m3), c) porosity (%), and d) water content (% dry mass). Dashed lines are best-fit lines.

cracks. This disruption is thought to result from gas expansion fracturing.

Subunit 1B (Fig. 4.2) (69.3-176.5 mbsf) has an upper boundary at a stratally disturbed, indurated sandy layer which is the basal unit of subunit 1A. The sediments are clayey silts, with scattered silty clays and fine sands. Colour ranges from dark olive gray to dark gray. Slight grain size and colour variations define rare bedding lamination. However, most of the sediment is fractured into 0.1- to 1-cm sized angular pieces, making recognition of structures difficult. Sediment consists mainly of clay minerals, quartz, and feldspars. Volcanic glass comprises up to 14% of several sandy layers from 138-147.5 mbsf. Glauconite is present in patches and dispersed grains, and appears to be less mature here than in subunit 1A. Biogenic components range from 5 to 20%, with several thin intervals of enriched quantities. The clay mineralogy is similar to subunit 1A, with chlorite, mica/illite, mixed-layer clays and minor kaolinite present. Carbonate concretions, dolomite-cemented silts, and microgranular carbonates, all apparently formed *in situ*, account for a carbonate content of up to 15%.

Sediments in subunit 1B are firm, fissile, and fractured, and generally barren of sedimentary structures. Near the top of subunit 1B, the level of fracturing is minor, whereas the sediment below 106.5 mbsf is heavily fractured. Possible intervals of tectonically disturbed sediments, including slickensides, polished surfaces and shear zones, are present at 116-125.5 mbsf and 144.5 -154 mbsf.

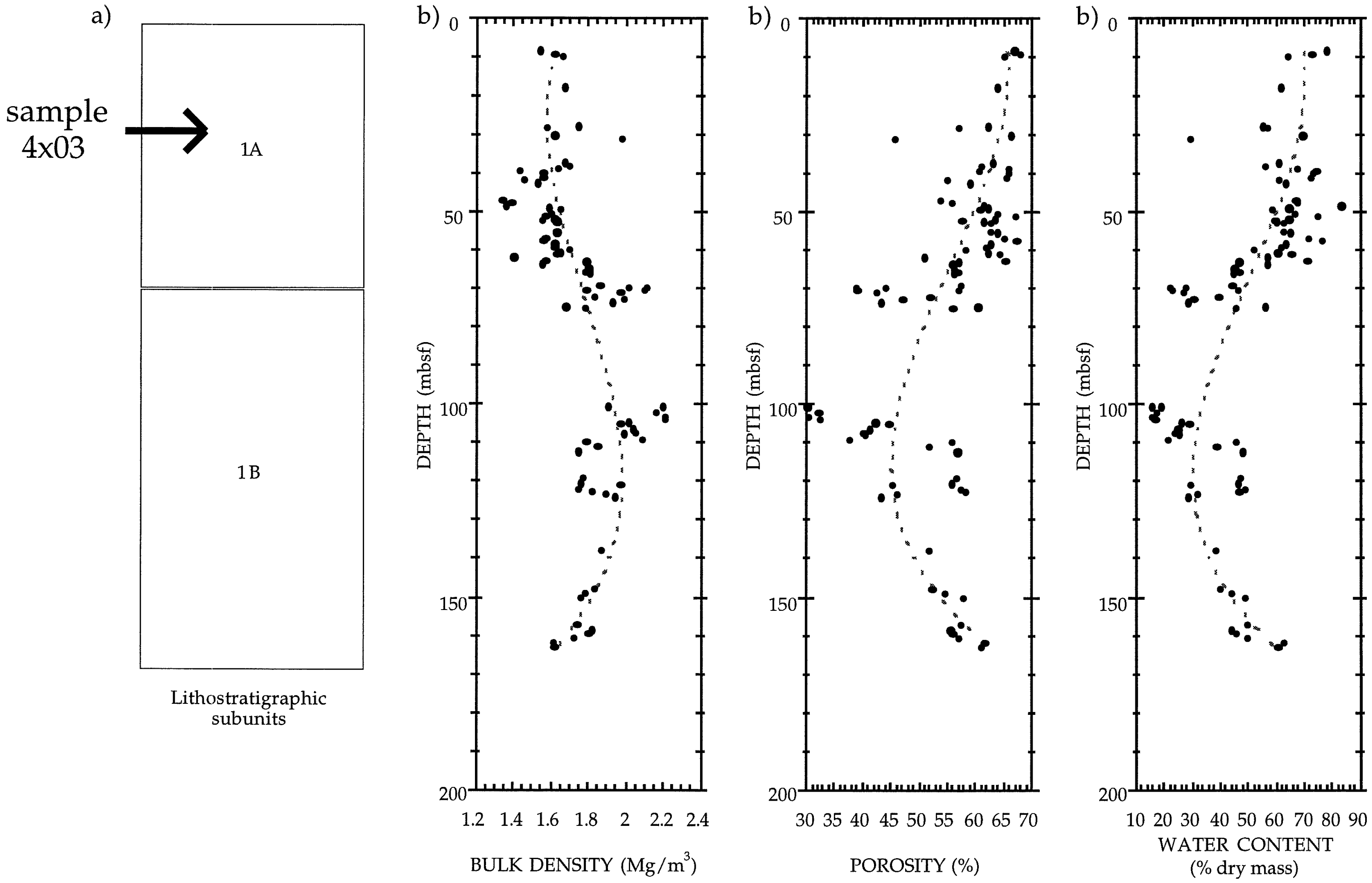

FIGURE 4.2. Lithostratigraphy and index property plots for Site 892D. a) Lithostratigraphic subunits, b) bulk density (Mg/m^3), c) porosity (%), and d) water content (% dry mass). Dashed lines are best-fit lines.

4.2.2 Index Properties

Physical properties testing of sediments cored during Leg 146 provide a wide range of data, of which the major index properties, bulk density, porosity, and water content, are reported here. In general, index properties show several offsets within each core, not always coincident with an identified lithostratigraphic interval. The cause of these offsets varies, but structural features may be responsible.

Athy (1930) and Hedberg (1936) investigated gravitational compaction in clays and shales. Their work resulted in empirically derived relationships between depth and porosity that are logarithmic equations. Subsequent work has shown the validity of these relationships, which define a reduction in porosity, resulting from decreased void space, with increasing depth and the increased overburden stress this increase in depth brings with it. The rate at which porosity decreases with depth depends upon sediment lithology. In situations with relatively constant lithology downhole, porosity reduction and the concomitant increase in bulk density and decrease in water content should remain constant with depth, displaying a logarithmic trend.

4.2.2.1 ODP Site 891

Reported in Table 4.1 are shipboard index properties for sediments drilled at Site 891B. As a result of the low recovery rate at Site 891, the data set is less comprehensive than usual ODP practice. The results are, however, consistent with subsequent analysis. Plotted against depth in Figure 4.1 b),c), and d), these properties indicate normal gravitational compaction in the upper subunit, 1A. The increase in bulk density, and decrease in porosity and water content in subunit 1A varies consistently with depth, illustrated by the trend of best-fit lines (dashed lines) in Figure 4.1.

The index properties do not vary consistently with depth in subunits 1B or 1C. Within these lower units, index properties tend to be offset at regular intervals of 50 to 70 metres (Shipboard Scientific Party, 1994). Index properties display an offset close to the subunit 1A/1B boundary, with four other major offsets below subunit 1A, at 261 mbsf, 315 mbsf, 368 mbsf and at 439 mbsf. These lower major offsets are characterized as being either sealed boundaries, that change downhole from lower porosity to higher porosity, or as drained boundaries, changing downhole from higher to lower porosity.

4.2.2.2 ODP Site 892

Table 4.2 details shipboard index properties of sediments drilled at Site 892D. The data are of good quality, and are consistent internally and with subsequent analysis. Plotted against depth in Figure 4.2 b), c), and d), these properties indicate normal gravitational compaction in the upper subunit, 1A, except in the upper 14 metres of core. These upper 14 metres were somewhat disturbed by the presence of gas clathrates in the core, and display a discontinuity in index properties. Below this disturbed section, however, the

DEPTH	ρ	n	w	DEPTH	ρ	n	w
(m)	(Mg/m3)	(%)	(%)	(m)	(Mg/m3)	(%)	(%)
2.7	1.96	49.22	33.7	287.5	2.01	43.89	28.1
3.45	1.71	61.24	56.5	288.27	2.01	45.77	29.8
4.1	2.03	44.42	28.1	295.32	2.07	42.97	26.4
4.95	1.92	49.95	35.5	295.82	2.01	47.86	31.5
5.99	1.86	53.56	40.8	296.95	1.97	47.36	31.8
7.11	1.98	48.45	32.7	304.75	1.99	47.4	31.5
7.45	1.9	52.47	38.6	305.78	1.98	47.95	32.2
83.38	2.05	43.46	27.1	313.25	2.01	47.52	31.1
109.85	2.11	53.44	34.2	314.7	2	48.35	32.2
118.66	2.08	42.84	26.1	315.2	2.19	34.39	18.7
127.74	1.87	36.84	24.6	314.35	2.14	41.15	24
127.7	2.12	41.13	24.2	322.15	2.07	43.7	26.9
154.32	2.08	42.97	26.2	322.95	2.12	40.94	24
162.9	2.04	45.34	28.7	330.69	1.79	38.69	27.7
163.4	2.13	40.53	23.6	331.87	2.14	40.28	23.3
180.65	2.04	43.8	27.5	332.29	2.12	41.87	24.8
181.35	2.14	38.39	22	332.44	2.13	40.09	23.3
182.2	2.16	35.2	19.5	339.5	2.02	46.01	29.7
182.66	2.12	38.49	22.4	348.4	2.13	41.38	24.2
198.41	2.14	37.13	21.1	368.3	2.07	43.32	26.6
199.19	2.11	39.36	23.1	367.6	2.2	37.02	20.3
207.31	2.03	43.91	27.8	375.55	2.01	45.77	29.7
216.02	2.1	41.51	24.8	375.72	2.07	45.25	28.1
216.16	2.05	41.85	25.9	366.25	2.14	39.6	22.8
225.47	2.09	41.63	25	384.1	2.11	40.82	24.1
234.35	2.08	41.75	25.2	411.35	2.12	41.82	24.7
237.67	2.15	38.92	22.2	393.14	2.16	38.61	21.9
242.7	2.14	39.65	22.8	438.05	2.06	61.36	43
243.1	2.15	39.21	22.4	437.06	2.33	26.77	13
244.19	2.06	44.01	27.3	439.57	1.91	50.76	36.6
251.58	2.16	36.53	20.5	446.25	1.9	51.78	37.8
260.35	2.15	39.15	22.4	446.42	1.75	48.79	39
260.7	2.09	41.52	25	446.89	1.92	50.88	36.2
260.8	2.27	32.06	16.5	447.43	1.94	48.34	33.4
263.5	2.16	37.75	21.3	447.87	2.04	43.76	27.5
264.45	2.2	35.16	19.1	455.05	2.04	45.22	28.6
264.29	2.07	41.91	25.5	463.7	2.06	44.03	27.4
269.4	2.21	35.68	19.4	464.2	2.03	44.15	28
270.05	2.13	40.76	23.8	465.57	2.1	40.69	24.1
279.02	2.06	41.96	25.8				

TABLE 4.1. Index property data for ODP Site 891B. Listed are values for bulk density (ρ) in Mg/m^3, porosity (n) in %, and water content (w) in %.

DEPTH (m)	ρ (Mg/m3)	n (%)	w (%)	DEPTH (m)	ρ (Mg/m3)	n (%)	w (%)
8.6	1.55	67.22	78.2	69.46	1.87	57.62	44.9
9.65	1.63	68.17	73.3	69.9	2.12	38.93	22.6
10.15	1.67	65.21	64.8	70.2	2.02	44.18	28.1
18.1	1.68	64.05	62.6	70.55	2.11	39.3	23.1
27.9	1.76	62.45	55.8	70.62	1.8	57.17	47.1
28.3	1.59	57.29	57.3	70.95	1.98	42.73	27.6
30.37	1.63	66.51	69.9	72.46	1.84	52.21	40.1
31.42	1.99	45.8	30.1	72.84	2	47.3	31.2
37.5	1.68	63.25	61.4	73.77	1.94	43.56	29.2
38.25	1.71	61.24	56.6	75	1.69	60.65	56.8
38.82	1.65	66.18	67.8	75.38	1.79	56.22	46.1
39.32	1.44	60.82	74.8	100.95	2.2	30.27	16
40.1	1.57	66.11	73.7	100.96	1.91	30.51	19.1
41.3	1.57	65.7	73	102.4	2.17	32.39	17.6
41.93	1.46	55.1	61.4	103.55	2.21	30.53	16.1
42.63	1.54	59.3	63.7	104.1	2.21	32.46	17.3
47.31	1.35	53.85	67.7	104.95	2.02	42.52	26.9
47.57	1.4	56.01	68	105.35	1.98	44.89	29.5
48.6	1.37	61.58	83.8	106.68	2.05	41.35	25.4
49.15	1.6	62.45	65.3	107.53	2.06	40.19	24.4
49.57	1.66	61.09	59	108.03	2	40.78	25.7
50.53	1.61	64.01	67.2	109.48	2.1	37.82	22.1
51.25	1.58	67.26	75.2	110.15	1.8	56.09	45.8
52.1	1.63	63.78	65.2	111.25	1.86	52.1	39.2
52.45	1.56	57.87	60	112.35	1.76	57.11	48.7
52.6	1.65	61.77	60.7	112.68	1.76	56.98	48.3
53	1.64	62.88	63.1	119.41	1.78	56.84	47.6
55.2	1.64	62.72	62.9	120.95	1.77	55.97	46.7
55.7	1.64	64.14	65.5	121.35	1.98	45.64	30.1
57.06	1.58	65.48	72.2	122.2	1.76	57.53	49.3
57.56	1.57	67.55	77.1	122.8	1.83	58.4	47.3
58.56	1.63	62.82	63.9	123.7	1.9	46.2	32.3
59.36	1.63	62.1	62.4	124.5	1.95	43.54	29
60.06	1.71	58.59	52.6	138.35	1.88	52.13	38.7
60.86	1.66	62.54	61	148.2	1.84	52.62	40.5
61.28	1.64	64.46	65.9	149.4	1.79	54.78	44.7
62.18	1.41	51.18	57.5	150.7	1.77	58.07	49.6
62.85	1.58	65.52	71.7	157.48	1.75	57.75	50
63.25	1.8	57.29	47.4	159.03	1.83	55.83	44.4
63.87	1.56	56.22	57.4	159.73	1.81	56.25	45.7
65	1.81	56.28	45.6	161.07	1.73	57.22	50.1
65.98	1.79	57.04	47.1	162.23	1.62	61.9	62.9
66.25	1.82	56.28	45.2	163.43	1.63	61.32	60.9

TABLE 4.2. Index property data for ODP Site 892D. Listed are values for bulk density (ρ) in Mg/m^3, porosity (n) in %, and water content (w) in %.

increase in bulk density, and decrease in porosity and water content in subunit 1A vary with depth, illustrated by the trend of best-fit lines (dashed lines) in Figure 4.2. The base of subunit 1A marks the site of another discontinuity, at which point index properties cease to vary consistently with depth. Subunit 1B displays three discontinuities, at 104 mbsf, 144 mbsf and 164 mbsf. These discontinuities may be the products of localized shear consolidation (Shipboard Scientific Party 1994), resulting in a dewatering of discrete zones of the core.

4.2.2.3 Porosity-depth Profiles

Porosity reduction has long been identified as a consequence of sediment consolidation (Athy 1930, Terzaghi 1943) As a result, comparison of the porosity-depth profiles of shipboard data with porosity-depth profiles established for normally consolidated silty clay (Brückmann 1989) allows some indication of a sediments relative consolidation state. Refer to Section 3.3 for discussion on consolidation theory and definitions.

At Site 891, comparison of porosity-depth profiles suggests three regions of stress history (Fig. 4.3 a). Above 200 mbsf, the porosity values are less than those predicted for a normally consolidated silty clay, suggesting a state of overconsolidation. Between 200 mbsf and 280 mbsf, porosity values are close to predicted, suggesting normal or slight underconsolidation. Below 280 mbsf, and particularly below 439 mbsf, porosity values are higher than

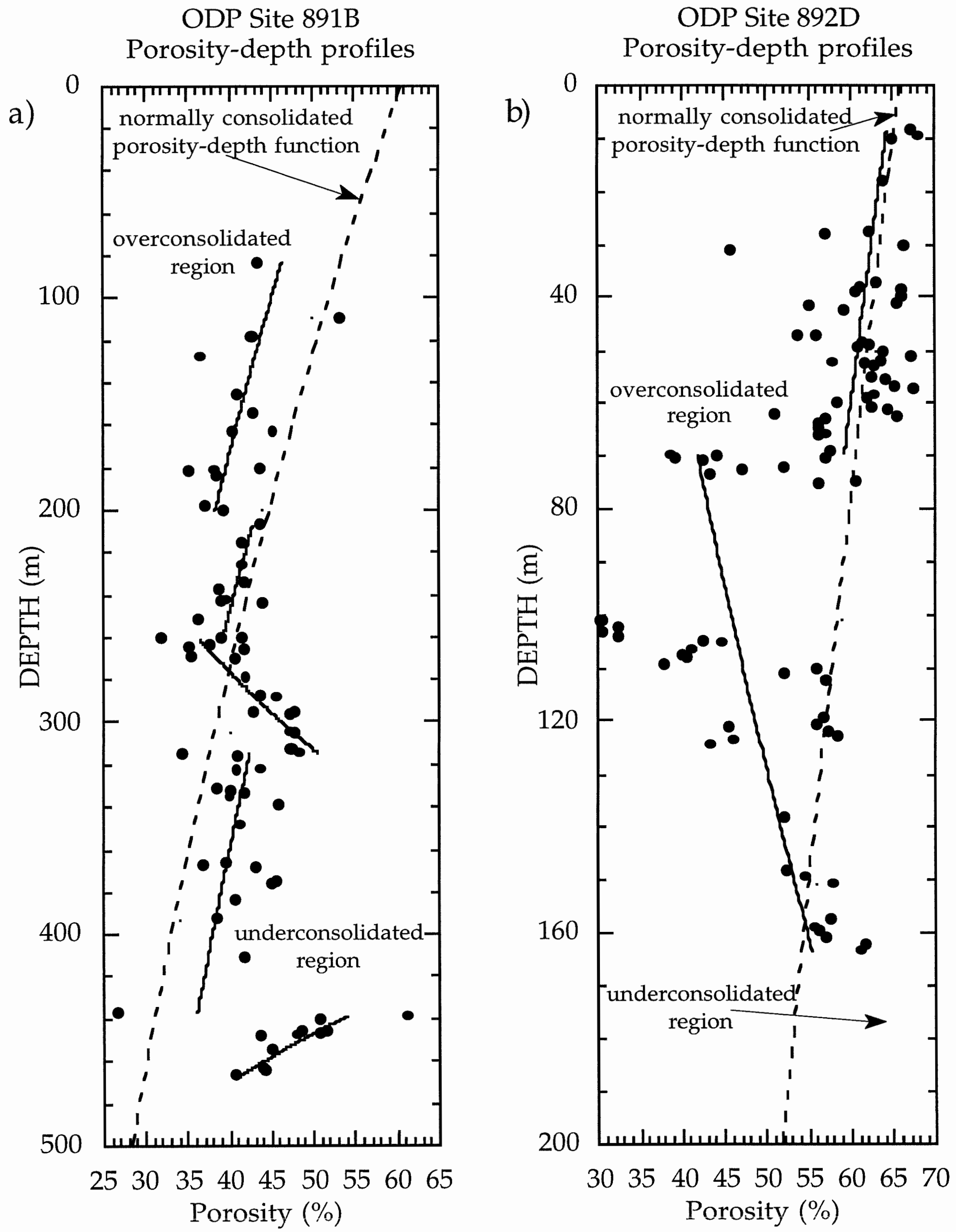

FIGURE 4.3. Porosity-depth profiles for, a) Site 891B and, b) Site 892D. Dashed lines are porosity-depth profiles (Brückmann 1989) for normally consolidated clayey silt a), and silty clay b), solid lines are exponential regressions for index property subdivisions. Points to the left of the dashed lines indicate lower than expected porosity, those to the right, higher than expected. Several areas of rapidly increasing and decreasing porosity are shown, related to fault zones.

predicted, suggesting a state of underconsolidation in general, and significant underconsolidation below 439 mbsf (Shipboard Scientific Party 1994).

At Site 892, comparison of porosity-depth profiles suggests two regions of stress history (Fig. 4.3 b). The portion of subunit 1A below the clathrate disturbed zone suggests normal or slight overconsolidation, as porosity is close to values predicted for normally consolidated silty clay. In subunit 1B, however, porosity is lower than predicted values, suggesting overconsolidation. However, the low porosities in this region result from shear-induced consolidation within the thrust-fault zone, discounting the utility of applying porosity-depth profiles to this subunit.

4.2.3 Shear Strength

Table 4.3 reports results from shipboard testing of undrained sediment shear strength (S_u). Also listed are values for effective overburden stress P_0' (Sect. 3.3.1) calculated for the intervals tested for shear strength, as well as ratios of S_u / P_0'. Empirically determined relationships between values of S_u and P_0' suggest an S_u / P_0' ratio of 0.25 for normally consolidated sediments. Ratios less than 0.25 suggest underconsolidated conditions, whereas ratios greater than 0.25 suggest overconsolidated conditions. Figure 4.4 plots S_u against depth, as well as a plot of 0.25 times the value of P_0', to produce a curve representing normal consolidation. S_u values that plot beneath the 0.25 P_0 line represent underconsolidated regions, those near the line are normally

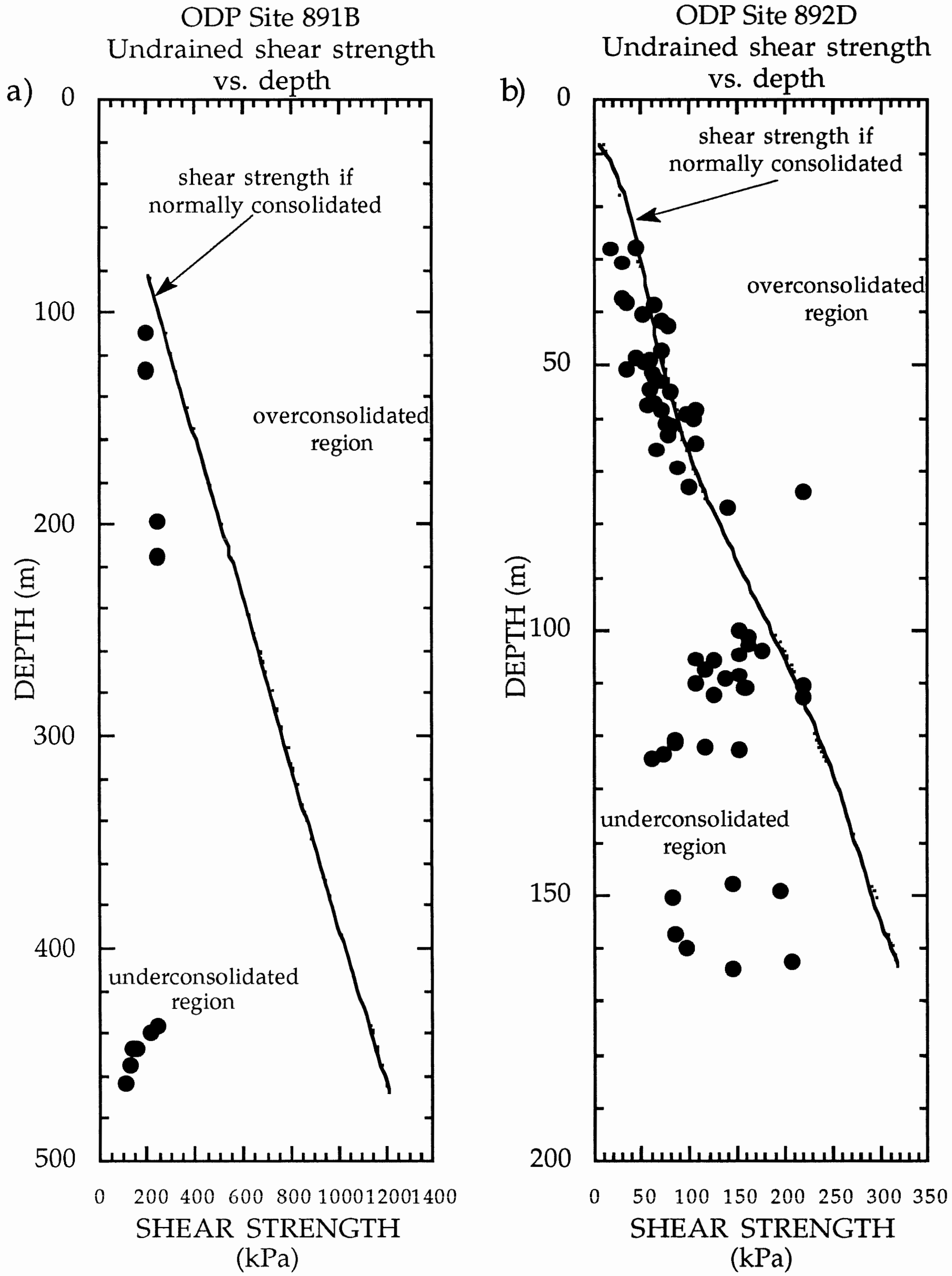

FIGURE 4.4. Plots of undrained shear strength (S_u) versus depth for, a) Site 891B and, b) Site 892D. Also shown are normally consolidated sediment curves for S_u. Each test is marked by a dot. Dots to the left of the curves indicate states of underconsolidation, and to the right, overconsolidation.

consolidated, and those above the line are overconsolidated. Figure 4.4 a) suggests that Site 891B subunit 1A is normally consolidated, subunit 1B is underconsolidated, and subunit 1C is highly underconsolidated. Figure 4.4 b) suggests that Site 892D subunit 1A is normally consolidated, and subunit 1B is underconsolidated. Note that the porosity-depth profile suggested subunit 1B of Site 892 was overconsolidated, as a result of the band of low porosities in the 100 to 110 metre region.

ODP Site 891B				ODP Site 892D			
DEPTH (m)	*Su* (kPa)	*Po'* (kPa)	*Su/ Po'* ratio	DEPTH (m)	*Su* (kPa)	*Po'* (kPa)	*Su/ Po'* ratio
109.75	196	1153	0.17	28	46.06	170.27	0.27
127.74	196	1302	0.15	38.82	63.52	231.16	0.28
199.19	>250	2083	> 0.12	48.6	44.41	287.84	0.15
216.02	>250	2253	> 0.11	52.34	63.09	310.52	0.2
440.04	216	4703	0.05	57.28	62.75	341.6	0.18
437.22	>250	4667	> 0.05	60.3	104.93	361.32	0.29
447.5	140	4757	0.03	66.18	67.38	401.43	0.17
447.87	159	4760	0.03	100.45	151.7	682.82	0.22
455.05	127	4832	0.03	105.7	107.87	731.8	0.15
464.2	110	4922	0.02	110.15	107.87	773.93	0.14
				120.95	85.81	876.7	0.1
				124.5	61.29	910.06	0.07
				148.2	147.1	1108.4	0.13
				163.9	147.1	1190.58	0.12

TABLE 4.3. Undrained shear strength (S_u) data for Site 891B and 892D. Also listed are effective overburden stress (P_o') values for the same intervals, as well as the S_u / P_o' ratios. Ratios of less than approximately 0.25 indicate underconsolidation, those near 0.25 indicate normal consolidation, and those higher than 0.25 indicate overconsolidation.

4.2.4 Packer Permeability

Tests performed during ODP Leg 146 included a packer permeability test on the borehole drilled for Site 892B. In packer permeability tests, an interval of the borehole is hydraulically isolated by means of an inflatable packer device. The interval tested extended from 105.5 mbsf to 178.5 mbsf. The resulting data set was less complete than intended, as technical difficulties were encountered during the packer experiments. As well, drilling the hole itself caused disturbances of sediment and subsequent permeabilities. A borehole seal was installed at the Site with instruments capable of recording long-term pressure fluctuations, with the aim of obtaining accurate *in situ* measurements. The results to date from this Site indicate a permeability in the range of 10^{-5} to 10^{-4} cm/second (Screaton 1994).

4.3 Laboratory Consolidation Testing

This study presents results of consolidation testing performed upon three whole-round samples from the central Oregon margin. Testing took place from October, 1993 until March, 1994, using the methodology described in Chapter 3. Appendix C presents raw data from consolidation tests. These data require some analysis before they provide information about void ratios and states of consolidation.

4.3.1 Taylor's Square Root of Time Method

One method of consolidation test analysis is that of Taylor (1948), described fully in Section A.1. Graphical analysis of all consolidation increments, with the specific 90% consolidation root-time and height values, is provided in Appendix A. These values allow the calculation of sample void ratios, coefficients of compressibility, and coefficients of consolidation for each stress increment. These data allow estimation of permeability.

Sample	892D 4x03	891B 39x02	891B 56x02
Depth (mbsf)	30.45	296.61	447.23
Initial void ratio	1.832	1.147	0.845
effective stress (kPa)	void ratio	void ratio	void ratio
6	1.622	1.028	0.752
12	1.616	n/a	0.751
24	1.604	1.023	0.746
48	1.582	1.004	0.739
96	1.534	0.963	0.727
192	1.469	0.924	0.71
384	1.398	0.878	0.688
384	n/a	0.831	0.661
768	1.185	0.803	0.645
1536	1.107	0.765	0.619
3072	0.991	0.714	0.58
6144	0.872	0.656	0.534
1536	0.903	0.675	0.548
384	0.937	0.699	0.568
384	0.961	0.712	0.576
96	1.008	0.733	0.593
24	1.041	0.739	0.599
6	1.059	0.74	0.601
Pc'	195 kPa	510 kPa	125 kPa

TABLE 4.4. List of void ratios for each effective stress increment. Also shown are preconsolidation stresses determined by use of the Casagrande construction.

4.3.2 The Casagrande Construction

Discussed in detail in Section 3.3.4.2, the Casagrande construction is a graphical method of determining the preconsolidation stress (P_c') of a sediment sample. Refer to Section 3.3.4.2 or Figure 3.3 for detailed instructions. Table 4.4 reports void ratios (Sect. 3.4.1) at each stress increment for samples 892D 4x03, 891B 39x02, and 891B 56x02, as well as the P_c' values

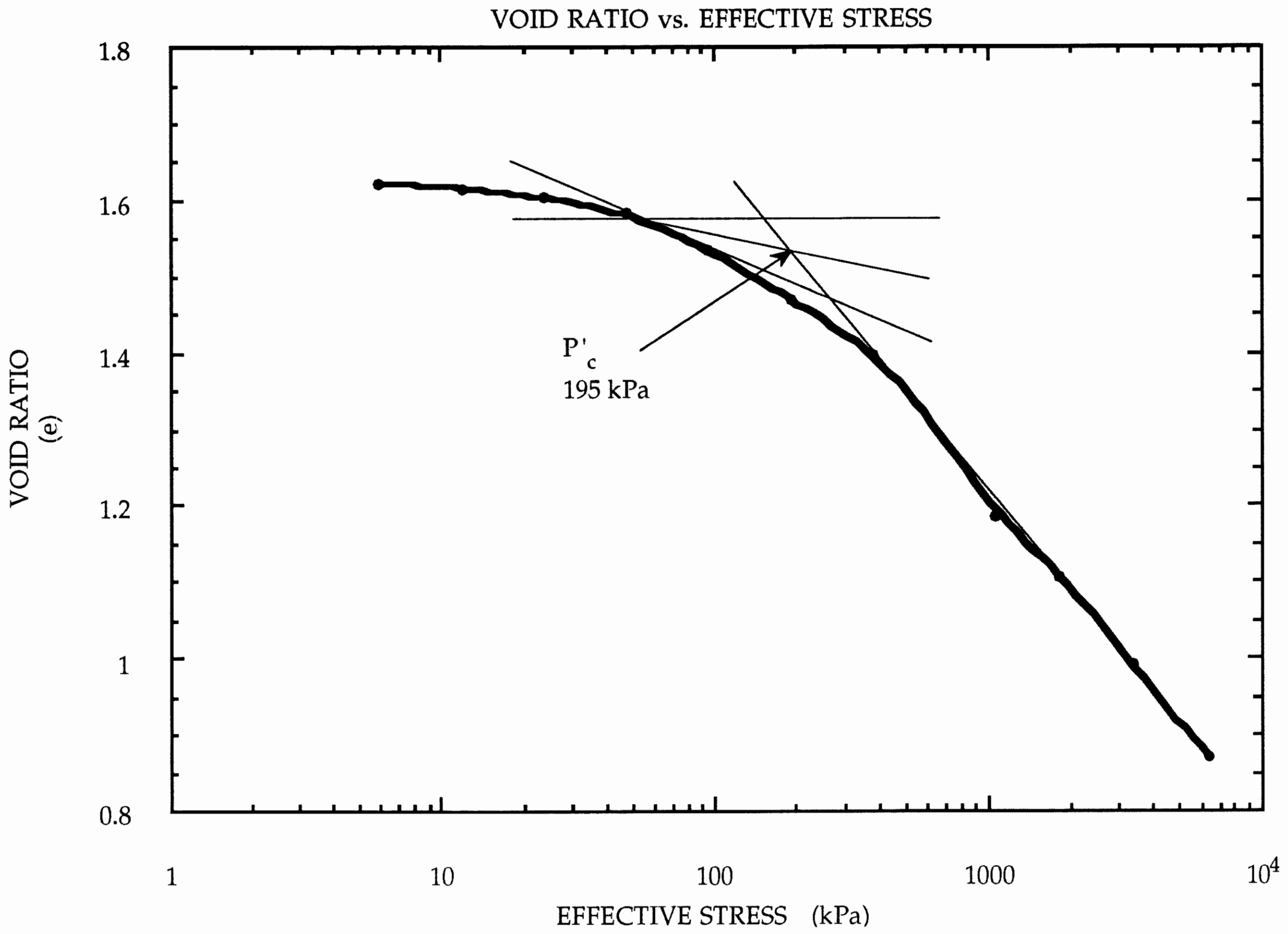

FIGURE 4.5. The Casagrande construction for sample 4x03, ODP Site 892D. The preconsolidation stress (labelled P_c') determined by this construction is approximately 195 kPa, at a void ratio of 1.53.

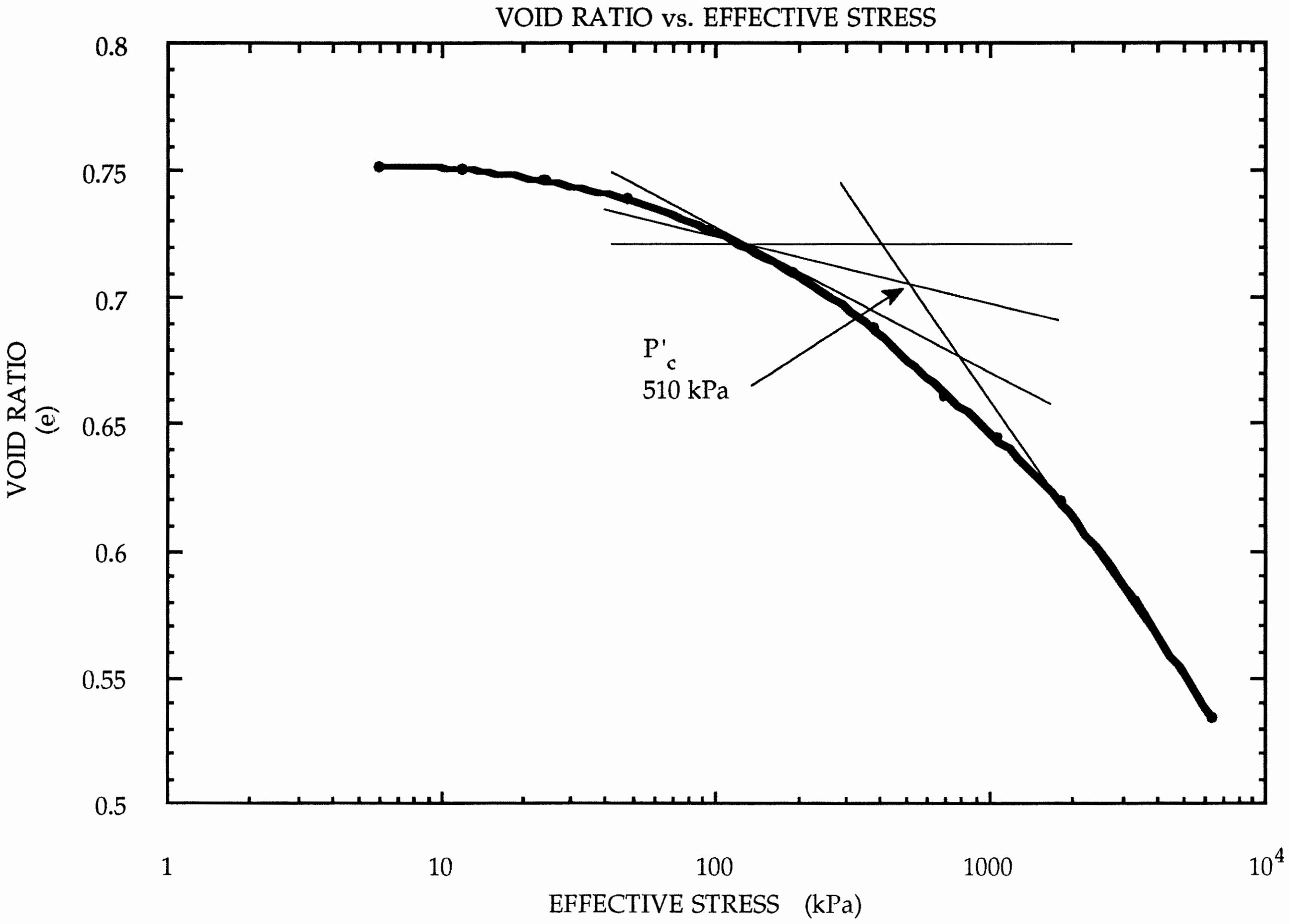

FIGURE 4.6. The Casagrande construction for sample 39x02, ODP Site 891B. The preconsolidation stress (labelled P_c') determined by this construction is approximately 510 kPa, at a void ratio of 0.70.

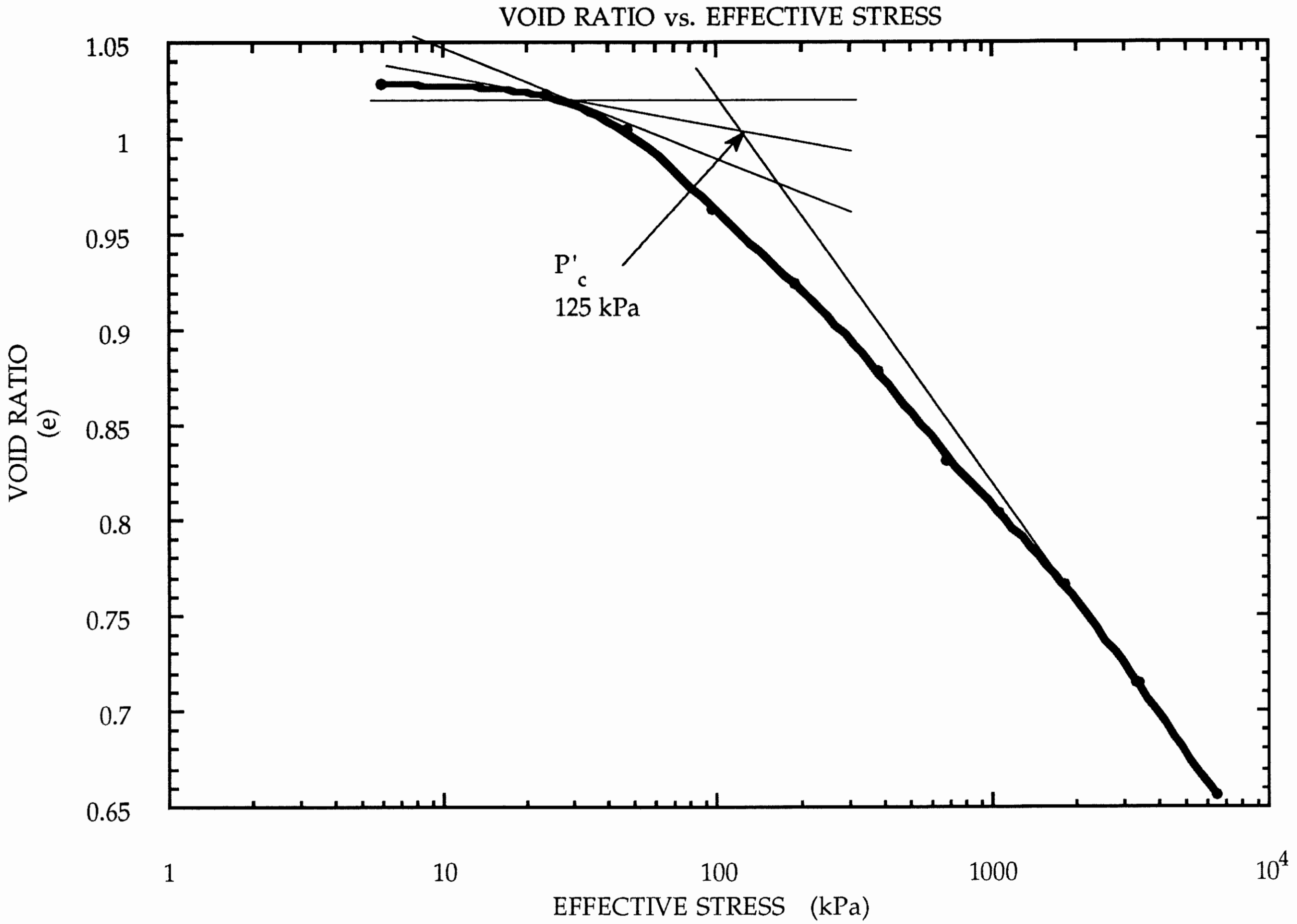

FIGURE 4.7. The Casagrande construction for sample 56x02, ODP Site 891B. The preconsolidation stress (labelled P_c') determined by this construction is approximately 125 kPa, at a void ratio of 1.00.

derived using Casagrande's construction for each sample. The constructions used to determine P_c' for each sample tested are shown in Figures 4.5 - 4.7.

4.3.3 Overconsolidation Ratio

The overconsolidation ratio, or OCR, is the ratio of the preconsolidation stress (P_c') to the vertical effective overburden stress (P_o'). Normally consolidated materials yield OCR values of 1, as detailed in Section3.3.3, whereas values of less than 1 indicate underconsolidated sediment, and greater than 1 indicate overconsolidated sediment.

Table 4.5 lists the preconsolidation stress, vertical effective overburden stress, and the resulting overconsolidation ratio for each sample.

Sample	892D 4x03	891B 39x02	891B 56x02
Pc'	195 kPa	510 kPa	125 kPa
Po'	195 kPa	3063 kPa	4655 kPa
OCR	1.00	0.167	0.027

TABLE 4.5. List of preconsolidation stresses (P_c'), vertical effective overburden stresses (P_o') , and OCR for each sample tested in this study.

The OCR values indicate normal consolidation in sample 4x03, located 30 mbsf at Site 892D, within an accreted thrust-bound unit. The Site 891B samples have OCR values that indicate significant underconsolidation exists at (at least) the intervals 297 mbsf and 447 mbsf.

4.4 LABORATORY PERMEABILITY TESTING

Permeability data in this study comes from two methods. The first method is the calculation of permeability from coefficient of consolidation (c_v) values. This method requires several assumptions regarding initial conditions (Sect. 3.3.4), which increases the margin of error surrounding the calculated permeability values. The second method utilized in this study is to induce fluid flow through a sample and record the pressure head developed. The combination of recorded pressure data, flow rates and sample area allow the calculation of permeability. As this method uses only common assumptions (for example, laminar flow) and measures all variables, this method provides greater accuracy.

4.4.1 Estimated Permeabilities

The calculation of permeability from c_v values follows the procedures outlined in Section 3.3.5. In particular, Equation 3.16 calculates hydraulic conductivity from consolidation test data. Table 4.6 lists the permeability values which result from analysis of c_v data for each effective stress increment.

4.4.2 Measured Permeabilities

The use of a micro-pump connected to the consolidometer unit allows samples to be tested for permeability, at various stress increments, by

Sample	892D 4x03	891B 39x02	891B 56x02
Depth (mbsf)	30.45	296.61	447.23
effective stress	*K (cm/s)*	*K (cm/s)*	*K (cm/s)*
6	8.48E-06	1.26E-05	1.26E-05
12	2.25E-07	1.54E-07	n/a
24	2.73E-07	2.02E-07	4.24E-07
48	1.79E-07	1.49E-07	3.27E-07
96	1.30E-07	9.35E-08	3.31E-07
192	8.07E-08	6.40E-08	1.09E-07
384	4.49E-08	4.09E-08	5.00E-08
768	4.95E-08	1.49E-08	1.17E-08
1536	9.52E-09	1.28E-08	7.28E-09
3072	3.97E-09	6.98E-09	5.42E-09
6144	2.36E-09	4.57E-09	4.40E-09
1536	1.09E-09	8.50E-10	1.70E-09
384	1.85E-09	4.46E-09	2.95E-09
96	2.99E-09	1.19E-08	8.49E-09
24	6.00E-09	2.53E-08	3.50E-08
6	1.32E-08	6.55E-08	1.08E-07

TABLE 4.6. Hydraulic conductivity data (*K*), estimated from consolidation test data, for each effective stress increment.

inducing a precisely metered flow rate across the sample and recording the pressure head which develops. This equipment configuration is referred to as a flow-pump permeameter in this study, following recent examples (Taylor and Fisher 1993). During this study, 104 permeability tests were performed over 8 effective stress intervals. Table 4.7 details the data resulting from these tests. Appendix B presents graphical analysis of the data in Table 4.7. This analysis indicates that the data are consistent. The graphs in Appendix B plot the differential pressure measured by the transducer (Fig. 3.4) against the induced flow rate. Linear least-squares fitting applied to the data points of these graphs producing best fit lines defined by the equation provided in the

Leg 146 892D 4x03 53-58 cm				Leg 146 891B 56x02 65-70 cm				Leg 146 891B 39x02 18-23 cm			
effective stress (kPa)	flow rate (ml/hr)	measured pressure (kPa)	pressure head (cm)	effective stress (kPa)	flow rate (ml/hr)	measured pressure (kPa)	pressure head (cm)	effective stress (kPa)	flow rate (ml/hr)	measured pressure (kPa)	pressure head (cm)
24	-0.200	-0.41	-0.040	48	-2.000	-1.12	-0.110	48	-3.000	-0.51	-0.050
24	0.200	-0.27	-0.026	48	2.000	-0.71	-0.070	48	3.000	-1.06	-0.104
24	-0.400	-0.48	-0.047	48	-1.000	-0.85	-0.083	48	-2.000	-0.98	-0.096
24	0.400	-0.18	-0.018	48	1.000	-0.79	-0.077	48	2.000	-0.79	-0.077
24	-0.600	-0.54	-0.053	48	-3.000	-1.15	-0.113	48	-4.000	-1.09	-0.107
24	0.600	-0.10	-0.010	48	3.000	-0.40	-0.039	48	4.000	-0.69	-0.067
192	-0.200	-1.60	-0.157	48	-4.000	-1.24	-0.122	768	-2.000	-3.40	-0.333
192	0.200	0.59	0.058	48	4.000	-0.09	-0.009	768	2.000	4.28	0.420
192	-0.300	-0.20	-0.019	384	-0.500	-1.60	-0.157	768	-1.500	-2.60	-0.255
192	0.300	0.97	0.095	384	0.500	-0.40	-0.039	768	1.500	1.79	0.175
192	-0.400	-2.98	-0.292	768	-0.150	-31.07	-3.046	768	-2.500	-4.20	-0.412
192	0.400	1.83	0.179	768	0.150	22.58	2.214	768	2.500	6.45	0.632
384	-0.200	-6.91	-0.677	768	-0.100	-12.00	-1.176	1536	-1.000	-2.00	-0.196
384	0.200	4.61	0.452	768	0.100	15.10	1.480	1536	1.000	5.90	0.578
384	-0.400	-12.40	-1.216	768	-0.050	-10.53	-1.032	1536	-1.500	-12.70	-1.245
384	0.400	10.86	1.065	768	0.050	6.20	0.608	1536	1.500	7.50	0.735
384	-0.600	-19.93	-1.954	1536	-0.100	-28.20	-2.764	1536	-2.000	-13.00	-1.274
384	0.600	17.40	1.706	1536	0.100	24.44	2.396	1536	2.000	17.40	1.706
768	-0.300	-31.00	-3.039	1536	-0.075	-20.40	-2.000	3072	-1.000	-33.50	-3.284
768	0.300	26.03	2.552	1536	0.075	18.64	1.827	3072	1.000	40.00	3.921
768	-0.250	-33.50	-3.284	1536	-0.050	-14.11	-1.383	3072	-0.750	-27.00	-2.647
768	0.250	23.00	2.255	1536	0.050	12.51	1.226	3072	0.750	21.60	2.117
768	-0.150	-16.15	-1.583	3072	-0.050	-26.20	-2.568	3072	-0.500	-19.30	-1.892
768	0.150	12.35	1.210	3072	0.050	24.16	2.368	3072	0.500	12.30	1.206
1536	-0.150	-27.30	-2.676	3072	-0.040	-20.20	-1.980	6144	-0.200	-27.50	-2.696
1536	0.150	23.46	2.300	3072	0.040	20.30	1.990	6144	0.200	25.50	2.500
1536	-0.100	-20.15	-1.975	3072	-0.030	-17.50	-1.716	6144	-0.150	-22.00	-2.157
1536	0.100	13.23	1.297	3072	0.030	15.80	1.549	6144	0.150	27.00	2.647
1536	-0.050	-10.30	-1.010	6144	-0.010	-13.70	-1.343	6144	-0.100	-15.70	-1.539
1536	0.050	4.00	0.392	6144	0.010	14.00	1.372	6144	0.100	10.90	1.069
3072	-0.100	-34.08	-3.341	6144	-0.020	-20.80	-2.039				
3072	0.100	32.20	3.157	6144	0.020	23.00	2.255				
3072	-0.075	-27.34	-2.680	6144	-0.030	-29.90	-2.931				
3072	0.075	20.49	2.009	6144	0.030	32.60	3.196				
3072	-0.050	-19.50	-1.912								
3072	0.050	11.65	1.142								
6144	-0.040	-32.91	-3.226								
6144	0.040	39.00	3.823								
6144	-0.030	-27.80	-2.725								
6144	0.030	21.50	2.108								

TABLE 4.7. Flow rate - pressure data resulting from 104 flow-pump permeameter tests. Pressure is measured in kPa by a differential pressure transducer, values are listed. Values are converted into pressure head in cm of water to facilitate calculation of hydraulic conductivity.

bottom right corner of each graph. The value R is the correlation coefficient of these lines - in all cases R is greater than 0.95, suggesting that the data is of excellent quality.

The equation of the best fit line also provides the slope of the pressure-flow rate relationship. This value, M1 in the graphs, is used to calculate hydraulic conductivity as it represents the hydraulic gradient during each test. Refer to Section B.1 for detailed information. Equation 3.13 is used to calculate the hydraulic conductivities. Table 4.8 lists the 18 hydraulic conductivity values measured by the flow-pump permeameter testing.

Sample	892D 4x03	891B 39x02	891B 56x02
Depth (mbsf)	30.45	296.61	447.23
effective stress	*K (cm/s)*	*K (cm/s)*	*K (cm/s)*
24	4.20E-06		
48		3.29E-05	1.24E-05
192	2.48E-07		
384	4.52E-08		1.21E-06
768	1.23E-08	7.89E-07	8.56E-09
1536	7.04E-09	2.21E-07	5.23E-09
3072	3.33E-09	4.23E-08	2.56E-09
6144	1.13E-09	9.96E-09	1.14E-09

TABLE 4.8. Measured hydraulic conductivity (*K*) values resulting from flow-pump permeameter testing. Linear least-squares analysis of data indicates it is consistent.

4.5 SUMMARY

Physical property testing by the Shipboard Scientific Party during ODP Leg 146 identifies several major offsets within sampled cores. As lithologies at both Sites are relatively homogeneous, the cause of these offsets is restricted to tectonic processes. Support for this conclusion comes from the presence of shear zones within the cored sediments, and slickensides and polished surfaces on partially lithified mudstones.

Index property and shear strength testing identifies normal consolidation in the upper subunit of Site 892D. This conclusion is supported by the OCR of 1 identified by this study. Index property testing identifies subunit 1B of Site 891B as normal to underconsolidated, whereas shear strength testing indicates underconsolidation. OCR values of 0.167 from this study agree with the shear strength interpretation, identifying Subunit 1B as significantly underconsolidated. Index property and shear strength testing identifies Subunit 1C of Site 891B as highly underconsolidated. The OCR value of 0.027 supports this interpretation, indicating high levels of underconsolidation.

Packer permeability testing (Sect. 4.2.4) during Leg 146 indicated permeabilities on the order of 10^{-5} cm/second, within sediment approximately 75 - 100 mbsf. This value is within the permeability values estimated and measured by this study. This study identifies a permeability range from approximately 10^{-5} cm/second to 10^{-10} cm/second, over a void ratio range of approximately 1.62 to 0.53.

There is a disparity between the results of the two methods used to determine permeability values in this study. This disparity results largely from the fact that consolidation analysis averages permeability over a wide stress range, introducing changing permeability conditions as a factor.

CHAPTER 5: INTERPRETATION AND DISCUSSION

5.1 INTRODUCTION

This chapter presents an interpretation discussion of the results of this study. Given particular attention is the role of excess pore pressure, a concept introduced in this chapter.

5.2 CONSOLIDATION TEST COEFFICIENTS

Analysis of consolidation test data determines the coefficient of consolidation, described in Section 3.3.4.1. This coefficient, c_v, is used in this study to calculate permeability, as detailed in Section 3.3.5. However, several other important coefficients exist that depend on sediment properties, and analysis of consolidation test data determines these coefficients as well.

The compression index, C_c, described in Section 3.3.4.3, represents the slope of the virgin compression curve. This value is defined by the relationship between void ratio and effective stress, and is significant for predicting the porosity-depth behaviour of sediment. Compression index values are of particular interest for post-Leg analysis of data. Values calculated for this study (Table 5.1) are in close agreement with empirically derived equations for silty clays (Haltz and Kovacs 1981).

A second useful coefficient is that of elastic rebound (Sect.3.3.4.3), which can be utilized to correct shipboard physical properties data to *in situ* conditions. Elastic rebound in this study is denoted by C_r, and should not be confused with the recompression coefficient, which is not calculated in this study. A simple method of determining both C_c and C_r values is to find the difference in void ratio for each portion of the curve over one log cycle. Figure 5.1, 5.2, and 5.3 plot void ratio against log of effective stress for samples 892D 4x03, 891B 39x02, and 891B 56x02, respectively. These figures show the logarithmic regression equations for each virgin compression and elastic rebound curve. The slope of the regression line for the virgin compression curve representsC_c, and the slope of the regression line for the elastic rebound curve represents C_r. Table 5.1 summarizes the results of these plots.

Sample	Cc	Cr	Cc regression equation	Cr regression equation
892D 4x03	0.42	0.065	e = logP'(-.42)+2.48	e =log P'(-.065)+1.12
891B 39x02	0.13	0.028	e = logP'(-.13)+1.04	e = logP'(-.028)+0.64
891B 56x02	0.17	0.036	e = logP'(-.17)+1.33	e = logP'(-.036)+0.79

TABLE 5.1. Summary of C_c and C_r data determined in Figures 5.1, 5.2 and 5.3. Regression equations relate effective stress (P') to void ratio (e).

5.3 HYDRAULIC CONDUCTIVITIES

5.3.1 *In Situ* Hydraulic Conductivity

Identification of the point where the hydraulic conductivity-effective stress relationship becomes representative of *in situ* conditions is necessary to determine the hydraulic conductivity of samples before their removal by coring. As an approximation, the P_c' value determined by the Casagrande construction relates to the *in situ* void ratio. From this void ratio, the corresponding hydraulic conductivity value is read from a plot of void ratio against the log of hydraulic conductivity. Figures 4.5, 4.6, and 4.7, determine P_c' values for each sample, and from these plots, void ratio values of 1.53, 0.70, and 1.00, are derived for samples 892D 4x03, 891B 39x02, and 891B 56x02, respectively. Figure 5.4 displays void ratio plotted against the log of hydraulic conductivity. Semi-logarithmic best-fit lines are plotted through the data points. Where these best fit lines intersect the respective void ratio of each sample is interpreted as the *in situ* hydraulic conductivity. Table 5.2 summarizes the values obtained from Figure 5.4.

Sample	892D 4x03	891B 39x02	891B 56x02
K (cm/s)	7.4 x 10-7 cm/s	6.56 x 10-6 cm/s	1.73 x 10-5 cm/s
e	1.53	0.70	1.00

TABLE 5.2. Interpreted *in situ* hydraulic conductivity values based on Pc' void ratio plotted against measured hydraulic conductivity values.

5.3.2 Comparison Of Calculated And Measured Values

This study utilizes two methods of determining hydraulic conductivities. The flow-pump permeameter method measures hydraulic conductivity directly, whereas consolidation test height analysis only indirectly estimates it. Flow-pump permeameter values are, as a result, considered more accurate, and require fewer assumptions. Comparisons between the two data sets are provided in Table 5.3. Ratios of calculated to measured values reported from previous work are in the range of 0.4 to 0.55

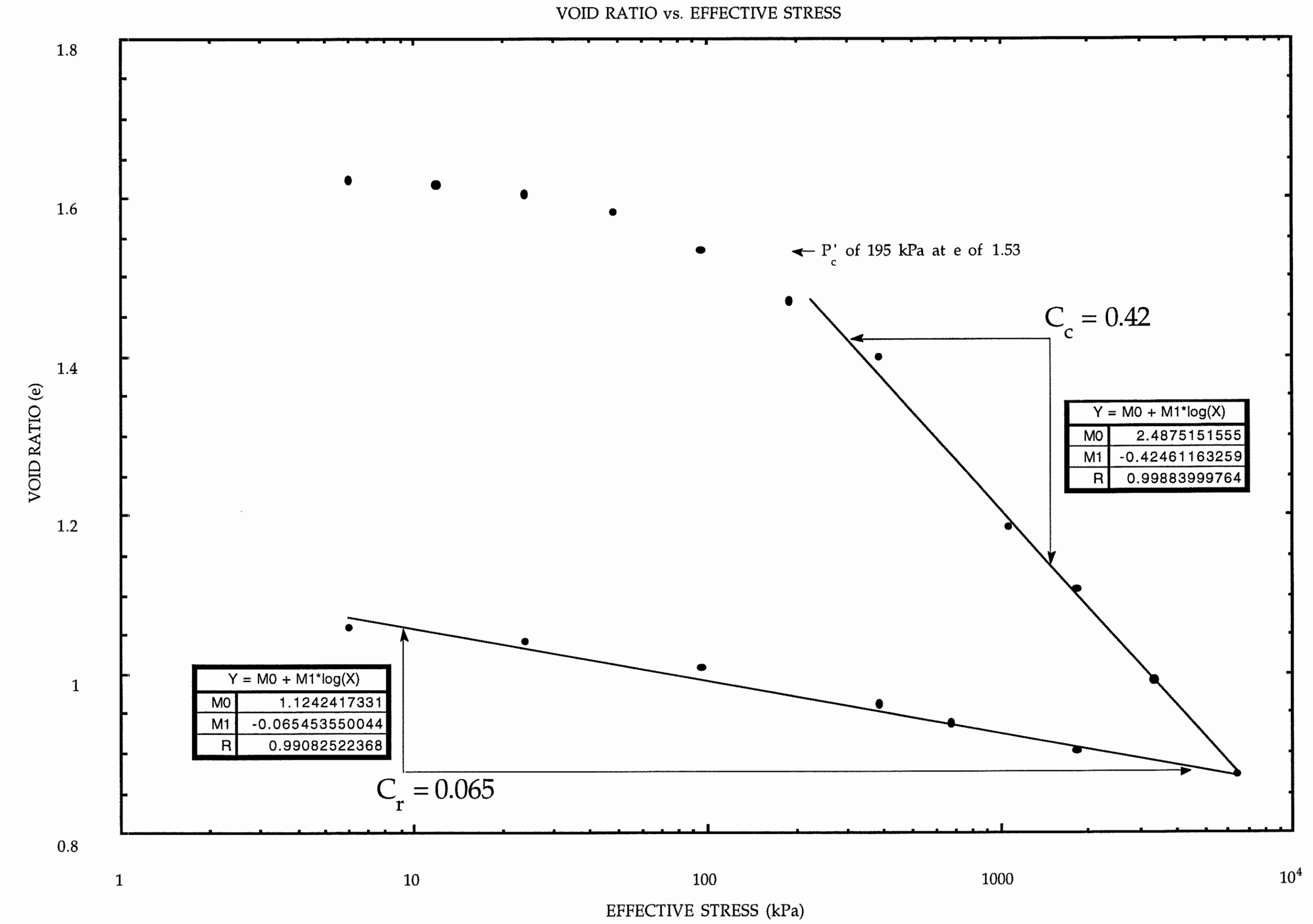

FIGURE 5.1. Void ratio vs. effective stress plot for sample 4x03, Site 892D. The slopes of the virgin compression and rebound curves provide compression index and elastic rebound coefficients. Boxes detail logarithmic regression lines.

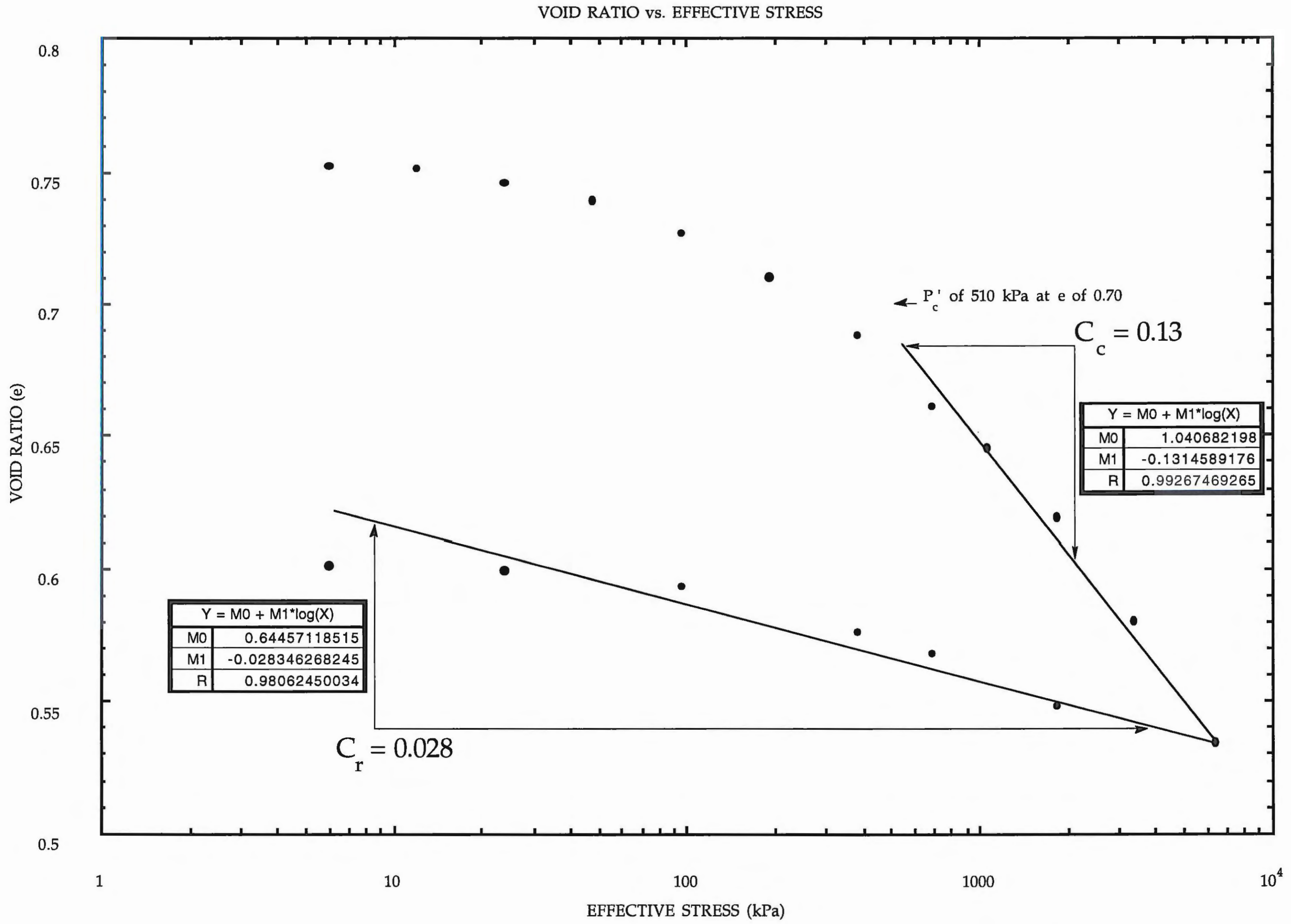

FIGURE 5.2. Void ratio vs. effective stress plot for sample 39x02, Site 891B. The slopes of the virgin compression and rebound curves provide compression index and elastic rebound coefficients. Boxes detail logarithmic regression lines.

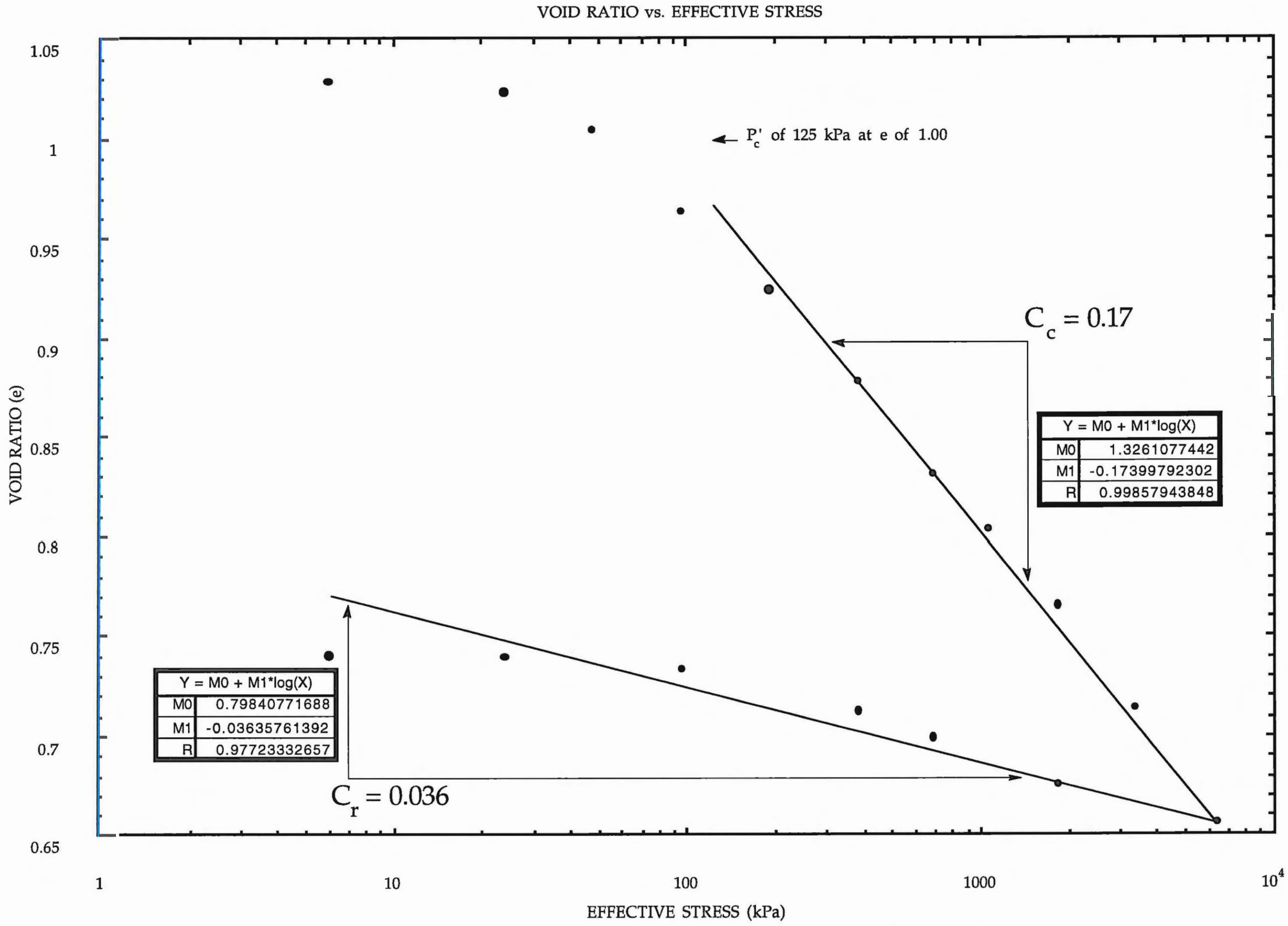

FIGURE 5.3. Void ratio vs. effective stress plot for sample 56x02, Site 891B. The slopes of the virgin compression and rebound curves provide compression index and elastic rebound coefficients. Boxes detail logarithmic regression lines.

(Clukey and Silva 1981). In this study, calculated values in general tend to be either lower than the measured values, or fairly similar, with two notable exceptions. Other than these exceptions, the ratios vary inversely with increasing effective stress. Figure 5.5 shows the measured hydraulic conductivity values as solid symbols and the calculated values as open symbols.

5.3.3 Comparison With Packer Test Permeability

ODP Leg 146 installed a packer device at Site 892 to test permeability, as detailed in Section 4.2.4. The interval tested ran from approximately 106 to 179 mbsf. This depth corresponds with P_0' values of between 825 kPa and 1350 kPa. If an intermediate value of approximately 1075 kPa is assumed, the corresponding void ratio is 1.19 (Fig. 5.1). At this void ratio, expected hydraulic conductivity is approximately 1.8 x 10^{-8} cm/s (Fig. 5.4). The order of 10^{-5} cm/s determined during Leg 146 (Screaton 1994), therefore, appears high. However, the large interval sampled undoubtedly included many fractures, which may have permeabilities orders of magnitude higher than the formation permeability of unfractured sediment (Moore and Vrolijk 1992), suggesting the packer results are, as expected, representative of bulk permeability.

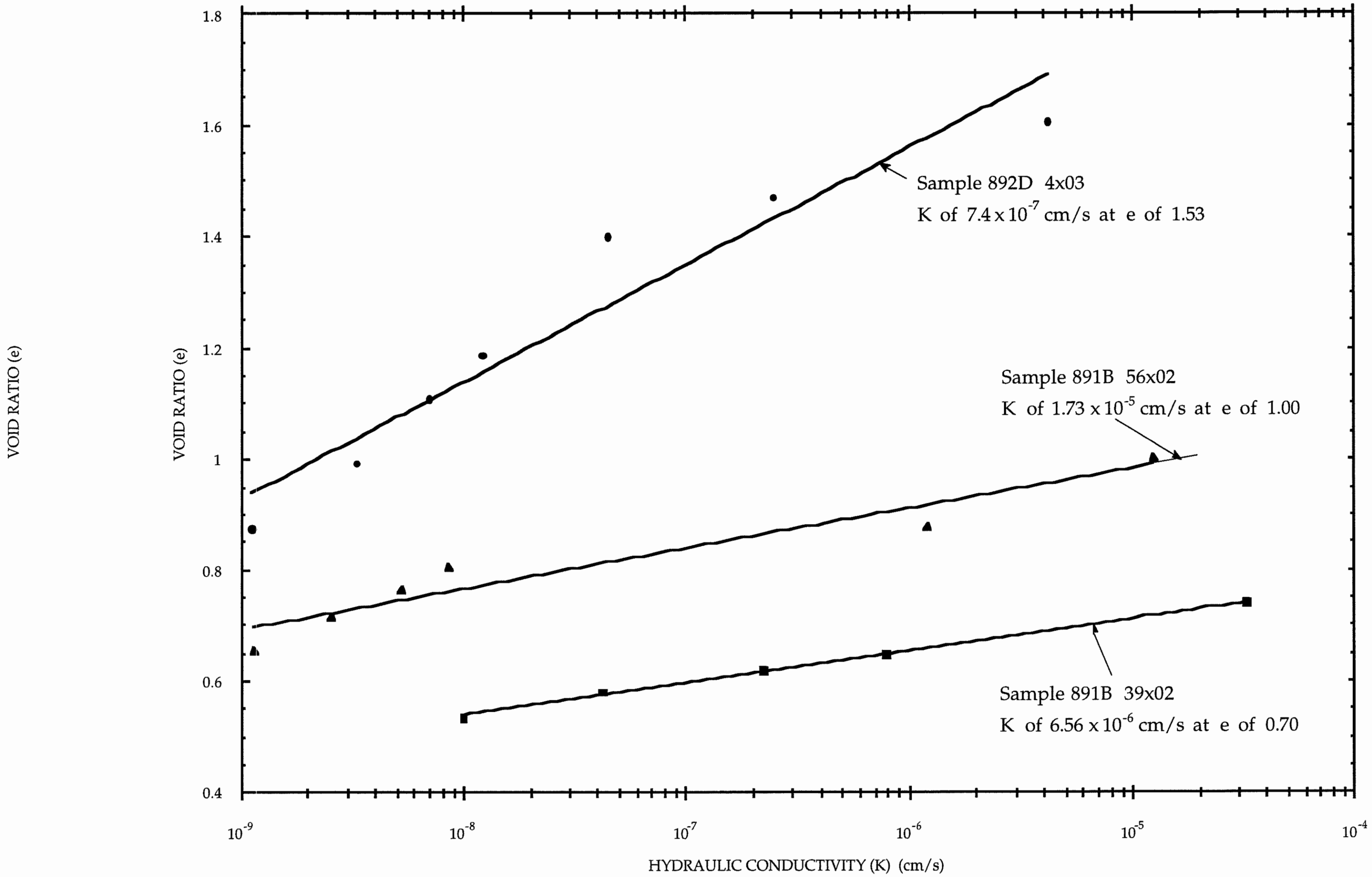

FIGURE 5.4. Void ratio vs. hydraulic conductivity for all samples. *In situ* hydraulic conductivities are determined by plotting the void ratios at the P_c' values for each sample. Both K values and corresponding e values are identified.

Sample 892D 4x03			
void ratio	measured K	estimated K	ratio est./meas.
1.622	-	8.48E-06	-
1.616	-	2.25E-07	-
1.604	4.20E-06	2.73E-07	0.07
1.582	-	1.79E-07	-
1.534	-	1.30E-07	-
1.469	2.48E-07	8.07E-08	0.33
1.398	4.52E-08	4.49E-08	0.99
1.185	1.23E-08	4.95E-08	4.02
1.107	7.04E-09	9.52E-09	1.35
0.991	3.33E-09	3.97E-09	1.19
0.872	1.13E-09	2.36E-09	2.09

Sample 891B 39x02			
void ratio	measured K	estimated K	ratio est./meas.
1.028	-	1.26E-05	-
1.023	-	4.24E-07	-
1.004	1.24E-05	3.27E-07	0.03
0.963	-	3.31E-07	-
0.924	-	1.09E-07	-
0.878	1.21E-06	5.00E-08	0.04
0.803	8.56E-09	1.17E-08	1.37
0.765	5.23E-09	7.28E-09	1.39
0.714	2.56E-09	5.42E-09	2.12
0.656	1.14E-09	4.40E-09	3.86

Sample 891B 56x02			
void ratio	measured K	estimated K	ratio est./meas.
0.752	-	1.26E-05	-
0.751	-	1.54E-07	-
0.746	-	2.02E-07	-
0.739	3.29E-05	1.49E-07	0.005
0.727	-	9.35E-08	-
0.71	-	6.40E-08	-
0.688	-	4.09E-08	-
0.645	7.89E-07	1.49E-08	0.02
0.619	2.21E-07	1.28E-08	0.06
0.58	4.23E-08	6.98E-09	0.17
0.534	9.96E-09	4.57E-09	0.46

TABLE 5.3. Comparison of measured and estimated hydraulic conductivities. Previous workers report ratios of estimated to measured values of 0.4 to 0.55. In general, estimated values are less than or equal to measured values.

5.4 RESULTS IN SITE CONTEXT: THE EFFECTS OF PORE PRESSURE

As discussed in Section 3.3.1, consolidation requires fluid expulsion, which is governed by permeability. Consolidation is a time-dependent phenomenon, and permeability greatly influences the rate of consolidation. In general, sediments of low permeability undergo low rates of consolidation. In addition to a sediment's interparticulate permeability, however, the bulk permeability over a large depth interval also governs consolidation. This bulk permeability is affected by fractures, faulting, and other large scale heterogeneities. The overall, or effective, permeability of a depth interval depends on both the bulk and the interparticulate permeability, but the former is of greater consequence as a result of the role of excess pore pressure. Excess pore pressures act to keep fractures open, preserving higher than expected permeabilities within a sediment package.

Pore pressure is the pressure developed within the void spaces of a material as a result of loading stresses. These loading stresses are produced by the mass of overlying sediment, overlying fluids, and any tectonically induced stresses. Normal pore pressure is calculated by multiplying the height of overlying water column and saturated sediments times $\rho_w g$. Pressures in excess of hydrostatic pressures develop loading occurs, and fluids are prevented from escaping. In saturated sediment, pore pressure is entirely transmitted by the pore fluid, as a consequence of its incompressibility. As a result, dissipation of excess pore pressure only results from the expulsion of

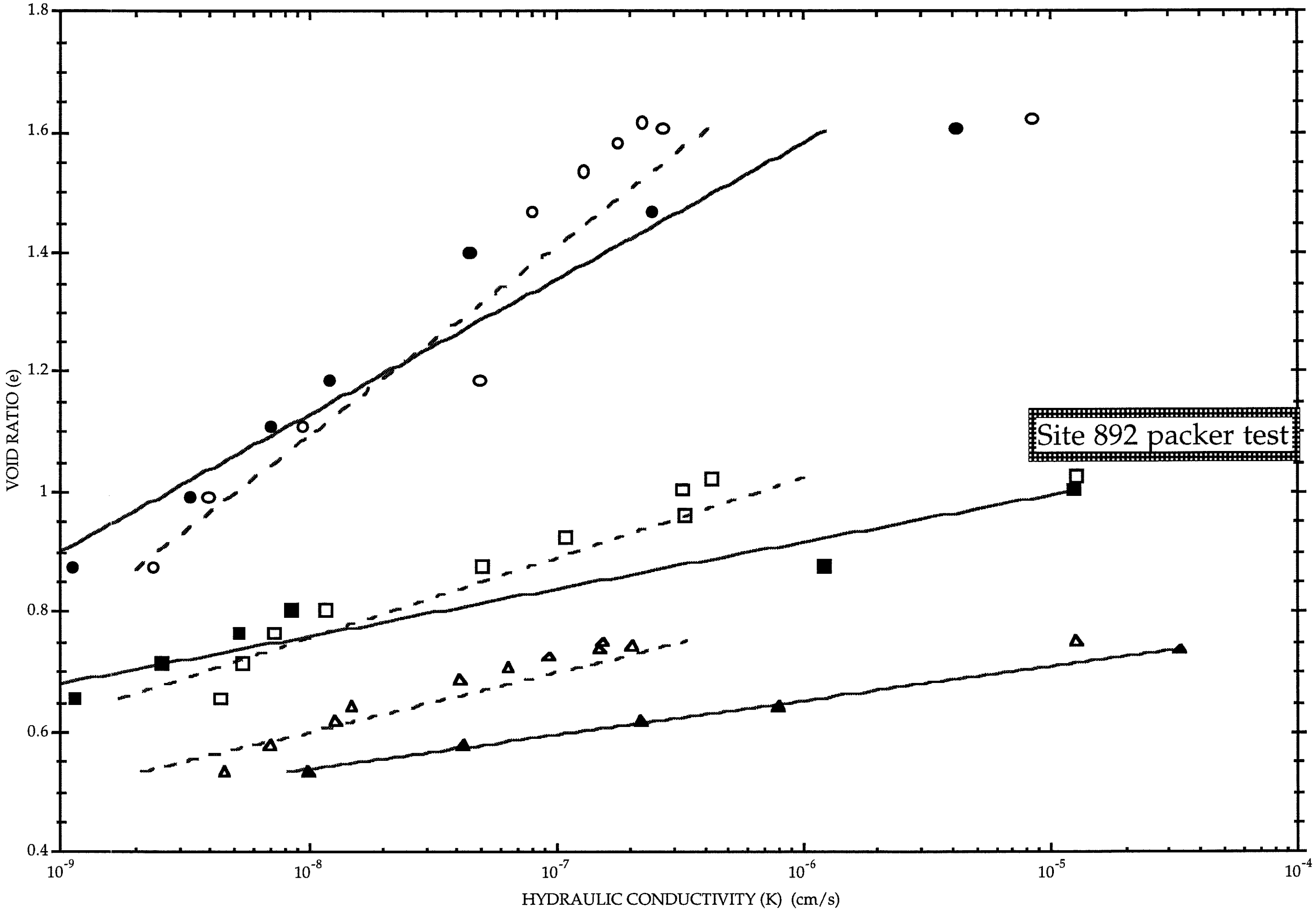

FIGURE 5.5. Void ratio vs. both measured and calculated hydraulic conductivity for all samples. Solid symbols are measured values, with circles representing sample 892D 4x03, squares 891B 56x02, and triangles 891B 39x02.

pore fluids. The permeability of loaded sediments governs the rate of expulsion of these pore fluids.

Index property testing, detailed in Section 4.2, identifies several porosity offsets not coincident with observed faulting or lithostratigraphic changes. The offsets form two categories: drained boundaries, characterized by increasing porosity vertically away from the boundary; and sealed boundaries, characterized by transitions from lower porosity above the boundary to higher porosity below (Fig. 5.6). Drained boundaries are zones of high permeability, capable of transmitting fluid relatively easily, whereas sealed boundaries are zones of low permeability, and do not pass fluids easily. Insight into the permeability of these boundaries allows interpretation of porosity trends and OCR values, in light of the influence of excess pore pressures.

5.4.1 Overconsolidation Ratios In Context

As discussed in Section 3.3.3, the overconsolidation ratios derived for each sample are useful indicators of consolidation state. More useful insight into *in situ* conditions results when the OCR is put into context. Consolidation is time-dependent, and with sufficient time, OCR values should approach 1. Exceptions can occur in overconsolidated sediment, as the inelastic component of deformation may preclude reaching an OCR of 1. Given enough time, however, underconsolidated sediments will eventually reach equilibrium with their environment, resulting in an OCR of 1.

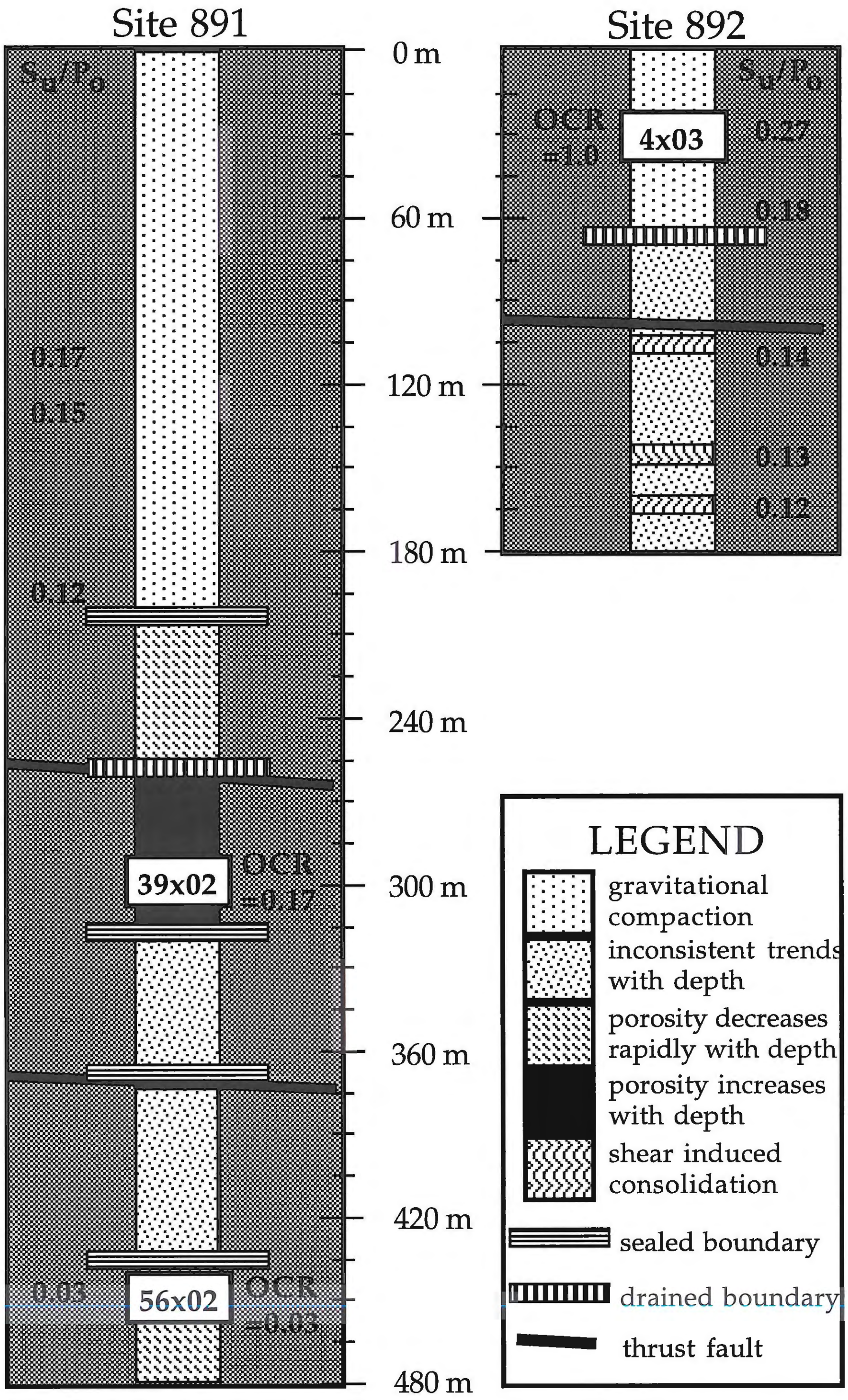

FIGURE 5.6. Sample locations within the context of structural features and index property trends. Symbols are as indicated in the legend. Sample 4x03 represents a normally consolidated unit, 39x02 an underconsolidated but drained unit, and 56x02 a highly underconsolidated sealed unit.

5.4.1.1 Sample 4x03, Site 892D

Sample 4x03 of Site 892D exhibits an OCR of 1.0 and S_u / P_o ratios of 0.27, which indicate normal consolidation. The sediments of the second ridge consist of an accreted, thrust-bounded package of Pliocene basin fill (Sect. 2.4.3, Fig. 2.5). However, sample 4x03, at a depth of only 30.45 mbsf, does not represent these older accreted materials, and instead consists of material deposited subsequent to the uplift of the second ridge. As such, however, this material is representative of the basin sediments before accretion. This interpretation allows the use of results from this sample as a reference point for interpreting accretion-related changes in the other samples. Based on OCR and S_u / P_o values resulting from this study, the basin sediments before accretion were normally consolidated. This conclusion is important, and not as obvious as it may appear. For example, ODP Leg 146 cored sediments within the basin fill (Site 888) with the aim of establishing a pre-accretion reference data set. These reference sediments, however, are underconsolidated, possibly, as some data suggests, a result of rapid sedimentation (Moran 1994 pers comm). This disparity in consolidation state suggests a difference in sedimentation rates, permeabilities or tectonic stress loading between sites, or perhaps some combination of these factors.

5.4.1.2 Sample 39x02, Site 891B

Consolidation testing of Sample 39x02, from a depth of 296.6 mbsf, yielded an OCR of 0.17. This OCR value suggests a high state of underconsolidation exists at this depth. Figure 5.6 illustrates the presence of a thrust fault approximately 30 metres above sample 39x02, indicating that this sample consists of underthrust sediments. The process of being underthrust results in increased thicknesses of overburden, and consequently increased load stresses. These increased load stresses develop excess pore pressures if the loading occurs faster than the sediment permeability allows for their dissipation. The OCR of sample 39x02 indicates that loading occurred at this site faster than excess pore pressures could be dissipated. Therefore, permeability at this location is insufficient to allow dissipation of excess pore pressures, despite the drained boundary formed by the thrust fault, which may enhance the bulk permeability of this interval. Comparison with other regions suggests that permeabilities at this Site would require on the order of at least 10^3 years to dissipate excess pore pressures of the magnitude found at Site 891 (Moran 1994 pers comm).

5.4.1.3 Sample 56x02, Site 891B

Sample 56x02 occurs approximately 70 metres below the frontal thrust fault of the central Oregon margin. Consolidation testing of this sample yielded an OCR of 0.03. This low OCR suggests an extremely underconsolidated state exists at this depth. This corresponds with the increased loading experienced at this location from being overthrust twice, as illustrated in Figure 5.6. Moreover, the presence of a sealed boundary directly above the sample further reduces bulk permeability, already insufficient to dissipate the loading produced by only one overthrusting event (Sect. 5.4.1.2).

5.4.2 Excess Pore Pressure Values

Pore water pressures greater than the hydrostatic pressure are called excess pore pressures. Sediments displaying excess pore pressure are called overpressured. Calculation of excess pore pressure is accomplished by subtracting the preconsolidation stress (P_c') from the vertical effective overburden stress (P_0'). As the P_c' represents the maximum effective stress upon a sediment, the stress difference between it and the P_0' must be supported by the pore fluid, in excess of hydrostatic pressure. Excess pore pressure values are listed in Table 5.4.

Sample	Pc' (kPa)	Po' (kPa)	Excess pore pressure
892D 4x03	195	195	0 MPa
891B 39x02	510	3063	2.5 MPa
891B 56x02	125	4655	4.5 MPa

TABLE 5.4. Excess pore pressure values for sample sediments. Figure 5.6 shows locations.

At Site 892D, sample 4x03 exhibits a P_0' value of 195 kPa, and a P_c' value also of 195 kPa. Therefore, no excess pore pressure is present at this location. The underconsolidated materials of Site 891B exhibit different results. Sample 39x02 yielded a P_0' value 3063 kpa and a P_c' value of only 510 kPa. The difference, over 2.5 MPa, represents the excess pore pressure. Sample

56x02 produced a P_o' of 4655 kPa and a P_c' of only 125 kPa, resulting in a large 4.5 MPa excess pore pressure.

The increase in excess pore pressure apparent from this study shows a relationship to the sample loading, as sample 39x02 has been overthrust once, whereas 56x02 has been overthrust twice. This relationship supports models of excess pore pressure generation that place more emphasis on tectonic loading, rather than tectonic compression, as the largest factor influencing overpressure generation (Shi and Wang 1988).

Excess pore pressures of this magnitude can reduce vertical effective stresses to nearly zero, resulting in a loss of frictional cohesion between sediment grains. Hubbert and Rubey (1959) suggested this loss of cohesion as a mechanism for large thrust block movement, occuring as pore pressures approach lithostatic values. To evaluate pore pressure conditions, Hubbert and Rubey define a pore pressure parameter, calculated as the ratio of pore pressure over the lithostatic stress. When the pore pressure parameter, λ, reaches a value of 1, sediment is at failure conditions.

Coulomb wedge modelling by Davis et al. (1983) predict values of λ at the décollement of 0.90 for the Oregon margin, based on its geometry. Results from this study (excess pore pressures of 2.5 MPa and 4.5MPa) produce values of λ of 0.83 for sample 39x02 and 0.97 for sample 56x02. Sample 56x02 occurs approximately 70 metres from the frontal thrust, and values for λ decrease away from the décollement (Shi and Wang 1988). This pattern of decrease suggests that the décollement region impedes fluid flow, and that the depth interval at sample 56x02 is very close to sediment failure. Moreover, these values suggest that deformation occurs early in the accretion history of accretionary prisms such as the Cascadia margin.

5.5 SUMMARY

The Casagrande construction allows the compression index, C_c, and the coefficient of elastic rebound, C_r, to be determined for each sample. The P_c' values determined by the Casagrande construction allow hydraulic conductivity values to be identified for *in situ* void ratios. These *in situ* hydraulic conductivity values range from 10^{-5} to 10^{-7} cm/s. Low OCR values indicate that the hydraulic conductivities values at Site 891 are insufficient to dissipate the excess pore pressures developed from tectonic loading. Sediments that have been overthrust once display excess pore pressure values of 2.5 MPa, and those having been overthrust twice display 4.5 MPa excess pore pressures. These pores pressures yield pore pressure parameter values of 0.83 to 0.97 (Hubbert and Rubey 1959). The latter number suggests the depth interval near sample 56x02 is close to failure conditions.

CHAPTER 6: SUMMARY AND CONCLUSIONS

6.1 INTRODUCTION

This study provides data useful for understanding the complex interrelationship of sediment permeability and consolidation. In particular, the samples used in this study represent the coarse-grained accretionary prism environment. Contrasts and comparisons between results of this study and those from fine-grained accretionary prisms will be helpful in evaluating the relative importance of grain size, permeability, and pore pressure on the geometry and development of accretionary prisms. Finally, this study provides data which may contribute insight into local phenomena at the central Oregon margin. In particular, permeability data are necessary to evaluate water budgets in accretionary prisms.

6.2 SUMMARY OF RESULTS AND CONCLUSIONS

Consolidation testing of three whole-round samples cored at the central Oregon convergent margin suggests that basin-fill sediments at Site 892 are normally consolidated, with OCR values of 1, whereas accreted Site 891 sediments at the base of the marginal ridges are highly underconsolidated, with OCR values of 0.17 to 0.03. These conclusions on consolidation state are also supported by index property trends and shear strength data.

Permeability testing of these samples reveals an *in situ* hydraulic conductivity range of 10^{-7} to 10^{-5} cm/s. The low OCR values indicate that this range of permeability is insufficient to dissipate pore pressures developed in the accreted samples. Low hydraulic conductivities result in excess pore pressures of 2.5 MPa in sample 39x02, from a depth of 296.6 mbsf within underthrust sediments. Values of 4.5 MPa are present at sample 56x02, from doubly underthrust sediments at 447.5 mbsf.

Pore pressure parameter (λ) values of up to 0.97 within 70 metres of the frontal thrust fault suggest that the sediment at this location is close to failure conditions, implying that deformation occurs early in the accretion history of sediment at the central Oregon margin.

6.3 RECOMMENDATIONS

During the course of this study, problems with the consolidometer unit developed that did not affect the accuracy of results, but required unanticipated efforts to correct. As a result, a calibration of consolidometer load chambers is prudent before consolidation testing begins, to allow instant use of data without correcting for frictional effects. During the course of testing, valuable information may result from applying a one increment unload-reload cycle within the virgin compression curve. This procedure adds only two increments to testing and will provide a check of C_c and C_r values, as these should match the values obtained from the entire test (Holtz and Kovacs 1981).

Future study opportunities for these sample materials include a detailed Environmental Scanning Electron Microscope (ESEM) study of grain relations and microfabrics. Combined with precise grain-size analysis, these data would be useful for estimating sediment permeabilities by means of the Kozeny-Carman Equation, and providing data on the validity of Darcy's Law in accreted, over-pressured silty clays.

REFERENCES

Athy LF (1930) Density, porosity, and compaction of sedimentary rocks. Bull Amer Assoc Petrol Geol 14:1-24

Bowles JE (1970) Engineering properties of soils and their measurement. McGraw Hill, Toronto

Brückmann WK (1989) Typische Kompakationsmuster mariner Sedimente und ihre Modifikation in einem rezenten Akkretionskeil (Barbados Ridge). Beitr Geol Inst Univ Tübingen, Rh. A, 5:1-135

Carson B (1977) Tectonically induced deformation of deep-sea sediments off Washington and northern Oregon: mechanical consolidation. Mar Geol 24:289-307

Casagrande A (1936) The determination of the pre-consolidation load and its practical significance, Discussion D-34. Proceedings of the First International Conference on Soil Mechanics and Foundation Engineering, Vol. III. Cambridge, pp. 60-64

Christian HA (1989) Operation manual for modified Geotest back pressured consolidometers A and B. Atlantic Geoscience Centre, Dartmouth

Clukey EC and Silva AJ (1982) Permeability of deep-sea clays: Northwestern Atlantic. Mar Geotechnology 5:1-25

Das BM (1989) Soil mechanics laboratory manual, third edition. Engineering Press, San Jose

Davis EE, Hyndman RD, Villinger H (1990) Rates of fluid expulsion across the northern Cascadia accretionary prism: Constraints from new heat flow and multichannel seismic reflection data. J Geophys Res 95:8869-8889

Davis D, Suppe J, Dahlen FA (1983) Mechanics of fold-and-thrust belts and accretionary wedges. J Geophys Res 88:1153-1172

Demets C, Gordon RG, Argus DF, Stein S (1990) Current plate motions. Geophys J Int 101:425-478

Hedberg HD (1936) Gravitational compaction of clays and shales. Amer J Sci 31:241-287

Holtz RD, Kovacs WD (1981) An introduction to geotechnical engineering. Prentice-Hall, Englewood Cliffs, New Jersey

Hubbert MK, Rubey WW (1959) Role of fluid pressure in the mechanics of overthrust faulting: I. Mechanics of fluid-filled porous solids and its application to overthrust faulting. Geol Soc Am Bull 70:115-166

Hyndman RD, Spence GD (1992) A seismic study of methane hydrate marine bottom simulating reflectors. J Geophys Res 97:6683-6698

Hyndman RD, Davis EE (1992) A mechanism for the formation of methane hydrate and seafloor bottom-simulating reflectors by vertical fluid expulsion. J Geophys Res 97:7025-7041

Kulm LD, Suess E, Moore JC, Carson B, Lewis BT and others (1986) Oregon subduction zone: venting, fauna, and carbonates. Science 231:561-566

Kulm LD, and others (eds) (1984) Western North American continental margin and adjacent floor off Oregon and Washington, Atlas 1, Ocean Margin Drilling Program, Regional Atlas Series. Marine Science International, Woods Hole

Langseth MG, Hobart A (1984) A marine geothermal study over deformed sediments of the subduction complex off Oregon and Washington. Eos, Trans Am Geophys Union 65:1089

Langseth MG, Moore JC (1990) Introduction to special section on the role of fluids in sediment accretion, deformation, diagenesis, and metamorphism in subduction zones. J Geophys Res 95:8737-8741

Lewis BTR, Cochrane GC (1990) Relationship between the location of chemosynthetic benthic communities and geologic structure on the Cascadia subduction zone. J Geophys Res 95:8783-8793

MacDonald GJ (1992) Clathrates. In: Encyclopedia of Earth System Science, Volume 1. Nierenberg WA (ed) Academic Press, New York

MacKay ME, Moore GF, Cochrane GR, Moore JC, Kulm LD (1992) Landward vergence and oblique structural trends in the Oregon margin accretionary prism: Implications and effect on fluid flow. Ear Planet Sci Let 109:477-491

MacKillop AK (1994) The application of consolidation results in a paleoceanographic study from the eastern equatorial Pacific Ocean. MASc thesis, Technical University of Nova Scotia

Mesri G (1975) Discussion of new design procedures for stability of soft clays. J Geotech Eng Division, ASCE 101 GT4:409-412

Moore JC, Brown KM, Horath F, Cochrane G, MacKay M, Moore GF (1991) Plumbing accretionary prisms: effects of permeability variations. Proc R Soc London 335:275-288

Moore JC, Lundberg N (1986) Tectonic overview of Deep Sea Drilling Project transects of forearcs. Geol Soc Amer, Memoir 166:1-12

Moore JC and Vrolijk P (1992) Fluids in accretionary prisms. Reviews of Geophysics 30:113-135

Moran K, Brückmann W, Feeser V, Campanella RG (1993) In-situ stress conditions at Nankai trough, Site 808. In: Proc. ODP Sci. Results, Vol. 131. Hill IA, Taira A, Firth JV and others (eds) Ocean Drilling Program, College Station, Texas, pp. 283-291

Penta-Pycnometer PP4 Operations Manual (1985) Quantachrome Corp., Syosset, N.Y.

Scheidegger KF, Krissek LA, Baba J (1984) Texture and mineralogy of continental margin sediments. In: Western North American continental margin and adjacent floor off Oregon and Washington, Atlas 1, Ocean Margin Drilling Program, Regional Atlas Series. Kulm, LD and others (eds) Marine Science International, Woods Hole, sheet 32

Scholl DW, von Heune R, Vallier TL, Howell DG (1980) Sedimentary masses and concepts about tectonic processes at underthrust ocean margins. Geology 8:564-568

Seely DR (1977) The significance of landward vergence and oblique structural trends on trench inner slopes. In: Island arcs, deep sea trenches, and back-arc basins. Talwani W, Pitman WC (eds) Am Geophys Union, Washington, pp. 187-198

Shi Y, Wang CY (1988) Generation of high pore pressures in accretionary prisms: Inferences from the Barbados Subduction Complex. J Geophys Res 93:8893-8910

Shipboard Scientific Party (1994) In: Proc. ODP Init. Repts. Vol. 146 (Pt. 1). Westbrook GK, Carson B, Musgrave RJ and others (eds) Ocean Drilling Program, College Station, Texas

Silver EA (1972) Pleistocene tectonic accretion of the continental slope off Washington. Mar Geol 13:239-249

Smith RC (1993) Physical and geotechnical properties report for Arctic '91 Cores 2185-5 and 2185-7. Unpublished report, Atlantic Geoscience Centre, Dartmouth

Taylor E, Fisher A (1993) Sediment permeability at the Nankai accretionary prism, Site 808. In: Proc. ODP Sci. Results, Vol. 131. Hill IA, Taira A, Firth JV and others (eds) Ocean Drilling Program, College Station, Texas, pp. 235-243

Taylor DW (1948) Fundamentals of soil mechanics. John Wiley and Sons, New York

Terzaghi K (1943) Theoretical soil mechanics. John Wiley and Sons, New York

APPENDIX A: TAYLOR'S SQUARE ROOT OF TIME METHOD

A.1. Taylor's Square Root of Time Fitting Method

Consolidation has two components, primary and secondary. The primary component of consolidation results from the dissipation of excess pore water pressure (Holtz and Kovacs, 1981), whereas secondary consolidation results from the deformation of sediment particles and is, therefore, of smaller magnitude and longer time scale. Recognizing that primary consolidation occurs relatively early, Taylor (1948) developed a method of graphical analysis for consolidation test height data based on the square root of time. Taylor's method is based on observations of the relationship between experimental and theoretical consolidation curves, when plotted versus the square root of time. This method distinguishes between the components of consolidation and identifies the point of 100% primary consolidation. The sample height at this point is required to calculate the void ratio at each stress increment, and the time at which 100% primary consolidation occurs is required to calculate the coefficient of consolidation.

This study uses Taylor's method as outlined in American Society of Testing and Materials (ASTM) D 2435 (1988), as illustrated in Figure A.1. The method consists of drawing a straight line through the initial part of the compression curve, extrapolating the line back to the ordinate axis where time = 0. This intercept represents U_0, the point of 0% primary consolidation. The first data points may not plot on this line as sample height can be affected by swelling and load pressure variations between tests. A second straight line is drawn from this intercept such that the abscissas are 1.15 times those of the first line. The intersection of this second line and the sample height curve represents U_{90}, the point of 90% primary consolidation. The abscissa at this point represents $\sqrt{t_{90}}$, the square root of time at 90% consolidation, whereas the ordinate represents H_{90}, the sample height at 90% consolidation.

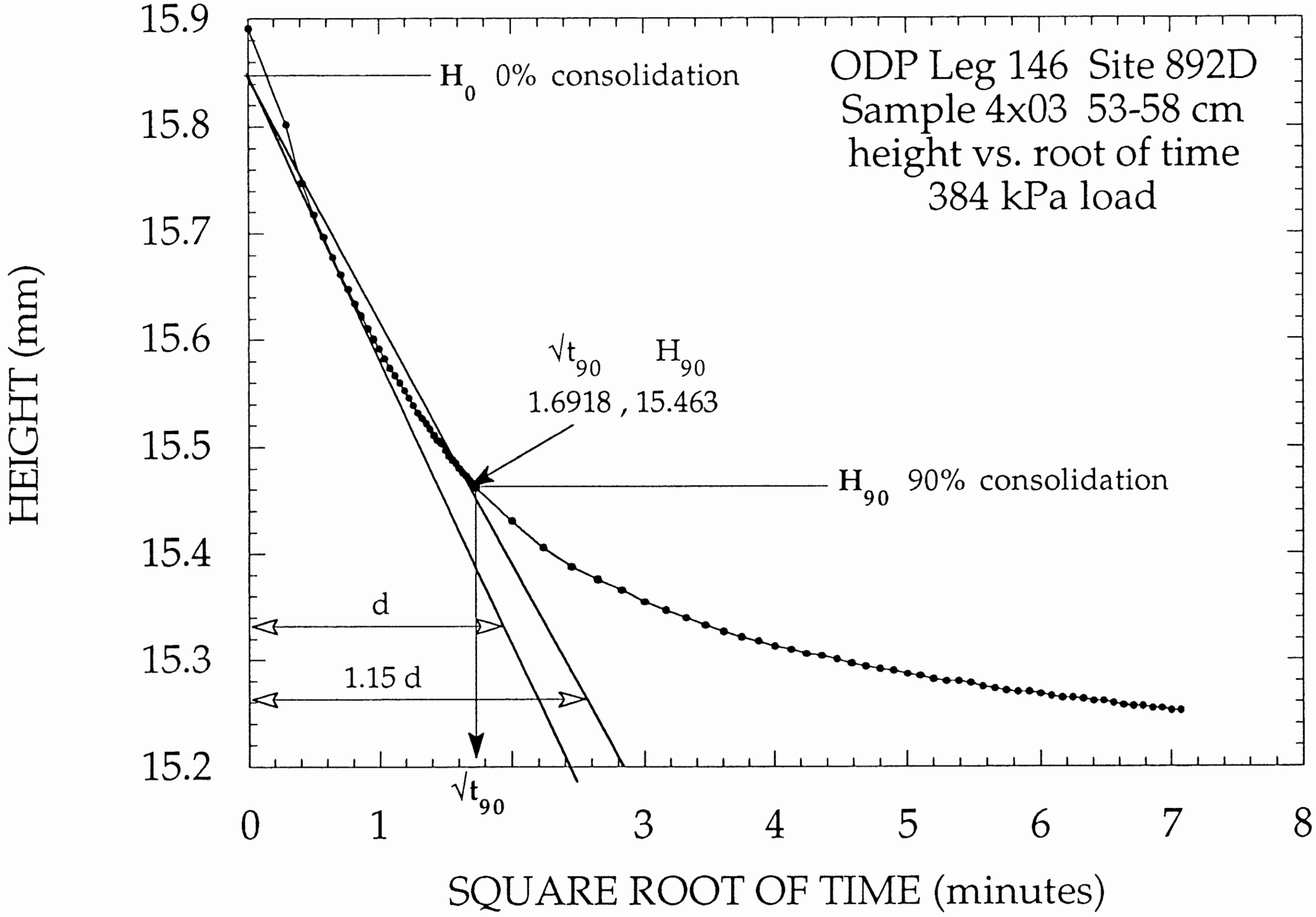

FIGURE A.1. Taylor's square root of time method. The procedure consists of drawing a straight line through the initial compression curve, extrapolated to the ordinate axis. A second line with abscissas 1.15 times larger is drawn from the y-intercept. This second line intersects the curve at the point of 90% primary consolidation. This represents $\sqrt{t_{90}}$ and H_{90}.

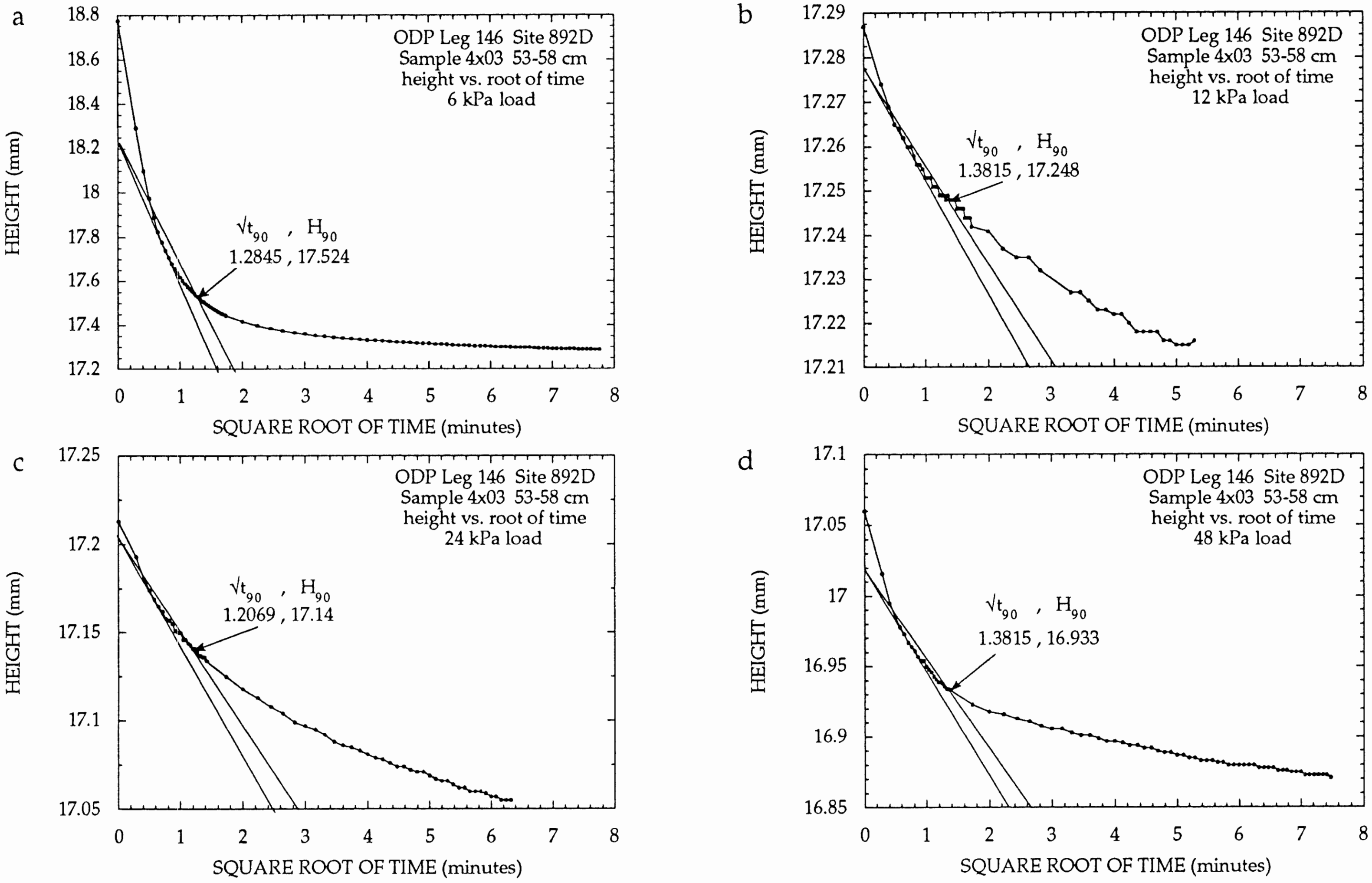

FIGURE A.2. Sample 4x03 consolidation test height data plotted against the square root of time. $\sqrt{t_{90}}$ and H_{90}, derived using Taylor's square root of time method, and sample height, are displayed for load increments a.) 6 kPa, b.) 12 kPa, c.) 24 kPa, and d.) 48 kPa.

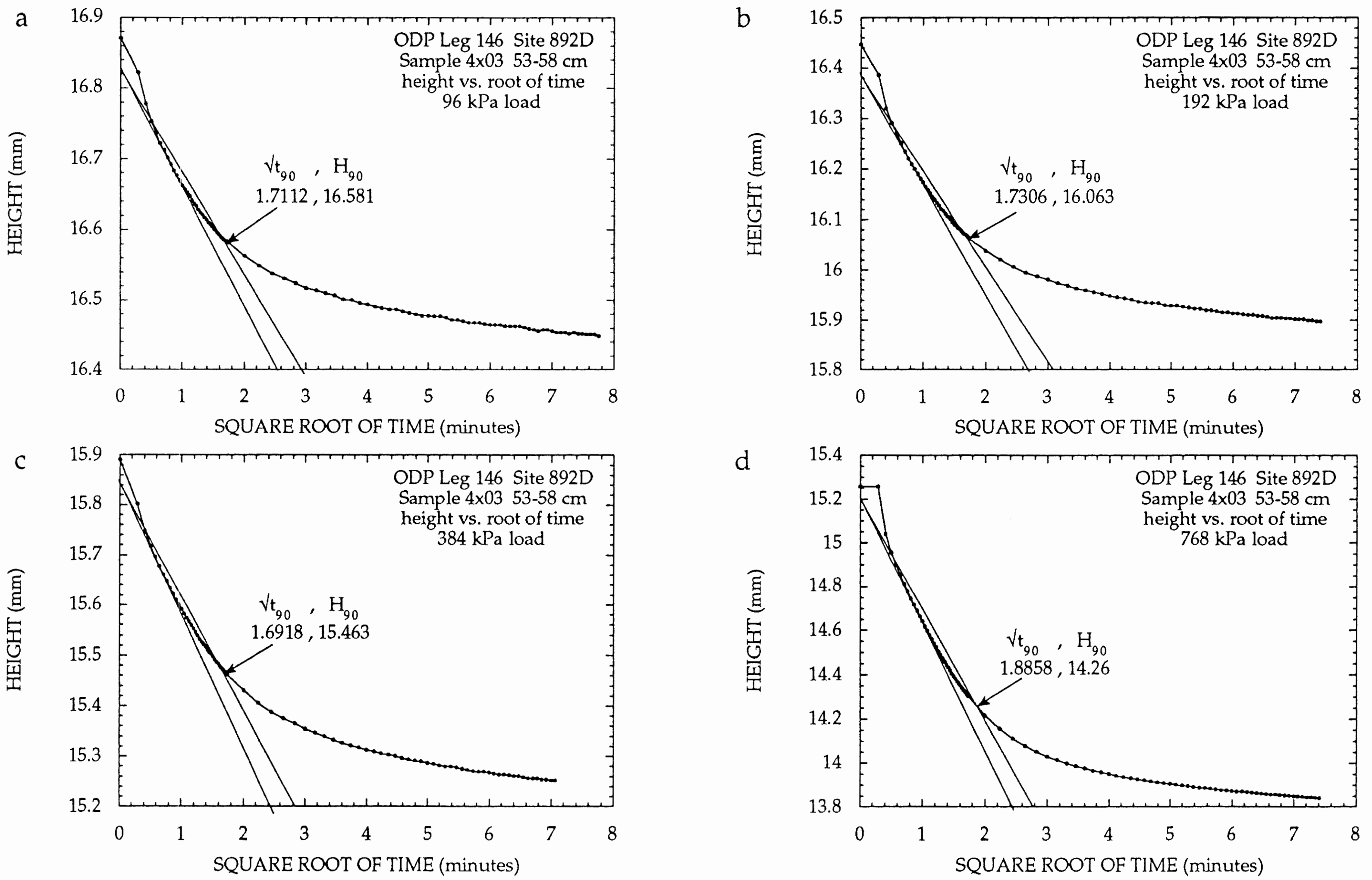

FIGURE A.3 Sample 4x03 consolidation test height data plotted against the square root of time. $\sqrt{t_{90}}$ and H_{90}, derived using Taylor's square root of time method, and sample height, are displayed for load increments a.) 96 kPa, b.) 192 kPa, c.) 384 kPa, and d.) 768 kPa.

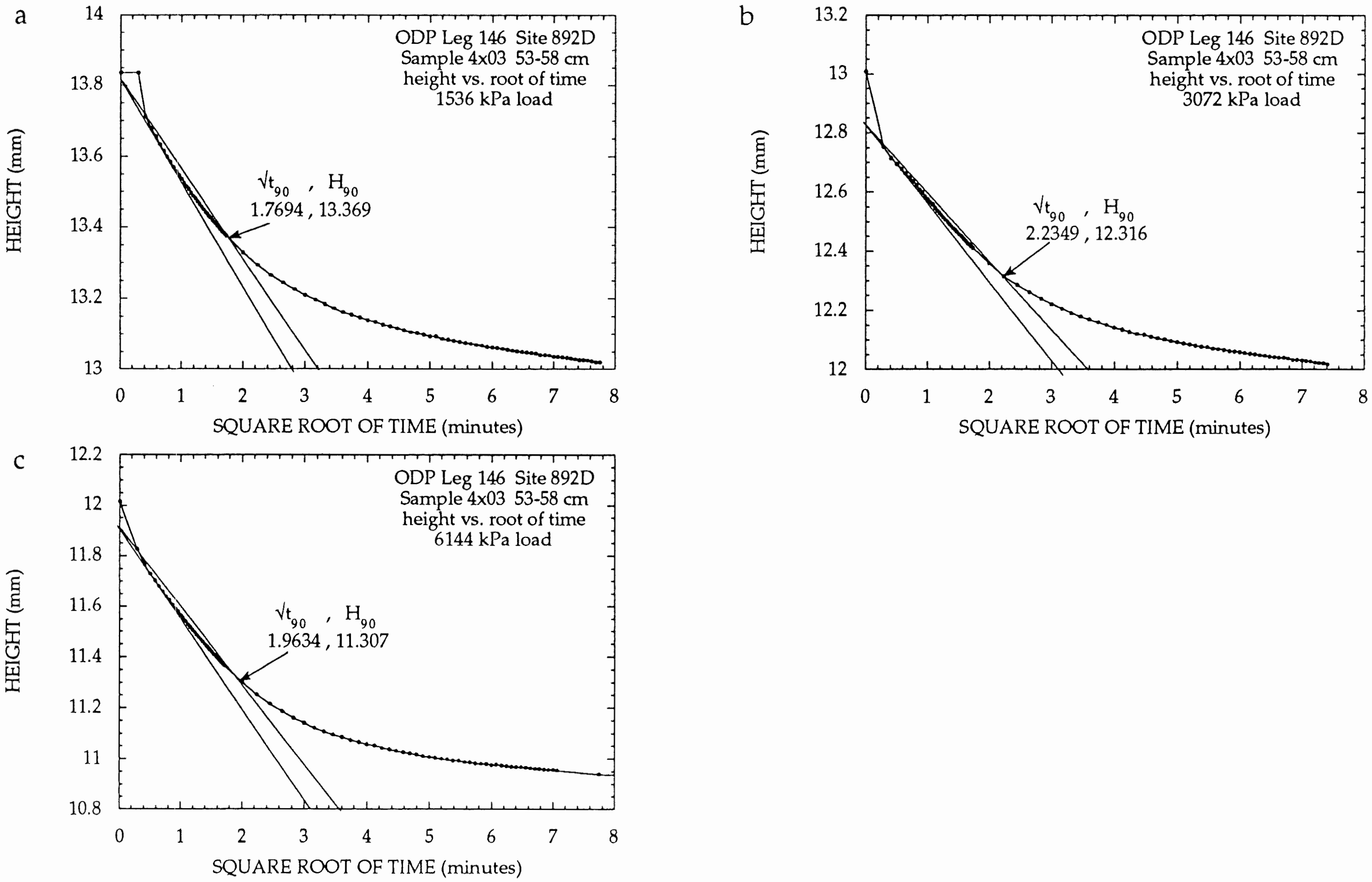

FIGURE A.4. Sample 4x03 consolidation test height data plotted against the square root of time. $\sqrt{t_{90}}$ and H_{90}, derived using Taylor's square root of time method, and sample height, are displayed for load increments a.) 1536 kPa, b.) 3072 kPa, and c.) 6144 kPa.

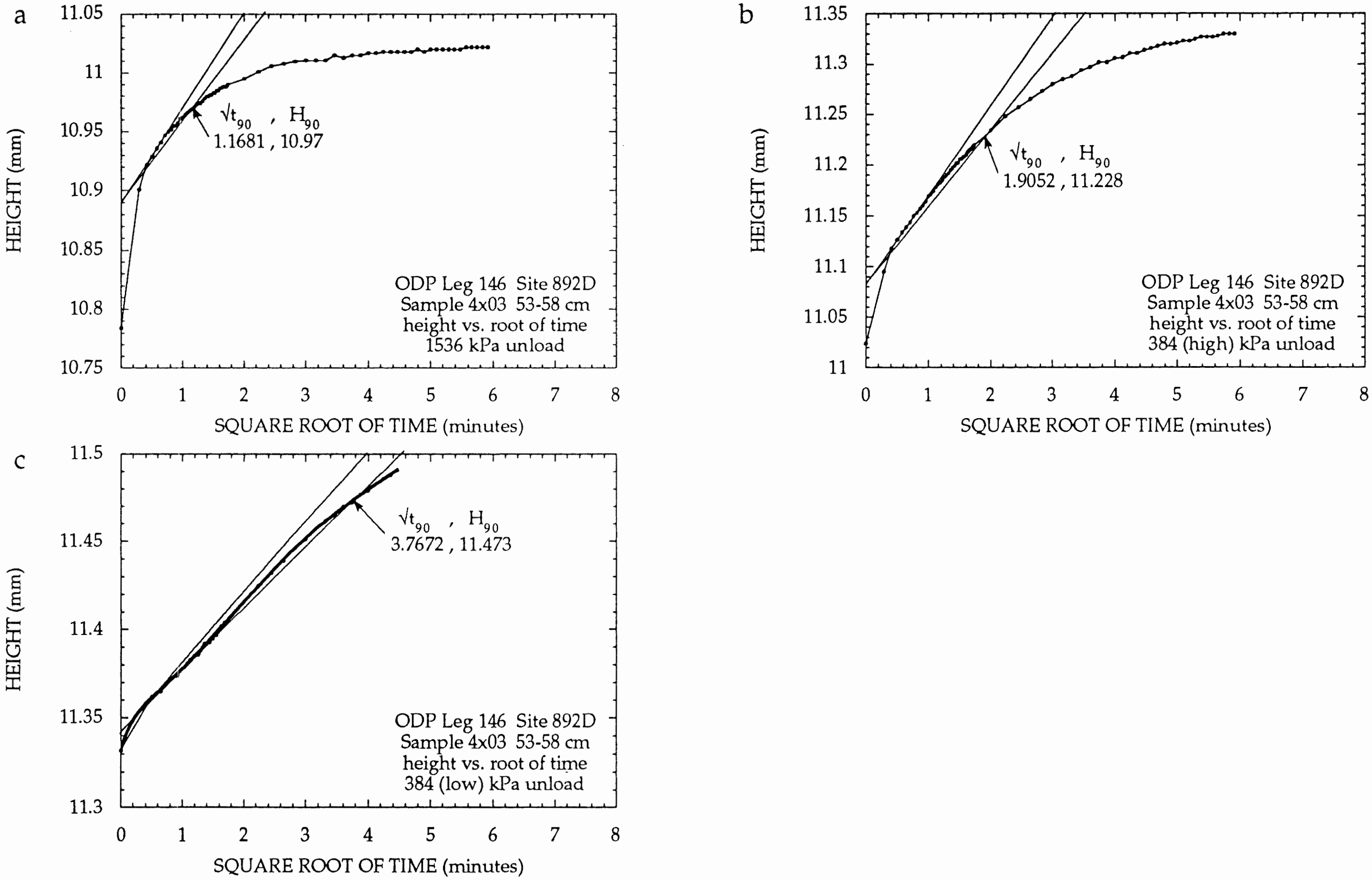

FIGURE A.5. Sample 4x03 consolidation test height data plotted against the square root of time. $\sqrt{t_{90}}$ and H_{90}, derived using Taylor's square root of time method, and sample height, are displayed for unload increments a.) 1536 kPa, b.) 384 (high) kPa, and c.) 384 (low) kPa.

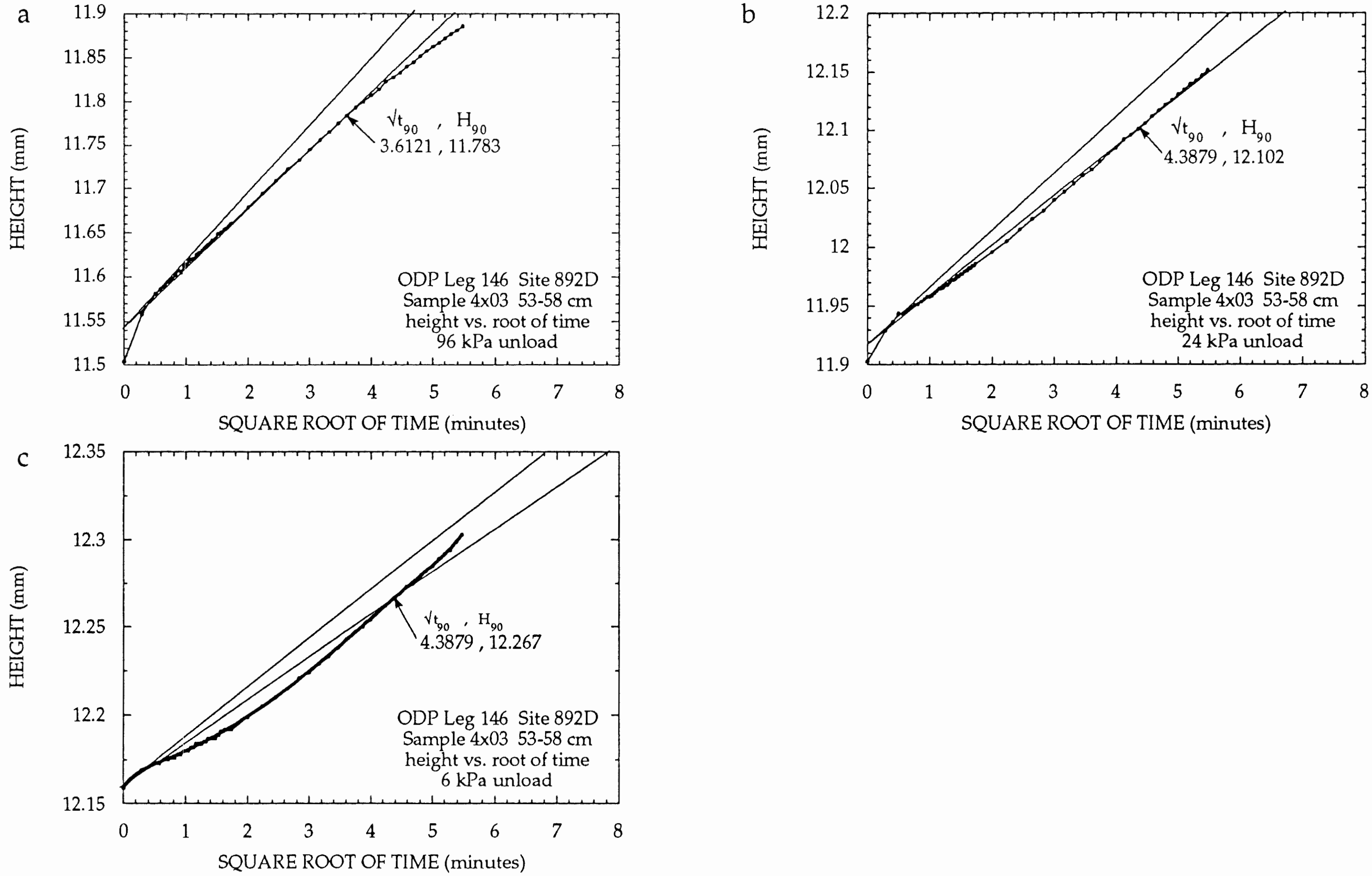

FIGURE A.6. Sample 4x03 consolidation test height data plotted against the square root of time. $\sqrt{t_{90}}$ and H_{90}, derived using Taylor's square root of time method, and sample height, are displayed for unload increments a.) 96 kPa, b.) 24 kPa, and c.) 6 kPa.

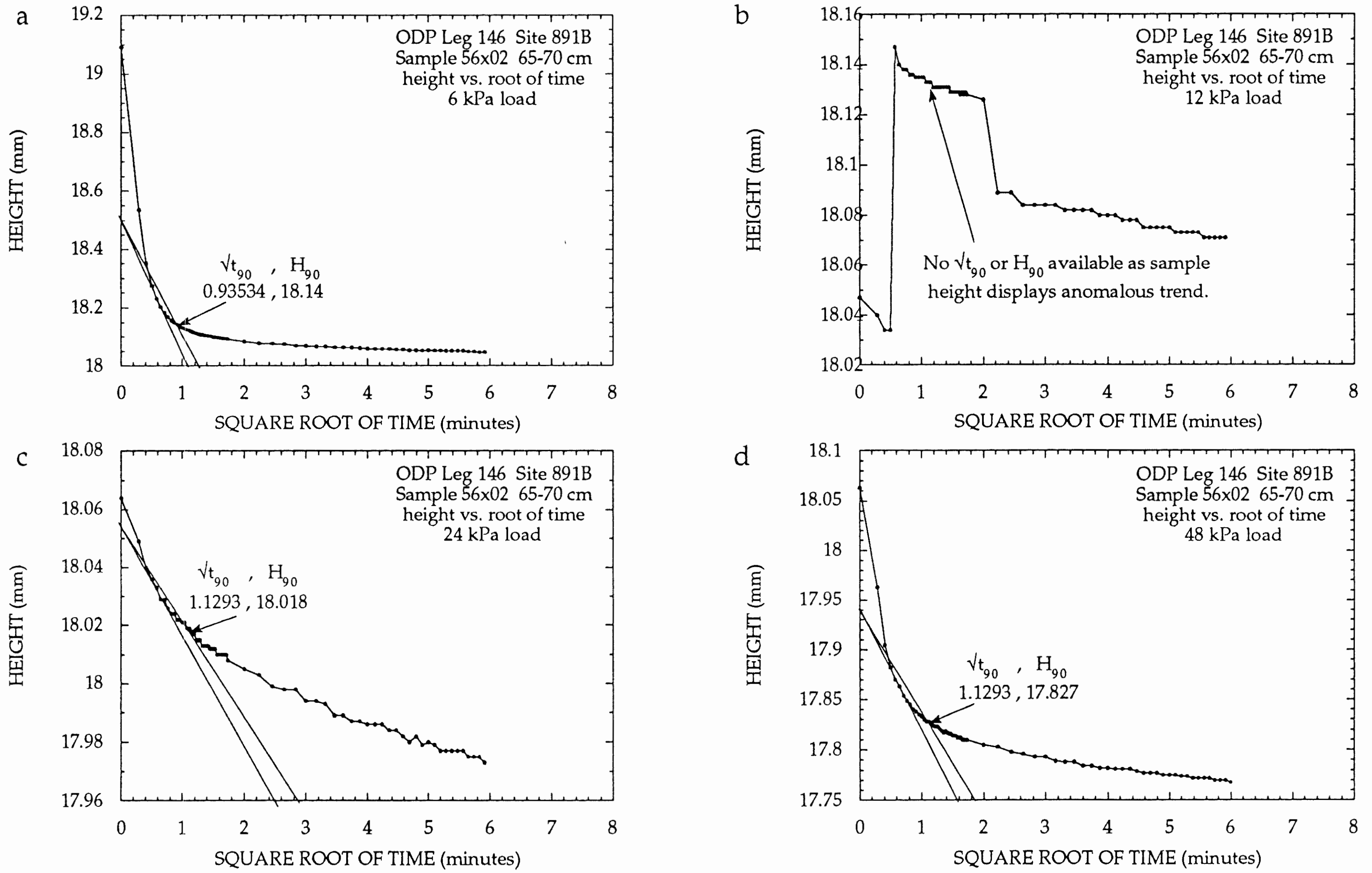

FIGURE A.7. Sample 56x02 consolidation test height data plotted against the square root of time. $\sqrt{t_{90}}$ and H_{90}, derived using Taylor's square root of time method, and sample height, are displayed for load increments a.) 6 kPa, b.) 12 kPa, c.) 24 kPa, and d.) 48 kPa.

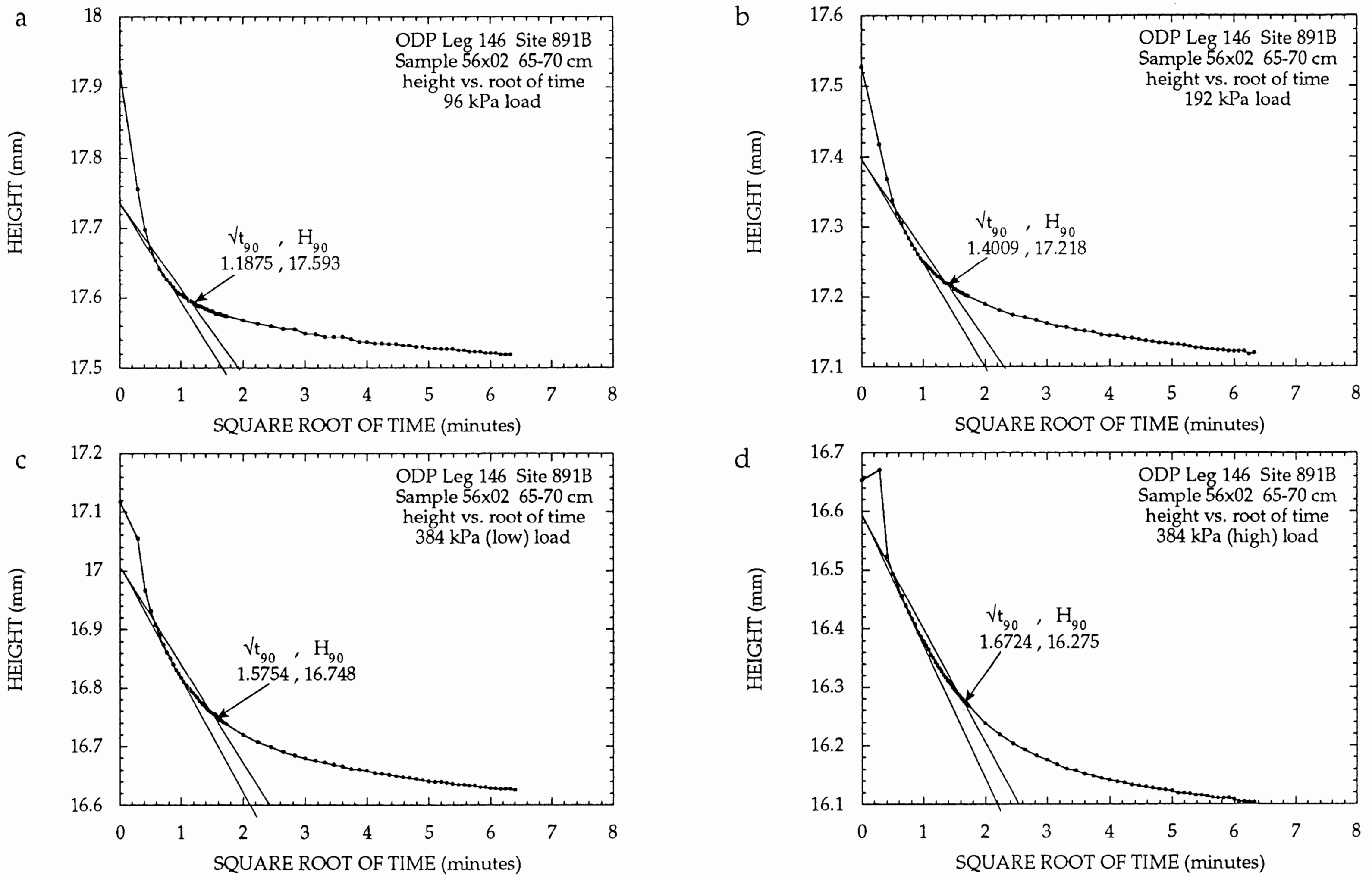

FIGURE A.8. Sample 56x02 consolidation test height data plotted against the square root of time. $\sqrt{t_{90}}$ and H_{90}, derived using Taylor's square root of time method, and sample height, are displayed for load increments a.) 96 kPa, b.) 192 kPa, c.) 384 (low) kPa, and d.) 384 (high) kPa.

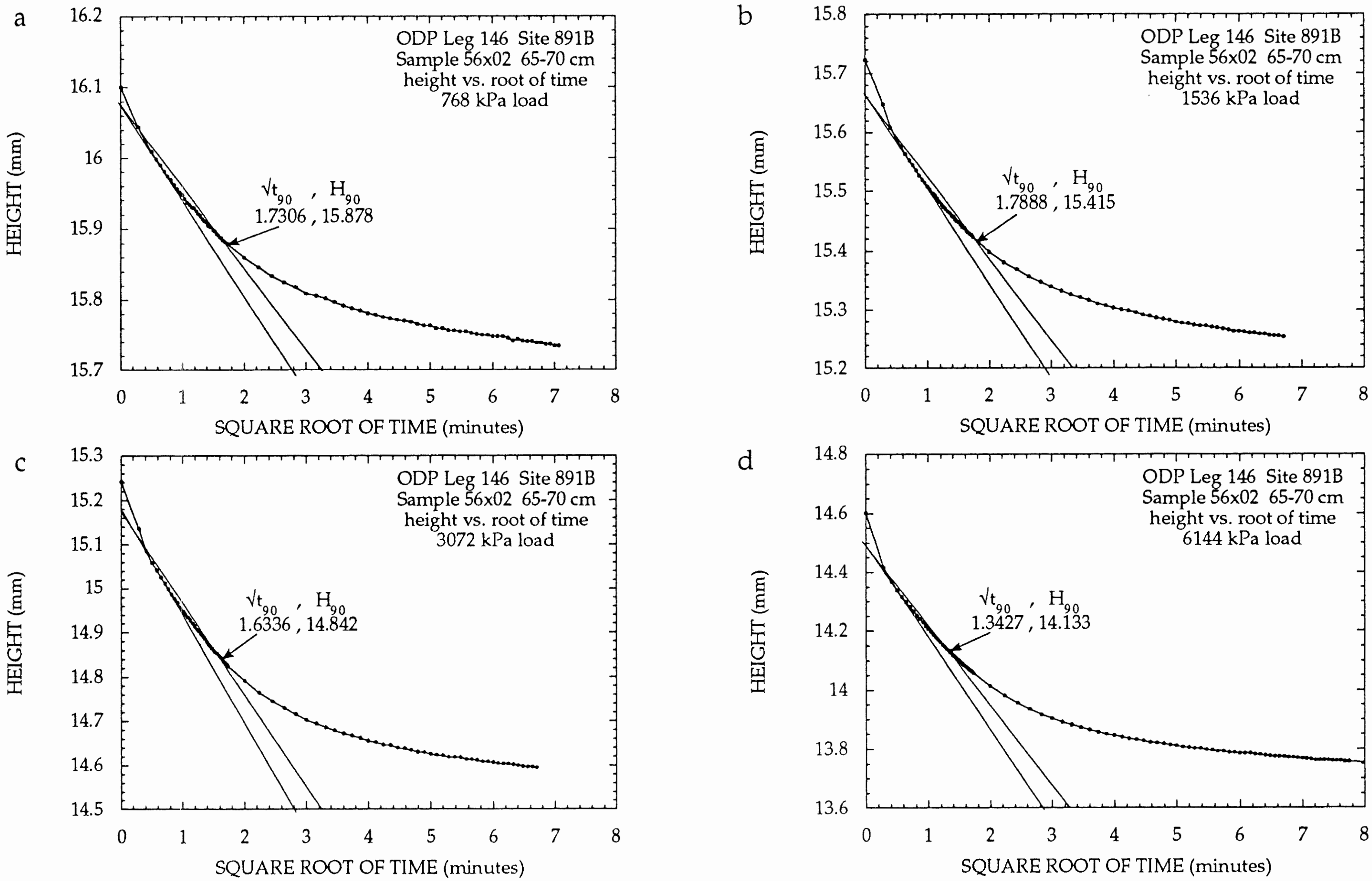

FIGURE A.9. Sample 56x02 consolidation test height data plotted against the square root of time. $\sqrt{t_{90}}$ and H_{90}, derived using Taylor's square root of time method, and sample height, are displayed for load increments a.) 768 kPa, b.) 1536 kPa, c.) 3072 kPa, and d.) 6144 kPa.

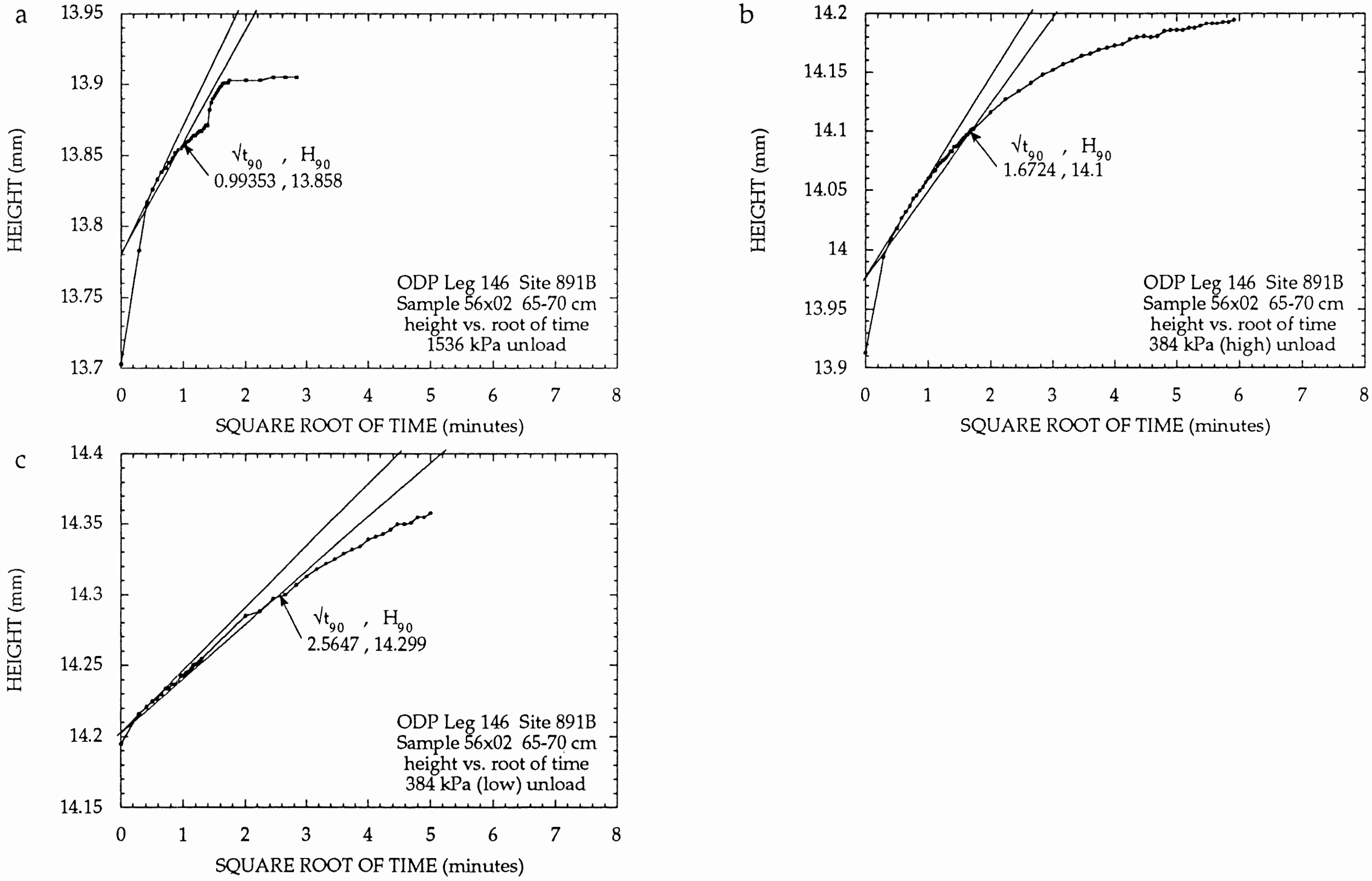

FIGURE A.10. Sample 56x02 consolidation test height data plotted against the square root of time. $\sqrt{t_{90}}$ and H_{90}, derived using Taylor's square root of time method, and sample height, are displayed for unload increments a.) 1536 kPa, b.) 384 (high) kPa, and c.) 384 (low) kPa.

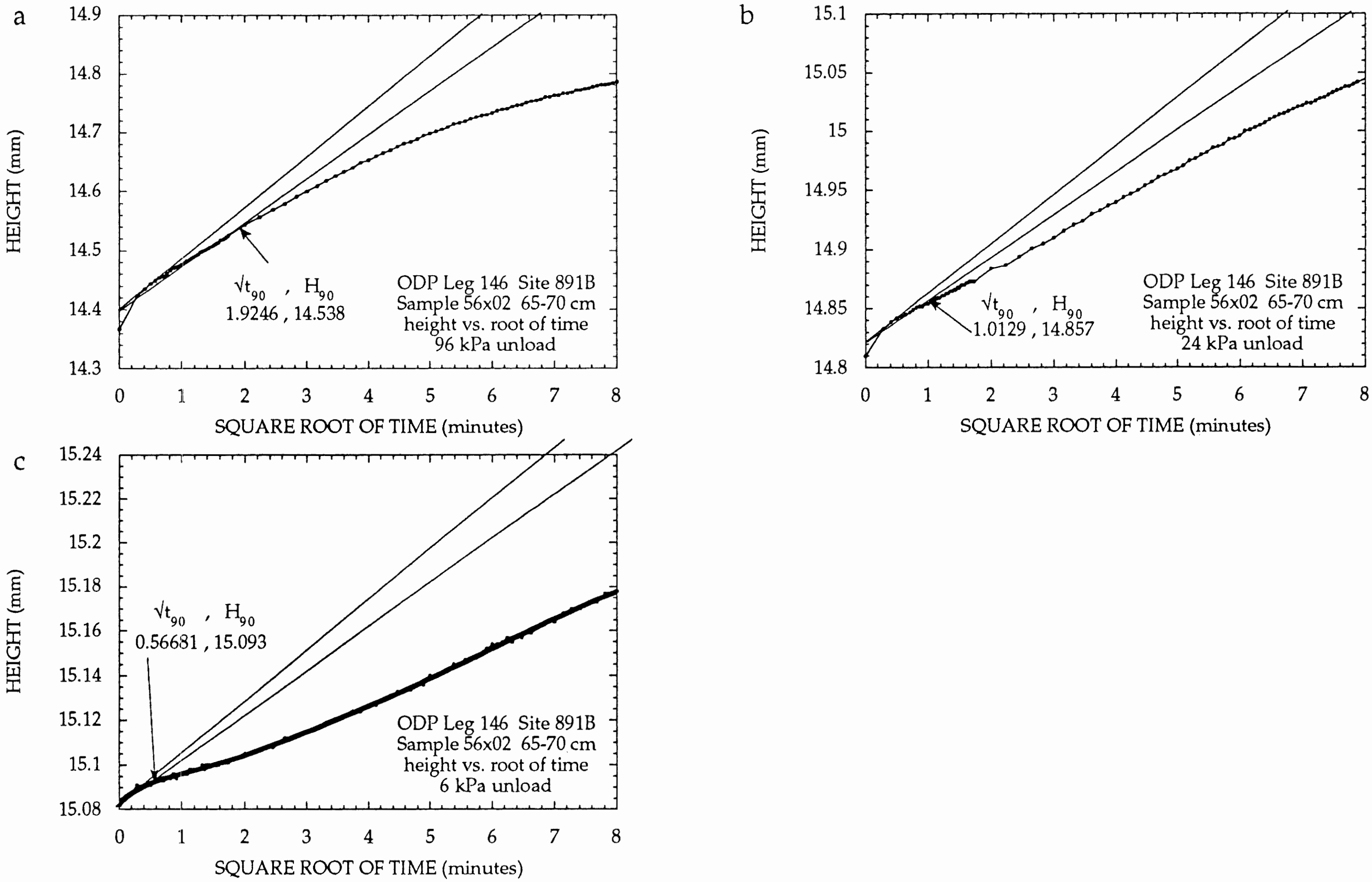

FIGURE A.11. Sample 56x02 consolidation test height data plotted against the square root of time. $\sqrt{t_{90}}$ and H_{90}, derived using Taylor's square root of time method, and sample height, are displayed for unload increments a.) 96 kPa, b.) 24 kPa, and c.) 6 kPa.

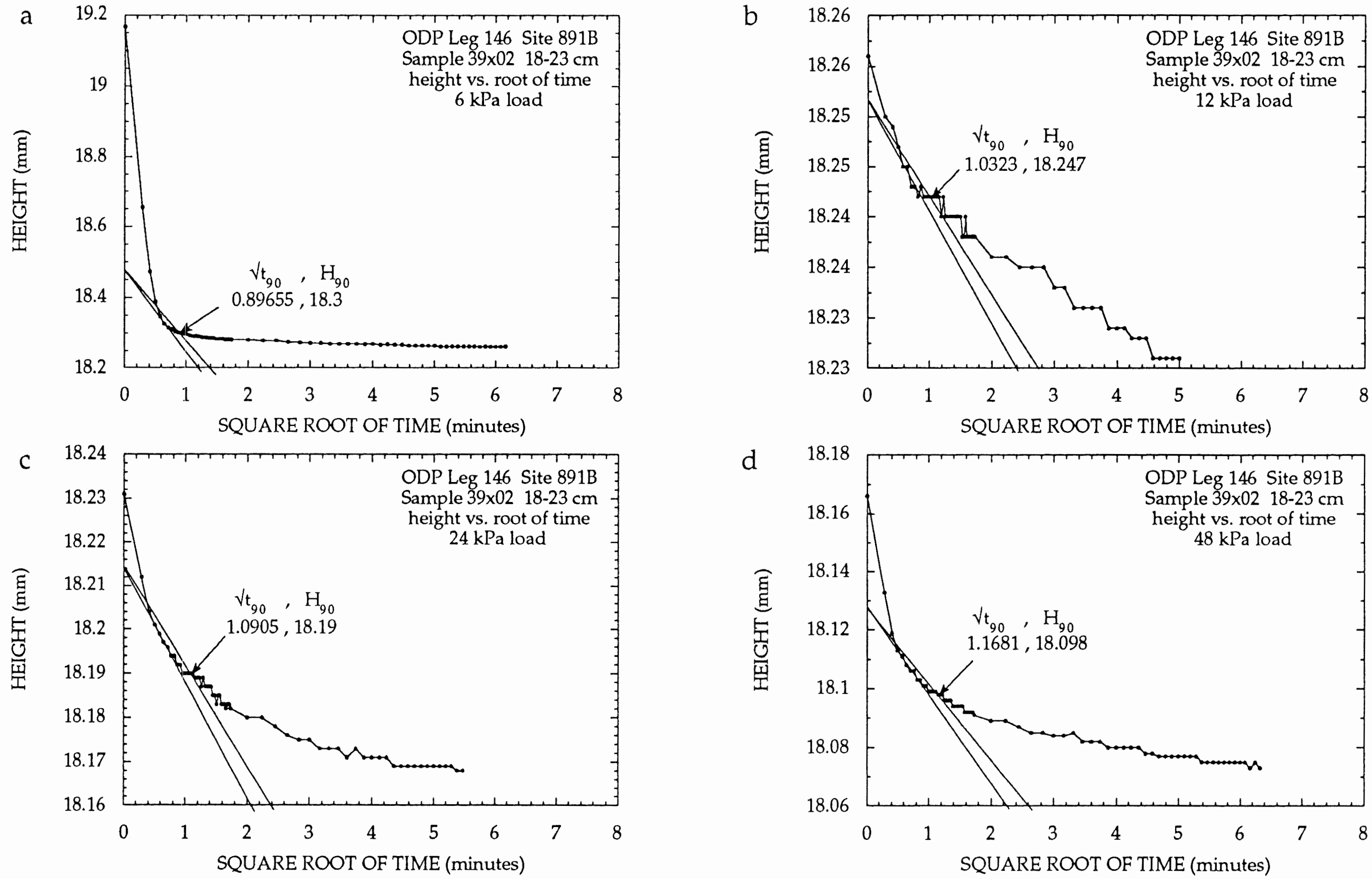

FIGURE A.12. Sample 39x02 consolidation test height data plotted against the square root of time. $\sqrt{t_{90}}$ and H_{90}, derived using Taylor's square root of time method, and sample height, are displayed for load increments a.) 6 kPa, b.) 12 kPa, c.) 24 kPa, and d.) 48 kPa.

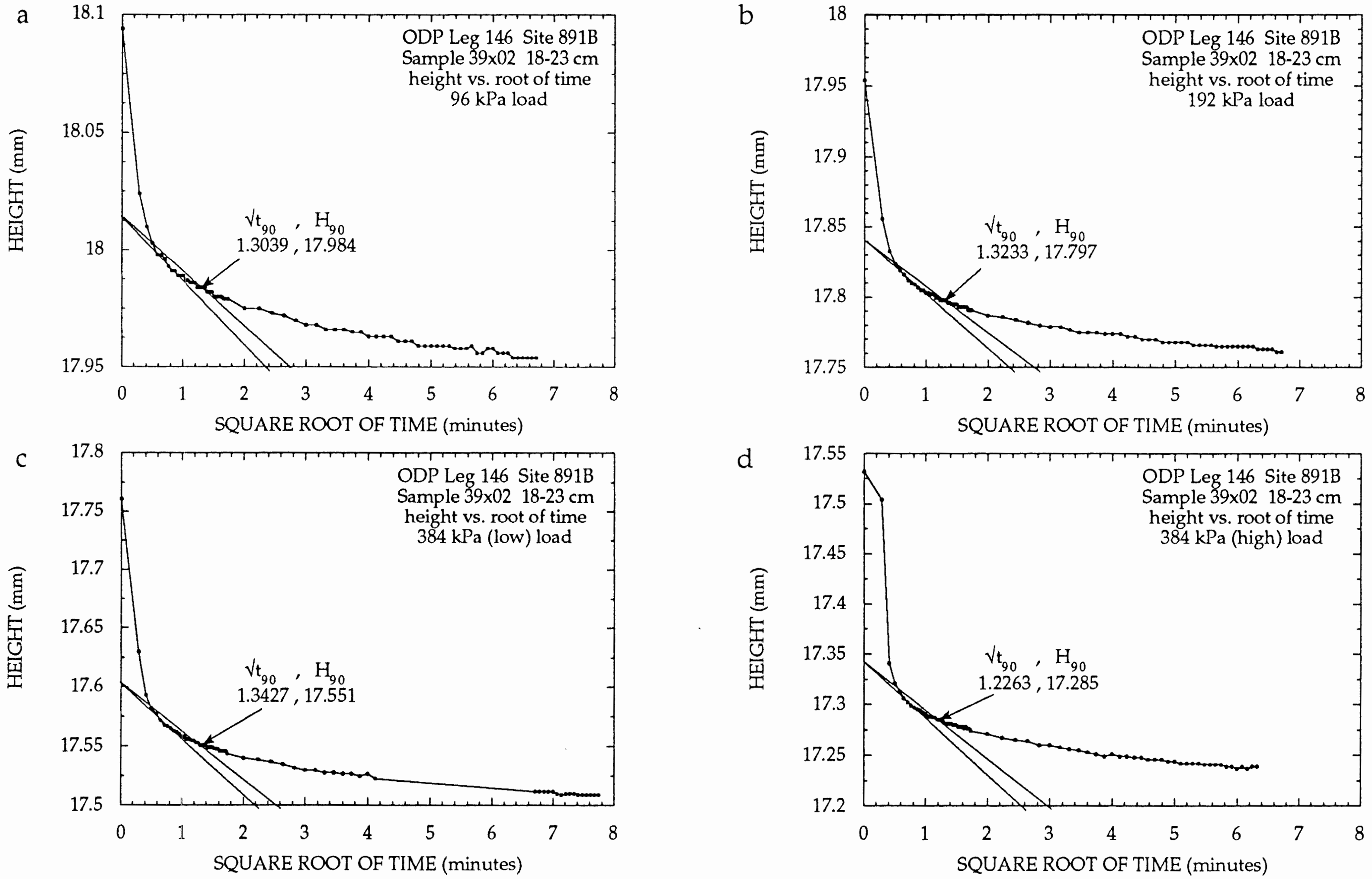

FIGURE A.13. Sample 39x02 consolidation test height data plotted against the square root of time. $\sqrt{t_{90}}$ and H_{90}, derived using Taylor's square root of time method, and sample height, are displayed for load increments a.) 96 kPa, b.) 192 kPa, c.) 384 (low) kPa, and d.) 384 (high) kPa.

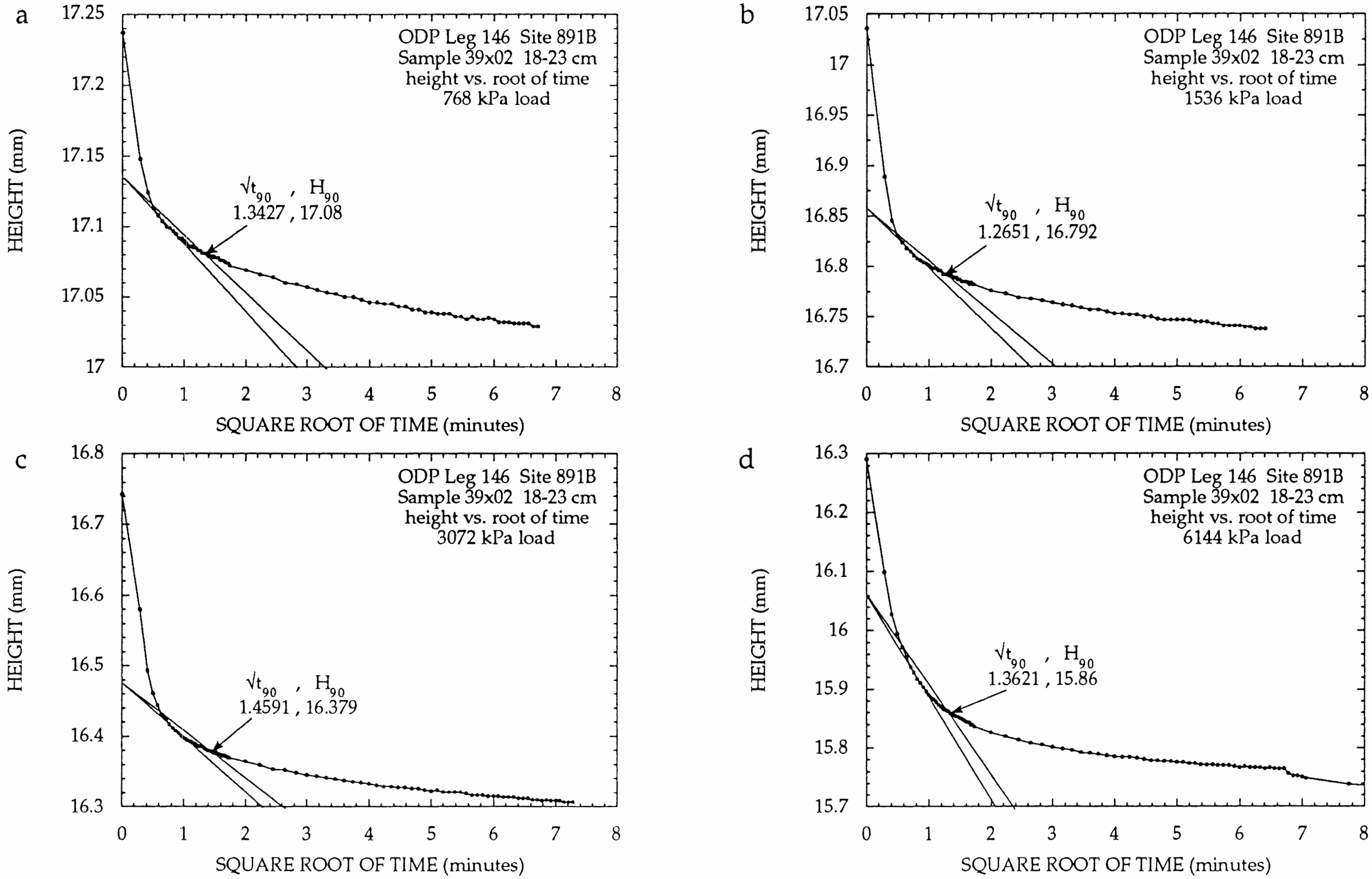

FIGURE A.14. Sample 39x02 consolidation test height data plotted against the square root of time. $\sqrt{t_{90}}$ and H_{90}, derived using Taylor's square root of time method, and sample height, are displayed for load increments a.) 768 kPa, b.) 1536 kPa, c.) 3072 kPa, and d.) 6144 kPa.

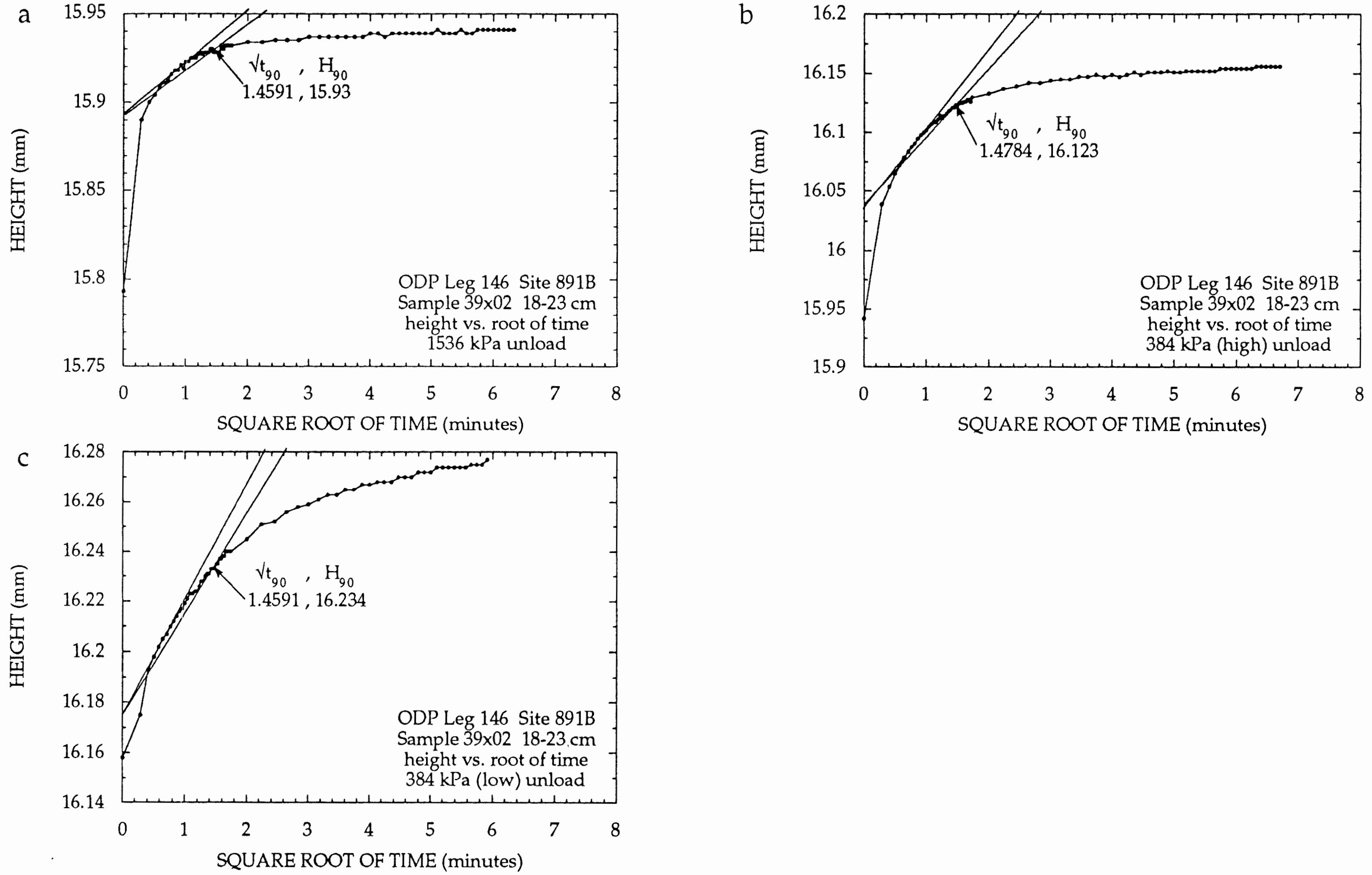

FIGURE A.15. Sample 39x02 consolidation test height data plotted against the square root of time. $\sqrt{t_{90}}$ and H_{90}, derived using Taylor's square root of time method, and sample height, are displayed for unload increments a.) 1536 kPa, b.) 384 (high) kPa, and c.) 384 (low) kPa.

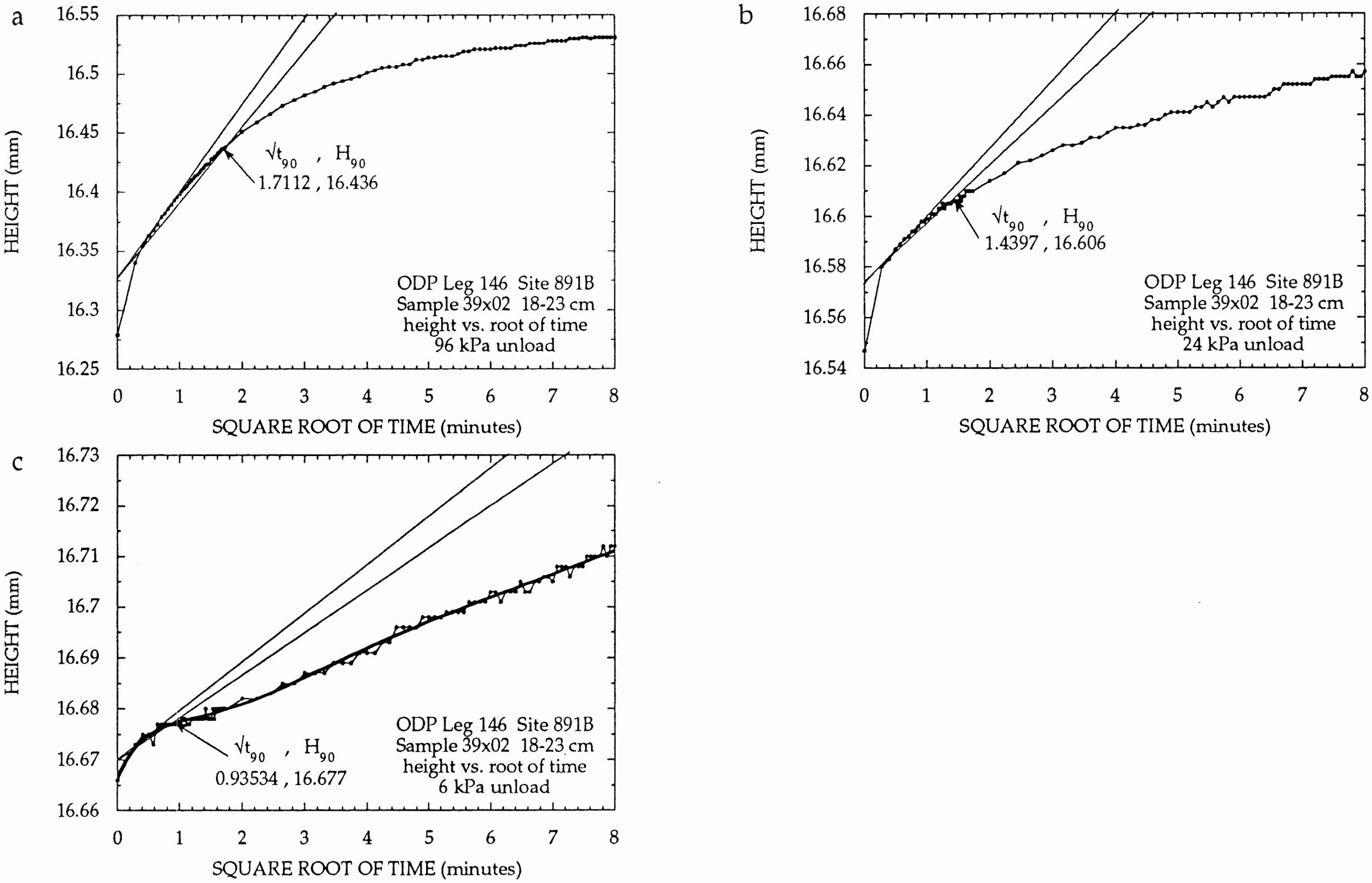

FIGURE A.16. Sample 39x02 consolidation test height data plotted against the square root of time. $\sqrt{t_{90}}$ and H_{90}, derived using Taylor's square root of time method, and sample height, are displayed for unload increments a.) 96 kPa, b.) 24 kPa, and c.) 6 kPa.

APPENDIX B: FLOW-PUMP PERMEABILITY TEST RESULTS

B.1. Pressure head vs. Flow rate plots

This appendix presents graphs of pressure head plotted against flow rate. The pressure head is the force per unit mass of water, and is usually expressed as the height of water that can be supported by a given pressure head. Pressure head is used in this study as it allows a convenient short cut to be employed when calculating permeability values. As pressure head is in cm of water, and flow rate is in ml or cm^3/hr, a conversion and possible source of error is avoided. Moreover, as this study uses fully saturated samples of constant height for permeability testing, pressure heads developed as water flows through samples represent total head loss.

When plotted against flow rate, pressure head forms a linear relationship, according to Darcy's Law. Least-squares linear regression fitting was employed to form best-fit lines, with excellent results. The slope of these best-fit lines represents the discharge over the hydraulic gradient as described in Equation 3.11. The calculation of hydraulic conductivity is thus simplified such it equals the value of M1 from each graph over sample height times the sample cross-sectional area.

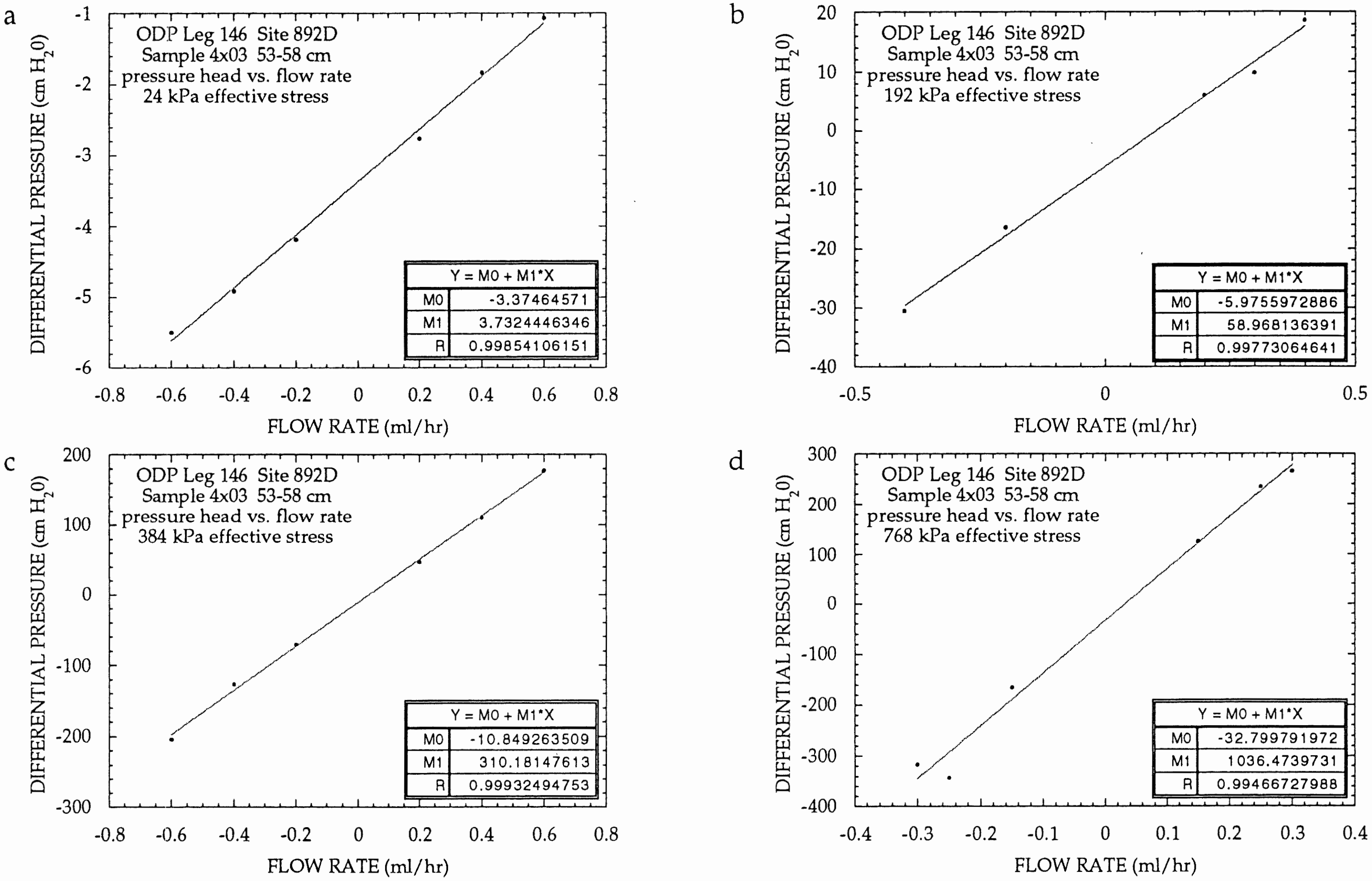

FIGURE B.1 Linear least-squares fitting applied to Sample 4x03 flow-pump permeability test data. Pressure head plotted against flow rate represents the hydraulic gradient of the sample, at an effective stress of a.) 24 kPa, b.) 192 kPa, c.) 384 kPa, and d.) 768 kPa.

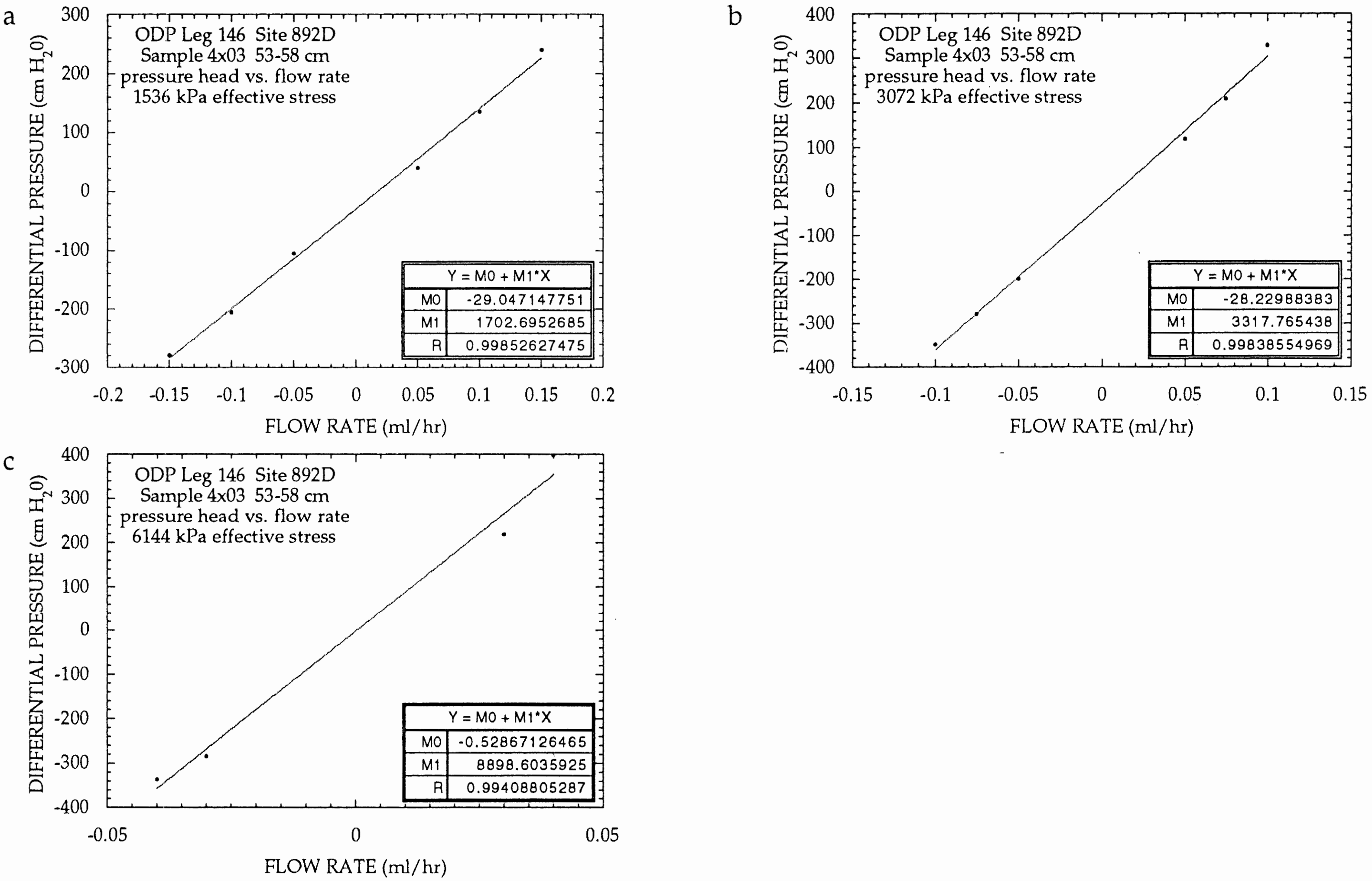

FIGURE B.2 Linear least-squares fitting applied to Sample 4x03 flow-pump permeability test data. Pressure head plotted against flow rate represents the hydraulic gradient of the sample, at an effective stress of a.)1536 kPa, b.) 3072 kPa, and c.) 6144 kPa.

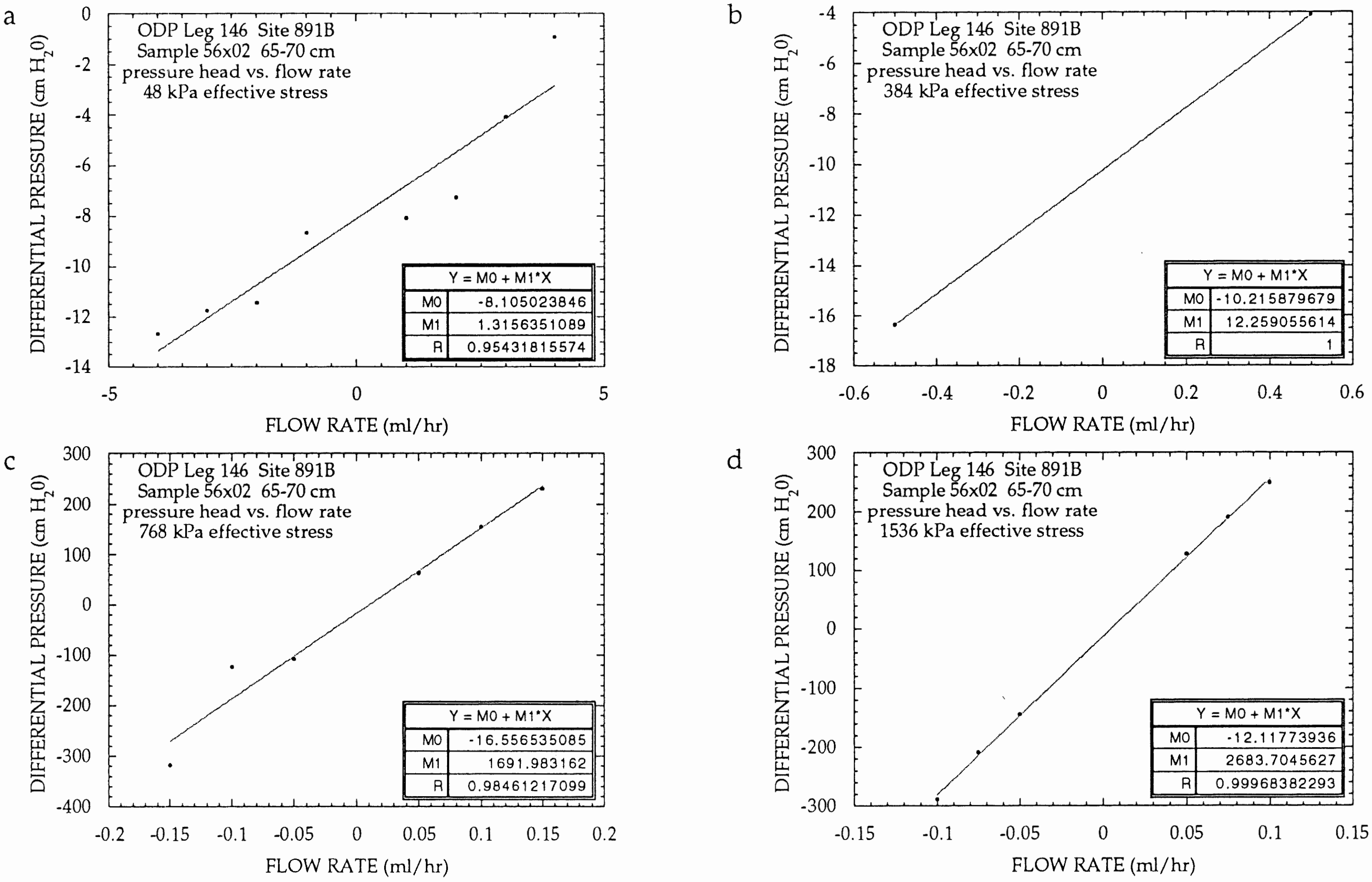

FIGURE B.3 Linear least-squares fitting applied to Sample 56x02 flow-pump permeability test data. Pressure head plotted against flow rate represents the hydraulic gradient of the sample, at an effective stress of a.) 48 kPa, b.) 384 kPa, c.) 768 kPa, and d.) 1536 kPa.

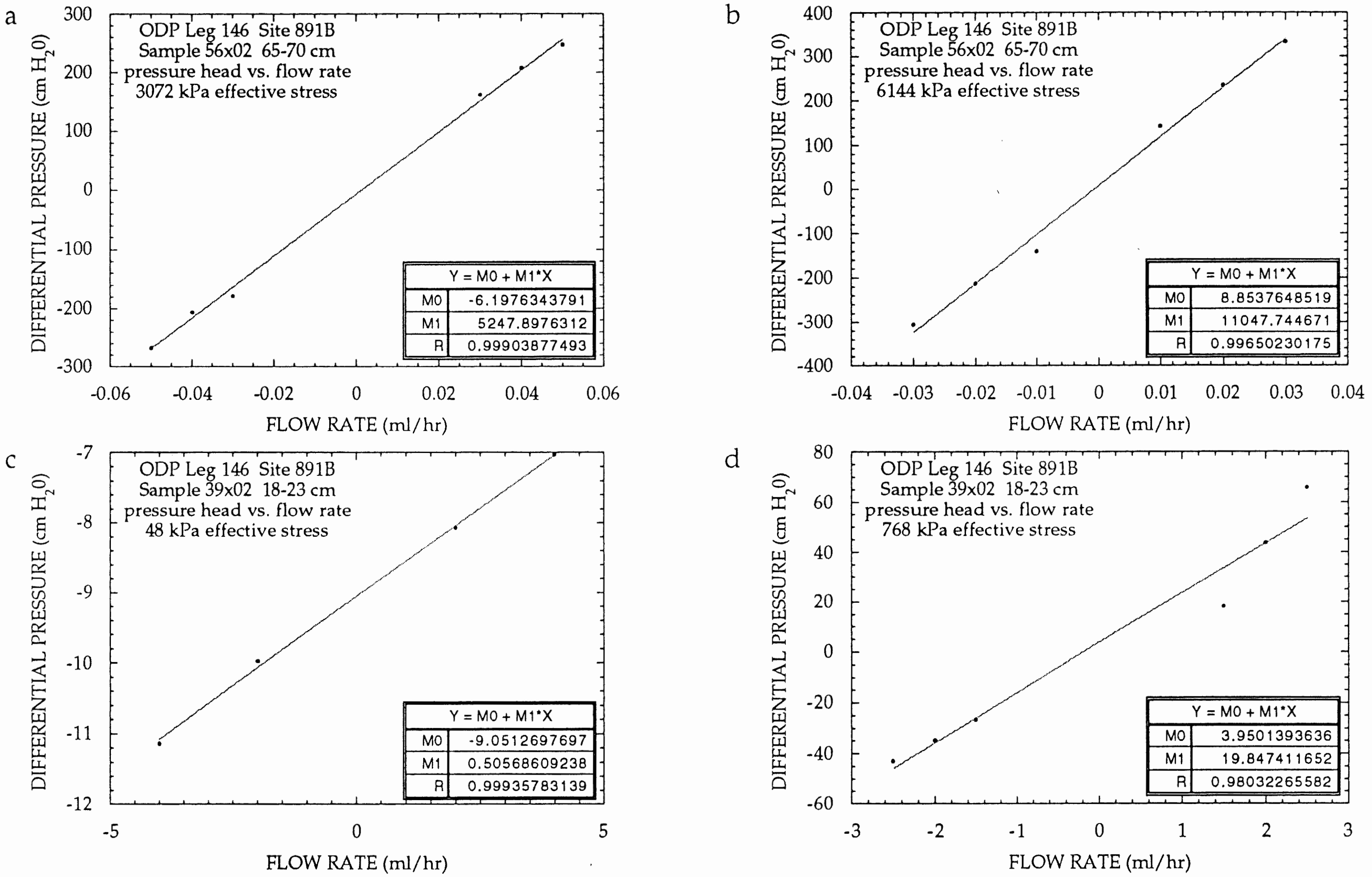

FIGURE B.4 Linear least-squares fitting applied to Sample 56x02 and 39x02 flow-pump permeability test data. Pressure head plotted against flow rate represents the hydraulic gradient of the sample, at an effective stress of, for Sample 56x02, a.) 3072 kPa, and b.) 6144 kPa, and for Sample 39x02, c.) 48 kPa, and d.) 768 kPa.

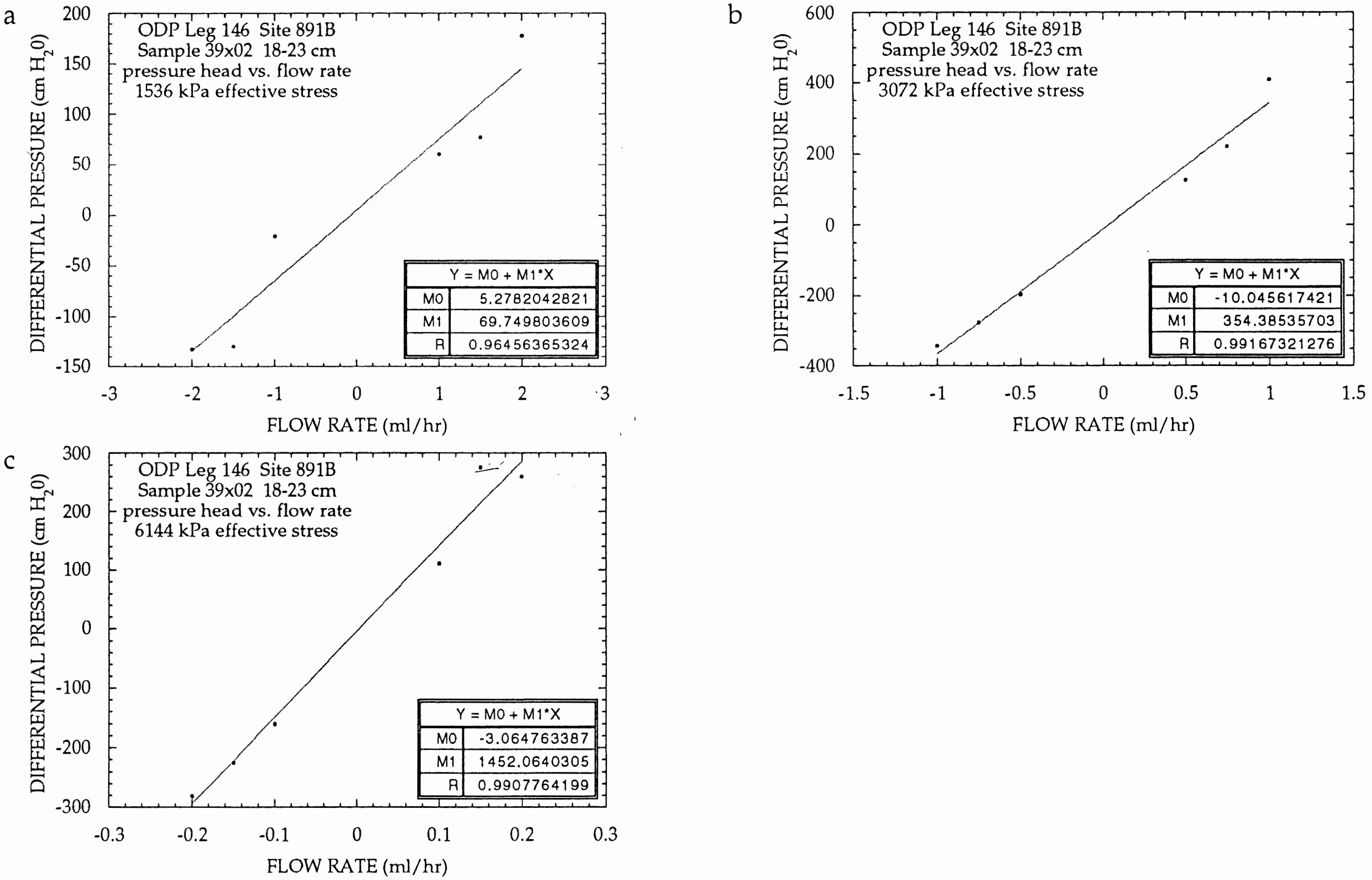

FIGURE B.5 Linear least-squares fitting applied to Sample 39x02 flow-pump permeability test data. Pressure head plotted against flow rate represents the hydraulic gradient of the sample, at an effective stress of a.) 1536 kPa, b.) 3072 kPa, and c.) 6144 kPa.

Time	Sample 4X-03 Load Cycle							
(minutes)	6 kPa	12 kPa	24 kPa	48 kPa	96 kPa	192 kPa	384 kPa	768 kPa
0	18.776	17.287	17.213	17.06	16.871	16.447	15.891	15.259
0.083	18.292	17.274	17.193	17.016	16.822	16.386	15.802	15.259
0.16666	18.099	17.269	17.181	16.995	16.778	16.321	15.748	15.042
0.25	17.975	17.265	17.174	16.985	16.753	16.291	15.718	14.957
0.3333	17.889	17.264	17.169	16.978	16.736	16.27	15.697	14.901
0.4166	17.826	17.262	17.165	16.973	16.722	16.251	15.678	14.854
0.5	17.777	17.26	17.162	16.967	16.712	16.235	15.662	14.812
0.58333	17.74	17.26	17.158	16.964	16.701	16.221	15.648	14.779
0.666	17.707	17.258	17.157	16.961	16.692	16.21	15.634	14.747
0.75	17.68	17.256	17.155	16.957	16.683	16.2	15.623	14.717
0.833	17.658	17.256	17.151	16.954	16.676	16.191	15.611	14.691
0.9166	17.637	17.255	17.15	16.954	16.669	16.181	15.601	14.665
1	17.619	17.253	17.15	16.95	16.662	16.174	15.592	14.642
1.083	17.603	17.253	17.146	16.948	16.657	16.165	15.583	14.619
1.1666	17.589	17.253	17.146	16.946	16.652	16.158	15.574	14.598
1.25	17.575	17.251	17.144	16.943	16.647	16.152	15.567	14.579
1.3333	17.565	17.251	17.143	16.941	16.641	16.144	15.56	14.56
1.4166	17.553	17.251	17.141	16.939	16.636	16.139	15.553	14.542
1.5	17.544	17.249	17.141	16.939	16.633	16.133	15.546	14.525
1.5833	17.533	17.249	17.139	16.938	16.628	16.128	15.539	14.507
1.666	17.525	17.249	17.137	16.936	16.624	16.121	15.532	14.49
1.75	17.517	17.248	17.137	16.934	16.621	16.118	15.527	14.476
1.833	17.51	17.249	17.136	16.934	16.617	16.112	15.522	14.461
1.9166	17.504	17.248	17.136		16.614	16.107	15.517	14.446
2	17.498	17.248	17.134		16.61	16.104	15.511	14.434
2.083	17.493	17.248			16.608	16.1	15.506	14.42
2.1666	17.486	17.248			16.605	16.095	15.503	14.407
2.25	17.481	17.246			16.601	16.091	15.497	14.395
2.333	17.476	17.246			16.599	16.089	15.492	14.384
2.4166	17.47	17.246			16.596	16.084	15.488	14.372
2.5	17.467	17.246			16.594	16.082	15.485	14.362
2.5833	17.463	17.246			16.591	16.079	15.48	14.351
2.666	17.458	17.244			16.589	16.075	15.476	14.341
2.75	17.455	17.244			16.587	16.072	15.473	14.332
2.833	17.451	17.244			16.585	16.07	15.469	14.322
2.9166	17.448	17.244			16.584	16.067	15.466	14.313
3	17.444	17.242	17.125	16.923	16.582	16.063	15.462	14.304
4	17.416	17.241	17.118	16.918	16.563	16.039	15.431	14.218

Time (minutes)	Sample 4X-03 Load Cycle							
	6 kPa	12 kPa	24 kPa	48 kPa	96 kPa	192 kPa	384 kPa	768 kPa
5	17.397	17.237	17.113	16.916	16.549	16.021	15.406	14.157
6	17.385	17.235	17.108	16.913	16.538	16.007	15.388	14.113
7	17.374	17.235	17.104	16.911	16.531	15.995	15.376	14.08
8	17.365	17.232	17.099	16.908	16.524	15.988	15.366	14.053
9	17.36		17.097	16.906	16.517	15.981	15.355	14.03
10	17.353		17.095	16.906	16.514	15.974	15.347	14.015
11	17.349	17.227	17.092	16.903	16.51	15.969	15.34	13.999
12	17.344	17.227	17.088	16.901	16.507	15.963	15.333	13.987
13	17.34	17.225	17.086	16.901	16.501	15.96	15.327	13.976
14	17.337	17.223	17.085	16.899	16.5	15.956	15.322	13.966
15	17.335	17.223	17.083	16.897	16.496	15.953	15.318	13.959
16	17.332	17.222	17.081	16.897	16.494	15.949	15.313	13.952
17	17.33	17.222	17.079	16.896	16.491	15.946	15.31	13.943
18	17.328	17.22	17.078	16.894	16.489	15.944	15.306	13.938
19	17.325	17.218	17.076	16.894	16.487	15.941	15.304	13.932
20	17.323	17.218	17.074	16.892	16.487	15.937	15.301	13.927
21	17.321	17.218	17.074	16.892	16.484	15.935	15.297	13.922
22	17.32	17.218	17.072	16.89	16.482	15.934	15.294	13.918
23	17.318	17.216	17.071	16.889	16.48	15.934	15.292	13.913
24	17.316	17.216	17.071	16.889	16.478	15.93	15.29	13.91
25	17.316	17.215	17.069	16.887	16.478	15.929	15.287	13.906
26	17.313	17.215	17.067	16.887	16.477	15.929	15.285	13.903
27	17.313	17.215	17.066	16.885	16.477	15.927	15.282	13.899
28	17.311	17.216	17.066	16.885	16.475	15.925	15.28	13.896
29	17.309		17.064	16.883	16.472	15.923	15.28	13.892
30	17.307		17.062	16.883	16.472	15.923	15.278	13.889
31	17.307		17.062	16.883	16.47	15.92	15.275	13.887
32	17.306		17.06	16.882	16.468	15.92	15.273	13.885
33	17.304		17.06	16.882	16.468	15.918	15.271	13.881
34	17.304		17.06	16.88	16.468	15.916	15.27	13.878
35	17.304		17.059	16.88	16.466	15.916	15.27	13.876
36	17.302		17.057	16.88	16.465	15.914	15.268	13.874
37	17.3		17.057	16.88	16.465	15.914	15.266	13.871
38	17.3		17.055	16.88	16.465	15.912	15.264	13.871
39	17.3		17.055	16.88	16.463	15.911	15.264	13.869
40	17.299		17.055	16.878	16.463	15.911	15.263	13.866
41	17.297			16.878	16.463	15.909	15.261	13.864
42	17.297			16.878	16.463	15.909	15.261	13.862

Time (minutes)	Sample 4X-03 Load Cycle							
	6 kPa	12 kPa	24 kPa	48 kPa	96 kPa	192 kPa	384 kPa	768 kPa
43	17.297			16.878	16.461	15.907	15.259	13.86
44	17.297			16.876	16.459	15.905	15.257	13.857
45	17.295			16.876	16.458	15.905	15.256	13.857
46	17.294			16.876	16.456	15.905	15.256	13.855
47	17.294			16.875	16.458	15.904	15.254	13.854
48	17.294			16.875	16.458	15.904	15.254	13.852
49	17.292			16.875	16.456	15.902	15.252	13.85
50	17.292			16.873	16.454	15.902	15.252	13.848
51	17.292			16.873	16.454	15.902		13.847
52	17.29			16.873	16.454	15.9		13.845
53	17.292			16.873	16.452	15.9		13.845
54	17.292			16.873	16.454	15.898		13.843
55	17.288			16.873	16.452	15.898		13.841
56	17.288			16.871	16.452			
57	17.288				16.451			
58	17.288				16.451			
59	17.287				16.451			
60	17.287				16.449			

	Sample 4X-03 Load Cycle			Sample 4X-03 Unload Cycle					
Time (minutes)	1536 kPa	3072 kPa	6144 kPa	1536 kPa	384 kPa (high)	384 kPa (low)	96 kPa	24 kPa	6 kPa
0	13.836	13.009	12.015	10.784	11.024	11.332	11.504	11.903	12.159
0.083	13.836	12.753	11.828	10.901	11.095		11.558	11.929	12.169
0.16666	13.712	12.715	11.768	10.922	11.118		11.572	11.937	12.171
0.25	13.678	12.695	11.73	10.929	11.127	11.362	11.581	11.944	12.173
0.3333	13.654	12.679	11.704	10.936	11.134	11.364	11.586	11.944	12.173
0.4166	13.633	12.664	11.681	10.941	11.139	11.365	11.589	11.947	12.175
0.5	13.615	12.65	11.66	10.947	11.144		11.595	11.949	12.175
0.58333	13.598	12.636	11.64	10.95	11.15		11.598	11.951	12.176
0.666	13.584	12.623	11.625	10.952	11.153	11.372	11.602	11.952	12.176
0.75	13.57	12.609	11.607	10.955	11.157		11.607	11.954	12.178
0.833	13.557	12.599	11.591	10.957	11.16	11.374	11.605	11.956	12.178
0.9166	13.547	12.587	11.579	10.961	11.164		11.612	11.958	12.18
1	13.536	12.576	11.565	10.962	11.169		11.614	11.958	12.18
1.083	13.524	12.567	11.553	10.964	11.171		11.618	11.959	12.18
1.1666	13.515	12.559	11.541	10.966	11.174	11.381	11.62	11.961	12.182
1.25	13.507	12.548	11.528	10.968	11.178	11.383	11.621	11.963	12.182
1.3333	13.496	12.539	11.518	10.969	11.181		11.625	11.965	12.184
1.4166	13.487	12.531	11.507	10.971	11.183	11.385	11.627	11.965	12.184
1.5	13.48	12.523	11.497	10.973	11.185	11.386	11.628	11.966	12.184
1.5833	13.472	12.515	11.486	10.974	11.188	11.386	11.63	11.968	12.184
1.666	13.465	12.508	11.477	10.974	11.19	11.388	11.633	11.968	12.185
1.75	13.457	12.501	11.469	10.976	11.192	11.39	11.635	11.97	12.185
1.833	13.45	12.492	11.46	10.978	11.195	11.392	11.637	11.972	12.187
1.9166	13.443	12.485	11.451	10.98	11.197	11.392	11.639	11.972	12.187
2	13.438	12.478	11.444	10.98	11.199	11.393	11.642	11.973	12.187
2.083	13.431	12.473	11.437	10.981	11.202	11.393	11.642	11.975	12.187
2.1666	13.426	12.466	11.428	10.981	11.202	11.395	11.644	11.975	12.187
2.25	13.419	12.459	11.421	10.983	11.206	11.395	11.649	11.977	12.189
2.333	13.414	12.455	11.412	10.983	11.206	11.397	11.649	11.977	12.189
2.4166	13.409	12.45	11.407	10.985	11.208	11.397	11.651	11.979	12.191
2.5	13.403	12.443	11.399	10.985	11.209	11.4	11.651	11.98	12.191
2.5833	13.398	12.438	11.393	10.987	11.211	11.4	11.654	11.98	12.191
2.666	13.393	12.432	11.386	10.987	11.213	11.402	11.654	11.982	12.192
2.75	13.388	12.425	11.379	10.988	11.215	11.402	11.656	11.982	12.192
2.833	13.384	12.422	11.374	10.988	11.216	11.404	11.658	11.984	12.192
2.9166	13.379	12.415	11.367	10.988	11.218	11.404	11.66	11.984	12.192
3	13.375	12.411		10.99	11.22	11.405	11.661	11.986	12.192
4	13.328	12.359	11.302	10.995	11.234	11.416	11.679	11.996	12.199

	Sample 4X-03 Load Cycle			Sample 4X-03 Unload Cycle					
Time (minutes)	1536 kPa	3072 kPa	6144 kPa	1536 kPa	384 kPa (high)	384 kPa (low)	96 kPa	24 kPa	6 kPa
5	13.293	12.315	11.253	11.001	11.248	11.425	11.695	12.005	12.205
6	13.265	12.287	11.216	11.006	11.257	11.432	11.709	12.015	12.21
7	13.244	12.262	11.187	11.008	11.265	11.439	11.723	12.024	12.215
8	13.225	12.24	11.16	11.01	11.273	11.446	11.733	12.031	12.221
9	13.209	12.222	11.141	11.011	11.28	11.451	11.745	12.04	12.224
10	13.196	12.207	11.122	11.011	11.285	11.457	11.756	12.047	12.229
11	13.184	12.192	11.108	11.011	11.288	11.462	11.765	12.054	12.233
12	13.172	12.18	11.095	11.015	11.294	11.465	11.775	12.061	12.238
13	13.161	12.171	11.085	11.013	11.297	11.47	11.784	12.066	12.243
14	13.154	12.161	11.074	11.015	11.302	11.472	11.793	12.073	12.247
15	13.146	12.152	11.066	11.015	11.302	11.477	11.8	12.08	12.25
16	13.139	12.143	11.057	11.017	11.306	11.479	11.807	12.085	12.254
17	13.134	12.136	11.052	11.017	11.307	11.483	11.814	12.092	12.259
18	13.126	12.129	11.043	11.018	11.311	11.486	11.823	12.096	12.262
19	13.121	12.122	11.038	11.018	11.311	11.488	11.828	12.101	12.266
20	13.116	12.119	11.032	11.018	11.314	11.491	11.833	12.106	12.269
21	13.11	12.112	11.026	11.018	11.316		11.84	12.112	12.273
22	13.105	12.107	11.022	11.018	11.318		11.845	12.117	12.275
23	13.102	12.103	11.017	11.02	11.32		11.852	12.122	12.278
24	13.098	12.098	11.011	11.018	11.32		11.858	12.126	12.282
25	13.093	12.094	11.008	11.02	11.321		11.863	12.131	12.285
26	13.093	12.089	11.004	11.02	11.323		11.867	12.135	12.289
27	13.086	12.085	11.001	11.02	11.323		11.872	12.14	12.292
28	13.084	12.082	10.999	11.02	11.325		11.877	12.143	12.294
29	13.081	12.078	10.994	11.02	11.327		11.881	12.147	12.299
30	13.077	12.077	10.994	11.02	11.327		11.886	12.152	12.303
31	13.074	12.071	10.988	11.022	11.327				
32	13.072	12.07	10.987	11.022	11.328				
33	13.069	12.066	10.983	11.022	11.33				
34	13.067	12.063	10.981	11.022	11.33				
35	13.063	12.061	10.98	11.022	11.33				
36	13.062	12.059	10.976						
37	13.06	12.056	10.978						
38	13.058	12.054	10.973						
39	13.055	12.051	10.971						
40	13.053	12.049	10.969						
41	13.051	12.047	10.968						
42	13.049	12.044	10.968						

Time (minutes)	Sample 4X-03 Load Cycle			Sample 4X-03 Unload Cycle					
	1536 kPa	3072 kPa	6144 kPa	1536 kPa	384 kPa (high)	384 kPa (low)	96 kPa	24 kPa	6 kPa
43	13.048	12.042	10.966						
44	13.046	12.04	10.964						
45	13.044	12.04	10.962						
46	13.04	12.037	10.961						
47	13.04	12.033	10.959						
48	13.039	12.033	10.957						
49	13.035	12.031	10.957						
50	13.035	12.029	10.955						
51	13.033	12.028							
52	13.032	12.024							
53	13.03	12.022							
54	13.028	12.021							
55	13.026	12.019							
56	13.026								
57	13.025								
58	13.023								
59	13.019								
60	13.019		10.94						
61									
62									
63									
64									
65									
66									
67									
68									
69									
70			10.934						
71									
72									
73									
74									
75									
76									
77									
78									
79									
80			10.925						

	Sample 4X-03 Load Cycle			Sample 4X-03 Unload Cycle					
Time (minutes)	1536 kPa	3072 kPa	6144 kPa	1536 kPa	384 kPa	384 kPa	96 kPa	24 kPa	6 kPa
					(high)	(low)			
81									
82									
85									
87									
90			10.918						
92									
97									
95									
100			10.91						
105									
110			10.904						
115									
120			10.883						
125									
130			10.875						
135									
140			10.866						
144									
150			10.861						
160			10.856						
170			10.852						
180			10.85						
190			10.848						
200			10.847						
210			10.843						
220			10.845						

Time	Sample 56X-02 Load Cycle							
(minutes)	6 kPa	12 kPa	24 kPa	48 kPa	96 kPa	192 kPa	384 kPa (high)	384 kPa (low)
0	19.091	18.047	18.064	18.604	17.922	17.528	17.118	16.654
0.083	18.536	18.04	18.049	17.963	17.756	17.418	17.055	16.671
0.16666	18.352	18.034	18.04	17.905	17.698	17.369	16.967	16.524
0.25	18.275	18.034	18.036	17.882	17.672	17.339	16.932	16.494
0.3333	18.231	18.147	18.033	17.87	17.654	17.32	16.909	16.473
0.4166	18.203	18.14	18.029	17.863	17.642	17.306	16.89	16.456
0.5	18.183	18.138	18.029	17.854	17.633	17.293	16.875	16.44
0.58333	18.169	18.138	18.026	17.849	17.626	17.285	16.862	16.428
0.666	18.157	18.136	18.024	17.845	17.621	17.276	16.852	16.417
0.75	18.15	18.136	18.024	17.84	17.616	17.269	16.841	16.407
0.833	18.143	18.135	18.022	17.838	17.61	17.262	16.832	16.394
0.9166	18.136	18.135	18.022	17.835	17.607	17.256	16.825	16.387
1	18.131	18.135	18.021	17.833	17.605	17.251	16.818	16.379
1.083	18.128	18.135	18.021	17.83	17.602	17.248	16.811	16.372
1.1666	18.124	18.133	18.019	17.828	17.6	17.244	16.806	16.365
1.25	18.121	18.133	18.019	17.828	17.596	17.241	16.801	16.356
1.3333	18.117	18.133	18.017	17.826	17.595	17.237	16.796	16.351
1.4166	18.115	18.131	18.017	17.824	17.593	17.234	16.792	16.344
1.5	18.113	18.131	18.015	17.823	17.591	17.23	16.787	16.338
1.5833	18.11	18.131	18.015	17.823	17.589	17.229	16.784	16.333
1.666	18.108	18.131	18.015	17.821	17.588	17.227	16.778	16.328
1.75	18.108	18.131	18.013	17.819	17.588	17.223	16.775	16.322
1.833	18.105	18.131	18.013	17.817	17.586	17.22	16.771	16.317
1.9166	18.105	18.131	18.013	17.819	17.584	17.22	16.768	16.312
2	18.103	18.131	18.013	17.817	17.584	17.218	16.764	16.309
2.083	18.103	18.131	18.012	17.816	17.582	17.216	16.761	16.305
2.1666	18.101	18.129	18.012	17.816	17.581	17.215	16.759	16.3
2.25	18.099	18.129	18.012	17.814	17.581	17.211	16.757	16.296
2.333	18.099	18.129	18.012	17.814	17.579	17.211	16.755	16.293
2.4166	18.098	18.129	18.01	17.814	17.577	17.209	16.755	16.289
2.5	18.098	18.129	18.01	17.812	17.577	17.208	16.75	16.286
2.5833	18.096	18.129	18.01	17.812	17.577	17.206	16.746	16.282
2.666	18.096	18.128	18.01	17.812	17.577	17.206	16.745	16.279
2.75	18.094	18.129	18.01	17.81	17.575	17.204	16.743	16.275
2.833	18.094	18.128	18.01	17.81	17.575	17.202	16.741	16.274
2.9166	18.094	18.129	18.01	17.81	17.574	17.202	16.74	16.27
3	18.092	18.128	18.008	17.81	17.574	17.201	16.738	16.268
4	18.084	18.126	18.005	17.805	17.568	17.19	16.72	16.238

Time (minutes)	Sample 56X-02 Load Cycle							
	6 kPa	12 kPa	24 kPa	48 kPa	96 kPa	192 kPa	384 kPa (high)	384 kPa (low)
5	18.078	18.089	18.003	17.803	17.563	17.181	16.708	16.219
6	18.077	18.089	17.999	17.798	17.56	17.174	16.699	16.204
7	18.075	18.084	17.998	17.796	17.556	17.171	16.691	16.193
8	18.07	18.084	17.998	17.793	17.555	17.167	16.685	16.183
9	18.068	18.084	17.994	17.793	17.549	17.162	16.68	16.176
10	18.066	18.084	17.994	17.789	17.548	17.158	16.676	16.168
11	18.066	18.082	17.993	17.788	17.544	17.157	16.673	16.161
12	18.064	18.082	17.989	17.788	17.544	17.153	16.669	16.158
13	18.064	18.082	17.989	17.784	17.544	17.151	16.666	16.152
14	18.063	18.082	17.987	17.784	17.541	17.15	16.662	16.149
15	18.061	18.08	17.987	17.782	17.537	17.146	16.661	16.145
16	18.059	18.08	17.986	17.782	17.537	17.144	16.659	16.142
17	18.058	18.08	17.986	17.781	17.535	17.144	16.655	16.139
18	18.058	18.078	17.986	17.781	17.535	17.141	16.654	16.137
19	18.058	18.078	17.984	17.781	17.534	17.141	16.652	16.133
20	18.056	18.078	17.984	17.779	17.534	17.139	16.65	16.132
21	18.056	18.075	17.982	17.777	17.532	17.137	16.648	16.13
22	18.054	18.075	17.98	17.777	17.532	17.136	16.647	16.128
23	18.054	18.075	17.982	17.777	17.53	17.134	16.645	16.126
24	18.052	18.075	17.979	17.775	17.53	17.134	16.643	16.125
25	18.054	18.075	17.98	17.775	17.528	17.132	16.641	16.123
26	18.052	18.073	17.979	17.775	17.528	17.132	16.64	16.119
27	18.052	18.073	17.977	17.774	17.527	17.131	16.64	16.119
28	18.051	18.073	17.977	17.774	17.527	17.129	16.638	16.118
29	18.051	18.073	17.977	17.772	17.527	17.127	16.636	16.116
30	18.051	18.073	17.977	17.772	17.525	17.127	16.635	16.116
31	18.051	18.071	17.977	17.772	17.525	17.125	16.635	16.114
32	18.049	18.071	17.975	17.772	17.523	17.125	16.633	16.112
33	18.049	18.071	17.975	17.77	17.523	17.124	16.633	16.111
34	18.047	18.071	17.975	17.77	17.523	17.124	16.631	16.111
35	18.047	18.071	17.973	17.77	17.521	17.122	16.631	16.111
36				17.768	17.521	17.122	16.629	16.109
37					17.521	17.122	16.629	16.105
38					17.519	17.122	16.628	16.105
39					17.519	17.118	16.628	16.104
40					17.519	17.12	16.628	16.104

	Sample 56X-02 Load Cycle				Sample 56X-02 Unload Cycle				
Time (minutes)	768 kPa	1536 kPa	3072 kPa	6144 kPa	1536 kPa	384 kPa	96 kPa	24 kPa	6 kPa
						(low)			
0	16.1	15.723	15.243	14.602	13.703	14.195	14.367	14.81	15.082
0.083	16.044	15.648	15.136	14.418	13.783	14.216	14.423	14.833	15.091
0.16666	16.023	15.609	15.086	14.37	13.817	14.221	14.435	14.839	15.091
0.25	16.009	15.59	15.059	14.339	13.826	14.225	14.444	14.842	15.091
0.3333	15.998	15.576	15.042	14.316	13.833	14.227	14.449	14.844	15.093
0.4166	15.99	15.564	15.026	14.299	13.838	14.23	14.454	14.845	15.093
0.5	15.981	15.553	15.012	14.281	13.841	14.234	14.456	14.847	15.093
0.58333	15.974	15.545	15	14.267	13.845	14.234	14.46	14.849	15.094
0.666	15.969	15.536	14.987	14.251	13.848	14.237	14.467	14.851	15.094
0.75	15.962	15.527	14.977	14.241	13.852	14.237	14.47	14.852	15.096
0.833	15.956	15.52	14.968	14.23	13.854	14.239	14.472	14.852	15.094
0.9166	15.951	15.515	14.957	14.218	13.855	14.243	14.474	14.854	15.096
1	15.948	15.508	14.949	14.207	13.857	14.243	14.476	14.854	15.096
1.083	15.942	15.503	14.942	14.199	13.859	14.245	14.479	14.856	15.096
1.1666	15.937	15.497	14.935	14.188	13.86	14.246	14.483	14.858	15.096
1.25	15.934	15.494	14.928	14.18	13.862	14.248	14.485	14.858	15.098
1.3333	15.93	15.488	14.921	14.171	13.864	14.25	14.488	14.859	15.098
1.4166	15.929	15.483	14.914	14.164	13.864	14.251	14.49	14.859	15.098
1.5	15.925	15.478	14.907	14.155	13.866	14.251	14.492	14.861	15.098
1.5833	15.921	15.474	14.903	14.148	13.867	14.253	14.493	14.861	15.098
1.666	15.918	15.471	14.896	14.141	13.867	14.255	14.497	14.863	15.098
1.75	15.914	15.467	14.891	14.136	13.869		14.499	14.863	15.1
1.833	15.911	15.464	14.886	14.128	13.871		14.5	14.865	15.098
1.9166	15.909	15.46	14.879	14.122	13.871		14.502	14.865	15.1
2	15.905	15.457	14.873	14.116	13.882		14.504	14.866	15.1
2.083	15.904	15.453	14.87	14.111	13.887		14.506	14.866	15.1
2.1666	15.902	15.45	14.865	14.106	13.89		14.507	14.868	15.1
2.25	15.898	15.448	14.859	14.101	13.892		14.509	14.868	15.1
2.333	15.897	15.445	14.856	14.095	13.894		14.511	14.87	15.1
2.4166	15.893	15.441	14.854	14.09	13.896		14.513	14.87	15.1
2.5	15.891	15.44	14.849	14.085	13.898		14.514	14.87	15.1
2.5833	15.888	15.438	14.845	14.081	13.899		14.518	14.872	15.101
2.666	15.888	15.434	14.842	14.076	13.901		14.518	14.872	15.101
2.75	15.884	15.431	14.835	14.071	13.901		14.519	14.873	15.101
2.833	15.883	15.429	14.833	14.067	13.901		14.521	14.873	15.101
2.9166	15.881	15.427	14.83	14.062	13.901		14.523	14.873	15.101
3	15.879	15.424	14.826	14.059	13.903		14.525	14.873	15.101
4	15.86	15.399	14.793	14.015	13.903	14.285	14.544	14.884	15.105

	Sample 56X-02 Load Cycle				Sample 56X-02 Unload Cycle				
Time (minutes)	768 kPa	1536 kPa	3072 kPa	6144 kPa	1536 kPa	384 kPa	96 kPa	24 kPa	6 kPa
						(low)			
5	15.846	15.381	14.765	13.983	13.903	14.288	14.556	14.887	15.107
6	15.834	15.369	14.746	13.957	13.905	14.297	14.569	14.894	15.108
7	15.825	15.357	14.73	13.936	13.905	14.3	14.579	14.901	15.112
8	15.818	15.348	14.716	13.918	13.905	14.307	14.591	14.905	15.113
9	15.809	15.34	14.703	13.905		14.313	14.6	14.91	15.115
10	15.806	15.333	14.695	13.892		14.318	14.609	14.916	15.117
11	15.802	15.327	14.686	13.883		14.322	14.618	14.921	15.119
12	15.797	15.322	14.679	13.875		14.325	14.626	14.924	15.12
13	15.792	15.317	14.672	13.866		14.329	14.633	14.93	15.122
14	15.788	15.311	14.667	13.859		14.332	14.64	14.933	15.124
15	15.785	15.308	14.662	13.852		14.334	14.649	14.937	15.124
16	15.781	15.304	14.656	13.847		14.339	14.653	14.94	15.126
17	15.779	15.301	14.653	13.841		14.341	14.66	14.944	15.127
18	15.776	15.299	14.647	13.836		14.343	14.665	14.947	15.129
19	15.774	15.296	14.646	13.833		14.346	14.67	14.95	15.131
20	15.772	15.292	14.64	13.829		14.35	14.676	14.954	15.133
21	15.771	15.29	14.639	13.824		14.35	14.681	14.957	15.133
22	15.769	15.287	14.635	13.822		14.351	14.684	14.961	15.134
23	15.766	15.285	14.631	13.819		14.355	14.689	14.963	15.136
24	15.764	15.283	14.63	13.815		14.355	14.695	14.966	15.136
25	15.764	15.28	14.626	13.812		14.358	14.698	14.968	15.14
26	15.76	15.278	14.624	13.808			14.702	14.971	15.14
27	15.76	15.277	14.623	13.806			14.705	14.975	15.141
28	15.757	15.275	14.619	13.803			14.709	14.977	15.143
29	15.757	15.273	14.619	13.803			14.714	14.98	15.145
30	15.755	15.273	14.618	13.799			14.716	14.982	15.145
31	15.755	15.271	14.614	13.797			14.719	14.986	15.147
32	15.753	15.27	14.614	13.794			14.723	14.987	15.148
33	15.751	15.268	14.612	13.794			14.726	14.989	15.148
34	15.75	15.266	14.609	13.79			14.728	14.993	15.15
35	15.75	15.264	14.609	13.79			14.73	14.994	15.152
36	15.748	15.264	14.607	13.787			14.733	14.996	15.154
37	15.748	15.263	14.605	13.787			14.737	15	15.154
38	15.748	15.261	14.604	13.787			14.739	15.001	15.155
39	15.746	15.261	14.604	13.783			14.74	15.003	15.157
40	15.742	15.259	14.602	13.782			14.744	15.005	15.155
41	15.744	15.259	14.6	13.78			14.746	15.007	15.157
42	15.742	15.257	14.598	13.778			14.747	15.01	15.157

Time	Sample 56X-02 Load Cycle				Sample 56X-02 Unload Cycle				
(minutes)	768 kPa	1536 kPa	3072 kPa	6144 kPa	1536 kPa	384 kPa	96 kPa	24 kPa	6 kPa
						(low)			
43	15.741	15.256	14.597	13.776			14.751	15.012	15.159
44	15.741	15.256	14.597	13.776			14.753	15.014	15.159
45	15.739	15.254	14.595	13.775			14.754	15.015	15.161
46	15.739			13.773			14.756	15.017	15.163
47	15.737			13.773			14.76	15.019	15.163
48	15.737			13.771			14.76	15.021	15.164
49	15.735			13.769			14.763	15.022	15.164
50	15.735			13.768			14.763	15.024	15.166
51				13.766			14.767	15.024	15.168
52				13.764			14.767	15.026	15.168
53				13.764			14.768	15.028	15.17
54				13.764			14.772	15.029	15.17
55				13.764			14.772	15.031	15.17
56				13.761			14.774	15.033	15.172
57				13.761			14.775	15.035	15.173
58				13.761			14.777	15.036	15.173
59				13.759			14.779	15.038	15.173
60				13.759			14.781	15.038	15.175
61							14.781	15.04	15.177
62							14.782	15.042	15.177
63							14.784		15.177
64							14.786		15.178
65							14.786		15.18
66							14.787		15.18
67							14.789	15.049	15.18
68							14.791		15.18
69							14.791		15.184
70				13.75			14.793		15.182
71							14.793		
72							14.794	15.054	
73							14.796		
74							14.798		
75							14.798		15.185
76							14.8		
77							14.8	15.059	
78							14.801		
79							14.803		
80				13.743			14.803		15.189

Time	Sample 56X-02 Load Cycle				Sample 56X-02 Unload Cycle				
(minutes)	768 kPa	1536 kPa	3072 kPa	6144 kPa	1536 kPa	384 kPa	96 kPa	24 kPa	6 kPa
						(low)			
81							14.805		
82								15.064	
85									15.192
87								15.07	
90									15.196
92								15.075	
97								15.078	
95				13.735					15.199
100								15.08	15.201
105									15.203
110				13.727					15.206
115									15.21
120									15.212
125				13.722					15.212
130									15.213
135									15.217
140									15.22
144									15.222

Time	Sample 39X-02 Load Cycle							
(minutes)	6 kPa	12 kPa	24 kPa	48 kPa	96 kPa	192 kPa	384 kPa	384 kPa
							(high)	(low)
0	19.168	18.261	18.231	18.166	18.094	17.954	17.761	17.532
0.083	18.655	18.255	18.212	18.133	18.024	17.856	17.63	17.504
0.16666	18.473	18.254	18.204	18.119	18.01	17.833	17.593	17.341
0.25	18.389	18.252	18.201	18.113	18.003	17.824	17.582	17.321
0.3333	18.346	18.25	18.199	18.111	17.998	17.819	17.577	17.313
0.4166	18.326	18.25	18.197	18.108	17.998	17.816	17.572	17.306
0.5	18.315	18.248	18.196	18.106	17.996	17.812	17.568	17.302
0.58333	18.31	18.248	18.194	18.106	17.993	17.81	17.567	17.299
0.666	18.304	18.247	18.194	18.103	17.991	17.809	17.565	17.297
0.75	18.301	18.248	18.192	18.103	17.991	17.807	17.563	17.295
0.833	18.299	18.247	18.192	18.101	17.989	17.805	17.562	17.294
0.9166	18.297	18.247	18.19	18.101	17.989	17.805	17.56	17.292
1	18.296	18.247	18.19	18.099	17.989	17.803	17.558	17.29
1.083	18.294	18.247	18.19	18.099	17.987	17.803	17.558	17.288
1.1666	18.292	18.247	18.19	18.099	17.987	17.802	17.556	17.288
1.25	18.29	18.247	18.19	18.099	17.986	17.802	17.556	17.287
1.3333	18.292	18.247	18.189	18.098	17.986	17.8	17.555	17.287
1.4166	18.29	18.245	18.189	18.098	17.986	17.8	17.555	17.285
1.5	18.289	18.247	18.189	18.098	17.984	17.798	17.553	17.285
1.5833	18.287	18.245	18.187	18.096	17.984	17.798	17.553	17.285
1.666	18.287	18.245	18.189	18.096	17.984	17.798	17.551	17.283
1.75	18.287	18.245	18.187	18.096	17.984	17.798	17.551	17.281
1.833	18.285	18.245	18.187	18.096	17.984	17.796	17.551	17.281
1.9166	18.285	18.245	18.187	18.094	17.982	17.796	17.551	17.281
2	18.285	18.245	18.187	18.094	17.982	17.795	17.549	17.281
2.083	18.285	18.245	18.185	18.094	17.982	17.795	17.549	17.28
2.1666	18.283	18.245	18.185	18.094	17.982	17.795	17.549	17.28
2.25	18.283	18.245	18.183	18.094	17.98	17.795	17.549	17.28
2.333	18.283	18.243	18.185	18.094	17.98	17.793	17.548	17.278
2.4166	18.283	18.243	18.185	18.094	17.98	17.793	17.548	17.278
2.5	18.283	18.245	18.183	18.092	17.98	17.793	17.548	17.278
2.5833	18.283	18.243	18.183	18.092	17.98	17.793	17.546	17.278
2.666	18.281	18.243	18.183	18.092	17.98	17.793	17.546	17.276
2.75	18.281	18.243	18.182	18.092	17.979	17.793	17.546	17.278
2.833	18.283	18.243	18.183	18.092	17.979	17.791	17.546	17.276
2.9166	18.281	18.243	18.183	18.092	17.979	17.791	17.546	17.276
3	18.281	18.243	18.182	18.091	17.979	17.791	17.544	17.274
4	18.28	18.241	18.18	18.089	17.975	17.787	17.54	17.271

	Sample 39X-02 Load Cycle							
Time (minutes)	6 kPa	12 kPa	24 kPa	48 kPa	96 kPa	192 kPa	384 kPa	384 kPa
							(high)	(low)
5	18.278	18.241	18.18	18.089	17.975	17.786	17.539	17.267
6	18.278	18.24	18.178	18.087	17.973	17.784	17.537	17.265
7	18.274	18.24	18.176	18.085	17.972	17.782	17.535	17.264
8	18.273	18.24	18.175	18.085	17.97	17.78	17.532	17.26
9	18.271	18.238	18.175	18.084	17.968	17.779	17.53	17.26
10	18.271	18.238	18.173	18.084	17.968	17.779	17.53	17.258
11	18.269	18.236	18.173	18.085	17.966	17.777	17.528	17.256
12	18.269	18.236	18.173	18.082	17.966	17.775	17.528	17.255
13	18.269	18.236	18.171	18.082	17.966	17.775	17.527	17.253
14	18.269	18.236	18.173	18.082	17.965	17.775	17.527	17.251
15	18.268	18.234	18.171	18.08	17.965	17.774	17.525	17.249
16	18.269	18.234	18.171	18.08	17.963	17.774	17.527	17.251
17	18.266	18.234	18.171	18.08	17.963	17.774	17.523	17.249
18	18.268	18.233	18.171	18.08	17.963	17.772		17.249
19	18.266	18.233	18.169	18.08	17.963	17.772		17.248
20	18.266	18.233	18.169	18.078	17.961	17.77		17.248
21	18.264	18.231	18.169	18.078	17.961	17.77		17.246
22	18.264	18.231	18.169	18.077	17.961	17.77		17.246
23	18.264	18.231	18.169	18.077	17.959	17.768		17.246
24	18.264	18.231	18.169	18.077	17.959	17.768		17.244
25	18.264	18.231	18.169	18.077	17.959	17.768		17.244
26	18.262		18.169	18.077	17.959	17.768		17.242
27	18.262		18.169	18.077	17.959	17.768		17.242
28	18.262		18.169	18.077	17.959	17.766		17.242
29	18.262		18.168	18.075	17.958	17.766		17.242
30	18.262		18.168	18.075	17.958	17.766		17.241
31	18.262			18.075	17.958	17.766		17.241
32	18.262			18.075	17.959	17.765		17.241
33	18.261			18.075	17.956	17.765		17.241
34	18.262			18.075	17.956	17.765		17.239
35	18.261			18.075	17.958	17.765		17.239
36	18.261			18.075	17.958	17.765		17.237
37	18.261			18.075	17.956	17.765		17.239
38	18.262			18.073	17.956	17.765		17.237
39				18.075	17.956	17.765		17.239
40				18.073	17.954	17.763		17.239
41					17.954	17.763		
42					17.954	17.763		

Time	Sample 39X-02 Load Cycle							
(minutes)	6 kPa	12 kPa	24 kPa	48 kPa	96 kPa	192 kPa	384 kPa (high)	384 kPa (low)
43					17.954	17.763		
44					17.954	17.761		
45					17.954	17.761	17.512	
46							17.512	
47							17.512	
48							17.512	
49							17.512	
50							17.51	
51							17.509	
52							17.51	
53							17.51	
54							17.51	
55							17.509	
56							17.509	
57							17.509	
58							17.509	
59							17.509	
60							17.509	

Time	Sample 39X-02 Load Cycle				Sample 39X-02 Unload Cycle				
(minutes)	768 kPa	1536 kPa	3072 kPa	6144 kPa	1536 kPa	384 kPa	96 kPa	24 kPa	6 kPa
						(low)			
0	17.237	17.036	16.743	16.291	15.793	16.158	16.279	16.547	16.666
0.083	17.148	16.889	16.58	16.099	15.89	16.175	16.34	16.58	16.673
0.16666	17.124	16.846	16.494	16.028	15.9	16.193	16.354	16.583	16.675
0.25	17.113	16.831	16.461	15.995	15.904	16.198	16.363	16.587	16.675
0.3333	17.108	16.824	16.444	15.972	15.909	16.202	16.368	16.589	16.673
0.4166	17.104	16.818	16.431	15.955	15.911	16.205	16.373	16.591	16.677
0.5	17.1	16.815	16.424	15.939	15.912	16.207	16.379	16.592	16.677
0.58333	17.099	16.811	16.417	15.929	15.916	16.21	16.382	16.594	16.677
0.666	17.097	16.808	16.412	15.918	15.918	16.212	16.386	16.594	16.677
0.75	17.095	16.806	16.408	15.911	15.918	16.214	16.389	16.596	16.677
0.833	17.092	16.804	16.405	15.904	15.921	16.216	16.393	16.598	16.677
0.9166	17.092	16.803	16.401	15.897	15.919	16.217	16.396	16.598	16.677
1	17.09	16.801	16.398	15.891	15.923	16.219	16.398	16.599	16.677
1.083	17.088	16.799	16.396	15.886	15.923	16.221	16.401	16.599	16.678
1.1666	17.086	16.798	16.394	15.883	15.925	16.223	16.403	16.601	16.678
1.25	17.086	16.798	16.393	15.879	15.925	16.223	16.405	16.601	16.677
1.3333	17.085	16.796	16.391	15.874	15.925	16.224	16.408	16.601	16.677
1.4166	17.085	16.796	16.389	15.871	15.927	16.224	16.41	16.603	16.678
1.5	17.083	16.792	16.387	15.867	15.928	16.226	16.412	16.603	16.678
1.5833	17.083	16.792	16.386	15.865	15.927	16.228	16.414	16.605	16.678
1.666	17.081	16.792	16.386	15.864	15.928	16.228	16.415	16.603	16.678
1.75	17.081	16.791	16.384	15.862	15.928	16.23	16.417	16.605	16.678
1.833	17.081	16.791	16.382	15.858	15.928	16.231	16.419	16.605	16.678
1.9166	17.079	16.789	16.38	15.857	15.93	16.231	16.421	16.605	16.678
2	17.079	16.789	16.38	15.855	15.93	16.233	16.423	16.606	16.68
2.083	17.078	16.789	16.379	15.853	15.928	16.233	16.424	16.606	16.678
2.1666	17.079	16.787	16.377	15.853	15.928	16.233	16.424	16.606	16.678
2.25	17.078	16.787	16.377	15.851	15.928	16.235	16.428	16.606	16.678
2.333	17.078	16.785	16.377	15.85	15.928	16.235	16.428	16.608	16.68
2.4166	17.078	16.785	16.375	15.848	15.932	16.237	16.43	16.606	16.678
2.5	17.076	16.785	16.375	15.846	15.93	16.237	16.431	16.608	16.68
2.5833	17.076	16.785	16.373	15.844	15.93	16.238	16.433	16.608	16.68
2.666	17.076	16.784	16.373	15.844	15.932	16.238	16.433	16.61	16.68
2.75	17.075	16.782	16.373	15.843	15.932	16.24	16.435	16.61	16.68
2.833	17.074	16.784	16.372	15.839	15.932	16.24	16.437	16.61	16.68
2.9166	17.074	16.782	16.37	15.839	15.932	16.24	16.437	16.61	16.68
3	17.072	16.782	16.37	15.837	15.932	16.24	16.438	16.61	16.68
4	17.069	16.776	16.365	15.827	15.934	16.245	16.451	16.614	16.682

	Sample 39X-02 Load Cycle				Sample 39X-02 Unload Cycle				
Time (minutes)	768 kPa	1536 kPa	3072 kPa	6144 kPa	1536 kPa	384 kPa	96 kPa	24 kPa	6 kPa
						(low)			
5	17.066	16.773	16.36	15.82	15.934	16.251	16.459	16.617	16.682
6	17.064	16.769	16.354	15.814	15.935	16.252	16.466	16.621	16.683
7	17.06	16.768	16.353	15.809	15.935	16.256	16.473	16.622	16.685
8	17.059	16.766	16.349	15.806	15.935	16.258	16.478	16.624	16.685
9	17.057	16.764	16.346	15.802	15.937	16.259	16.482	16.626	16.687
10	17.055	16.762	16.344	15.799	15.937	16.261	16.485	16.628	16.687
11	17.053	16.761	16.342	15.797	15.937	16.263	16.489	16.628	16.687
12	17.052	16.759	16.34	15.793	15.937	16.263	16.492	16.629	16.689
13	17.05	16.757	16.338	15.792	15.937	16.265	16.494	16.631	16.689
14	17.05	16.757	16.336	15.79	15.937	16.265	16.496	16.631	16.689
15	17.048	16.755	16.335	15.788	15.937	16.267	16.498	16.633	16.691
16	17.046	16.753	16.333	15.786	15.939	16.267	16.501	16.635	16.691
17	17.046	16.753	16.331	15.785	15.939	16.268	16.503	16.635	16.691
18	17.045	16.752	16.329	15.785	15.937	16.268	16.505	16.635	16.693
19	17.045	16.752	16.329	15.783	15.939	16.268	16.506	16.636	16.693
20	17.043	16.75	16.328	15.781	15.939	16.27	16.506	16.636	16.696
21	17.043	16.75	16.328	15.779	15.939	16.27	16.508	16.638	16.696
22	17.041	16.748	16.326	15.779	15.939	16.27	16.508	16.638	16.696
23	17.041	16.747	16.326	15.778	15.939	16.272	16.512	16.64	16.696
24	17.039	16.747	16.324	15.778	15.939	16.272	16.512	16.641	16.698
25	17.039	16.747	16.322	15.776	15.939	16.272	16.514	16.641	16.698
26	17.038	16.747	16.324	15.776	15.941	16.274	16.514	16.641	16.698
27	17.038	16.747	16.321	15.774	15.939	16.274	16.515	16.641	16.698
28	17.038	16.745	16.321	15.774	15.939	16.274	16.515	16.643	16.699
29	17.036	16.745	16.321	15.772	15.939	16.274	16.515	16.643	16.699
30	17.036	16.745	16.321	15.772	15.941	16.274	16.517	16.645	16.699
31	17.034	16.743	16.319	15.772	15.939	16.274	16.519	16.643	16.699
32	17.036	16.743	16.317	15.771	15.939	16.275	16.519	16.645	16.701
33	17.034	16.741	16.317	15.771	15.941	16.275	16.521	16.647	16.701
34	17.034	16.741	16.317	15.771	15.941	16.275	16.521	16.645	16.701
35	17.035	16.741	16.315	15.769	15.941	16.277	16.521	16.647	16.701
36	17.034	16.741	16.315	15.767	15.941		16.521	16.647	16.703
37	17.032	16.74	16.315	15.769	15.941		16.522	16.647	16.703
38	17.032	16.74	16.314	15.767	15.941		16.522	16.647	16.701
39	17.032	16.738	16.314	15.767	15.941		16.522	16.647	16.703
40	17.031	16.738	16.314	15.767	15.941		16.522	16.647	16.703
41	17.031	16.738	16.312	15.765			16.524	16.647	16.703
42	17.031		16.312	15.767			16.524	16.648	16.705

Time	Sample 39X-02 Load Cycle				Sample 39X-02 Unload Cycle				
(minutes)	768 kPa	1536 kPa	3072 kPa	6144 kPa	1536 kPa	384 kPa	96 kPa	24 kPa	6 kPa
						(low)			
43	17.031		16.312	15.765			16.524	16.65	16.703
44	17.029		16.31	15.765			16.526	16.65	16.703
45	17.029		16.31	15.765			16.526	16.652	16.705
46			16.309	15.757			16.526	16.652	16.705
47			16.31	15.753			16.526	16.652	16.706
48			16.309	15.753			16.528	16.652	16.706
49			16.309	15.751			16.528	16.652	16.705
50			16.309	15.749			16.528	16.652	16.708
51			16.307				16.528	16.652	16.708
52			16.307				16.528	16.654	16.708
53			16.307				16.53	16.654	16.706
54							16.53	16.654	16.708
55							16.53	16.654	16.708
56							16.531	16.655	16.708
57							16.531	16.655	16.71
58							16.53	16.655	16.71
59							16.531	16.655	16.71
60				15.739			16.531	16.655	16.71
61							16.531	16.657	16.712
62							16.531	16.655	16.71
63							16.531	16.655	16.712
64							16.531	16.657	16.712
65							16.533	16.657	16.712
66							16.531	16.657	
67							16.533	16.657	
68							16.533	16.657	
69							16.535	16.659	
70				15.735			16.535	16.659	16.712
71							16.535	16.659	
72							16.535	16.659	
73							16.535	16.659	
74							16.536	16.659	
75							16.535	16.659	16.713
76							16.536	16.659	
77							16.536	16.661	
78							16.536	16.659	
79							16.536	16.659	
80				15.73			16.536	16.659	16.713

	Sample 39X-02 Load Cycle				Sample 39X-02 Unload Cycle				
Time (minutes)	768 kPa	1536 kPa	3072 kPa	6144 kPa	1536 kPa	384 kPa	96 kPa	24 kPa	6 kPa
						(low)			
81							16.536	16.661	
82									16.715
85				15.723					16.719
87									16.717
90				15.72					16.719
92									16.72
97									16.72
95									16.72
100									16.724
105									16.724
110				13.727					15.206
115									15.21
120									15.212

Atlantic Geoscience Centre
Marine Geomechanics Laboratory
Consolidation Data Sheet 1 of 3

Sample Identification

Cruise ID:	ODP Leg 146	Description of Sample:	olive-green clay,silty
Borehole/Core:	892D	Condition of Sample:	fractured when trim
Sample No:	4x03		pulling from sides
Depth:	53-57.5 cm	Consolidometer ID:	A
Date:	93/12/09	Double or Single Drainage:	double

Initial Water Content		**Final Water Content**	
Tare Id:	A1	Tare Id:	L6
Tare Weight (g):	1.579	Tare Weight (g):	1.567
Wet Wt. of Sample + Tare (g):	20.123	Wet Wt of Sample + Tare (g):	77.192
Dry Wt of Sample + Tare (g):	13.538	Dry Wt of Sample + Tare (g):	55.395
Salinity (ppt):	35.000	Salinity (ppt) :	35.000
Water Content (%):	58.223	Water Content (%):	42.588

Initial Void Ratio

Specific Gravity:	2.658	Initial Dial Reading (div):	2025.0
Diameter of Sample (cm):	6.200	Area of Sample (cm2):	30.191
Ht of Sample measured (cm):	1.878	Volume of Sample (cm3):	56.686
Wet Wt of Sample + Filters (g):	86.745	Bulk Density (g/cm3):	1.521
ditto + ring (g):	122.600	Unit Weight:	14.929
Wt of Ring (g):	36.376	Effective Unit Weight:	4.874
Wt of 2 Filter Papers (g):	0.521	Dry Wt of Solids (g):	54.495
Computed Wet Wt (g):	86.224	Computed Ht of Solids (cm):	0.663
Dry Wt of Sample + Filters (g):	53.828	Initial Height of Voids (cm):	1.215
Computed Dry Wt (g):	53.307	Initial Void Ratio:	1.832

Loading Information

Backpressure (kPa):	300.000	DCDT Calibration (mm/mv):	375.900
Dial Reading at Contact (div):	1981.000	DCDT Calibration (mm):	10.756
DCDT at Contact (mm):	18.327	XDCR Calibration (kPa/mv):	103404.000
Dial Rdg after Saturation (div):	2025.000	XDCR Calibration (kPa):	-31.800
DCDT after Saturation (mm):	18.776	System A or B?:	A

Atlantic Geoscience Centre
Marine Geomechanics Laboratory
Consolidation Data Sheet 2 of 3

Sample Identification

Cruise ID: ODP Leg 146
Borehole/Core 892D

Sample No: 4x03
Core Depth: 53-57.5 cm
mbsf Depth: 30.45

Stress Level (kPa)	Load Pressure (kPa)	High Low?	DCDT (mm)	Dial Reading (div)	Sample H end of load (mm)	Comment
0	0.0		18.776	2025	18.776	9-Dec
6	99.6	low	17.287	1876	17.287	15-Dec
12	109.6	low	17.216	1869	17.216	
24	129.6	low	17.055	1853.5	17.055	
48	169.7	low	16.871	1834.7	16.871	
96	249.7	low	16.449	1792.5	16.449	
192	409.9	low	15.898	1738	15.898	
384	730.1	low	15.252	1672.5	15.252	
384	131.7	high				
768	200.8	high	13.841	1532.5	13.841	19-Dec
1536	339.2	high	13.019	1449	13.019	20-Dec
3072	615.9	high	12.019	1350	12.019	22-Dec
6144	1169.0	high	10.845	1232.5	10.845	5-Jan
1536	339.2	high	11.022	1249.5	11.022	12-Jan
384	131.7	high	11.33	1281	11.33	
384	730.1	low	11.491	1297	11.491	
96	249.7	low	11.886	1336	11.886	
24	129.6	low	12.152	1362	12.152	
6	99.6	low	12.303	1376.5	12.303	

Start	DCDT	dial	Start	DCDT	dial
6	18.776	2025.000	1536	13.836	1531.500
12	17.287	1876.000	3072	13.009	1448.000
24	17.213	1869.000	6144	12.015	1350.000
48	17.060	1853.500	1536u	10.784	1226.000
96	16.871	1834.500	384hu	11.024	1249.500
192	16.447	1792.500	384lu	11.332	1281.000
384lo	15.891	1737.000	96u	11.504	1297.000
384hi			24u	11.903	1336.500
768	15.529	1671.500	6u	12.159	1362.000

Atlantic Geoscience Centre
Marine Geomechanics Laboratory
Consolidation Data Sheet 3 of 3

Sample Identification

Cruise ID:	ODP Leg 146	Sample No:	4x03
Borehole/Core:	892D	Core Depth:	53-57.5 cm
		mbsf Depth:	30.45

Load increment (kPa)	H90 by sqrt (mm)	H100 by sqrt (mm)	Delta H (mm)	Delta e	e at end of load	t90 (sec)	Cv from t90 (cm2/sec)	mv coefficient of volume change (per kPa)	K (hydraulic conductivity) (cm/sec)
					1.832				
6	17.524	17.385	1.391	0.210	1.622	98.994	0.0070	1.235E-02	8.481E-06
12	17.248	17.244	0.043	0.007	1.616	114.51	0.0055	4.154E-04	2.249E-07
24	17.140	17.132	0.081	0.012	1.604	87.42	0.0072	3.898E-04	2.734E-07
48	16.933	16.919	0.141	0.021	1.582	114.51	0.0053	3.406E-04	1.786E-07
96	16.581	16.549	0.322	0.049	1.534	175.692	0.0034	3.921E-04	1.296E-07
192	16.063	16.020	0.427	0.064	1.469	179.6982	0.0031	2.646E-04	8.070E-08
384	15.463	15.415	0.476	0.072	1.398	171.7308	0.0030	1.513E-04	4.490E-08
768	14.260	14.119	1.410	0.213	1.185	213.3744	0.0022	2.310E-04	4.948E-08
1536	13.369	13.317	0.519	0.078	1.107	187.848	0.0021	4.664E-05	9.519E-09
3072	12.316	12.239	0.770	0.116	0.991	299.682	0.0011	3.589E-05	3.970E-09
6144	11.307	11.228	0.787	0.119	0.872	231.294	0.0012	1.941E-05	2.357E-09
1536	10.970	10.991	-0.207	-0.031	0.903	81.867	0.0031	3.614E-06	1.088E-09
384	11.228	11.251	-0.227	-0.034	0.937	217.7868	0.0012	1.560E-05	1.847E-09
96	11.783	11.814	-0.310	-0.047	1.008	782.82	0.0004	8.280E-05	2.990E-09
24	12.102	12.124	-0.221	-0.033	1.041	1155.24	0.0003	2.307E-04	5.995E-09
6	12.267	12.279	-0.120	-0.018	1.059	1155.24	0.0003	4.927E-04	1.324E-08

			Comments:
Cc:	0.420		Cc:
Cr:	0.065		Cr:
P'c:	195.000	Corr. OCR	P'c:
OCR:	1.3	1.0	OCR:
P'o	195		P'o

Atlantic Geoscience Centre
Marine Geomechanics Laboratory
Consolidation Data Sheet 1 of 3

Sample Identification

Cruise ID:	ODP Leg 146	Description of Sample:	olive-green clay
Borehole/Core:	891B	Condition of Sample:	very stiff, brittle
Sample No:	39x02		highly fractured
Depth:	18-23 cm	Consolidometer ID:	A
Date:	94/02/07	Double or Single Drainage:	double

Initial Water Content		**Final Water Content**	
Tare Id:	B81	Tare Id:	B51
Tare Weight (g):	1.576	Tare Weight (g):	1.549
Wet Wt. of Sample + Tare (g):	54.617	Wet Wt of Sample + Tare (g):	113.147
Dry Wt of Sample + Tare (g):	44.394	Dry Wt of Sample + Tare (g):	90.168
Salinity (ppt):	35.000	Salinity (ppt) :	35.000
Water Content (%):	24.958	Water Content (%):	27.126

Initial Void Ratio

Specific Gravity:	2.738	Initial Dial Reading (div):	2064.0
Diameter of Sample (cm):	6.200	Area of Sample (cm2):	30.191
Ht of Sample measured (cm):	1.917	Volume of Sample (cm3):	57.867
Wet Wt of Sample + Filters (g):	110.446	Bulk Density (g/cm3):	1.900
ditto + ring (g):	146.009	Unit Weight:	18.646
Wt of Ring (g):	36.070	Effective Unit Weight:	8.591
Wt of 2 Filter Papers (g):	0.507	Dry Wt of Solids (g):	87.981
Computed Wet Wt (g):	109.939	Computed Ht of Solids (cm):	1.039
Dry Wt of Sample + Filters (g):	88.619	Initial Height of Voids (cm):	0.878
Computed Dry Wt (g):	88.112	Initial Void Ratio:	0.845

Loading Information

Backpressure (kPa):	300.000	DCDT Calibration (mm/mv):	375.900
Dial Reading at Contact (div):	2001.000	DCDT Calibration (mm):	10.756
DCDT at Contact (mm):	18.539	XDCR Calibration (kPa/mv):	103404.000
Dial Rdg after Saturation (div):	2064.000	XDCR Calibration (kPa):	-31.800
DCDT after Saturation (mm):	19.167	System A or B?:	A

Atlantic Geoscience Centre
Marine Geomechanics Laboratory
Consolidation Data Sheet 2 of 3

Sample Identification

Cruise ID: ODP Leg 146

Borehole/Core 891B

Sample No: 39x02

Core Depth: 18-23 cm

mbsf Depth: 296.61

Stress Level (kPa)	Load Pressure (kPa)	High Low?	DCDT (mm)	Dial Reading (div)	Sample H end of load (mm)	Comment
0	0.0		19.167	2064	19.167	9-Feb
6	99.6	low	18.261	1973.5	18.261	9-Feb 38 min
12	109.6	low	18.231	1970	18.231	9-Feb 25 min
24	129.6	low	18.168	1964	18.168	9-Feb 30 min
48	169.7	low	18.073	1954.5	18.073	9-Feb 40 min
96	249.7	low	17.954	1942	17.954	11-Feb 45 min
192	409.9	low	17.761	1923	17.761	11-Feb 45 min
384	730.1	low	17.509	1897	17.509	11-Feb 60 min
384	131.7	high	17.237	1870	17.237	11-Feb 40 min
768	200.8	high	17.029	1850	17.029	11-Feb 45 min
1536	339.2	high	16.738	1821	16.738	17-Feb 45 min
3072	615.9	high	16.307	1778.5	16.307	21-Feb 53 min
6144	1169.0	high	15.72	1721	15.72	23-Feb 100 min
1536	339.2	high	15.941	1742	15.941	26-Feb 40 min
384	131.7	high	16.156	1763	16.156	26-Feb 45 min
384	730.1	low	16.277	1775	16.277	26-Feb 35 min
96	249.7	low	16.538	1799	16.538	26-Feb 81 min
24	129.6	low	16.661	1813	16.661	27-Feb 81 min
6	99.6	low	16.724	1819	16.724	27-Feb 121 min

Start	DCDT	dial	Start	DCDT	dial	
6	19.168	2064.000	1536	17.036	1850.000	
12	18.261	1973.500	3072	16.743	1822.000	
24	18.231	1970.000	6144	16.291	1777.000	
48	18.168	1964.000	1536u	15.793	1727.000	
96	18.094	1956.000	384hu	15.941	1742.000	
192	17.954	1942.000	384lu	16.158	1763.000	
384lo	17.761	1923.000	96u	16.277	1775.000	
384hi	17.532	1900.000	24u	16.547	1802.500	
768	17.237	1870.000	6u	16.661	1813.000	

Atlantic Geoscience Centre
Marine Geomechanics Laboratory
Consolidation Data Sheet 3 of 3

Sample Identification

Cruise ID: ODP Leg 146
Borehole/Core: 891B
Sample No: 39x02
Core Depth: 18-23 cm
mbsf Depth: 296.61

Load increment (kPa)	H90 by sqrt (mm)	H100 by sqrt (mm)	Delta H (mm)	Delta e	e at end of load	t90 (sec)	Cv from t90 (cm2/sec)	mv coefficient of volume change (per kPa)	Load increment k (hydraulic conductivity) (cm/sec)
6	18.300	18.204	0.964	0.093	0.752	48.228	0.0153	8.386E-03	1.263E-05
12	18.247	18.245	0.016	0.001	0.751	63.936	0.0110	1.424E-04	1.544E-07
24	18.190	18.185	0.046	0.004	0.746	71.352	0.0099	2.087E-04	2.017E-07
48	18.098	18.090	0.078	0.007	0.739	81.864	0.0085	1.786E-04	1.492E-07
96	17.984	17.972	0.122	0.012	0.727	102.006	0.0068	1.410E-04	9.346E-08
192	17.797	17.780	0.174	0.017	0.710	105.066	0.0064	1.013E-04	6.400E-08
384	17.551	17.528	0.233	0.022	0.688	108.168	0.0061	6.840E-05	4.094E-08
768	17.080	17.063	0.174	0.017	0.645	108.168	0.0058	2.632E-05	1.488E-08
1536	16.792	16.765	0.271	0.026	0.619	96.024	0.0063	2.066E-05	1.278E-08
3072	16.379	16.339	0.404	0.039	0.580	127.734	0.0045	1.566E-05	6.976E-09
6144	15.860	15.812	0.479	0.046	0.534	111.318	0.0049	9.500E-06	4.573E-09
1536	15.930	15.945	-0.152	-0.015	0.548	127.734	0.0042	2.074E-06	8.502E-10
384	16.123	16.143	-0.202	-0.019	0.568	131.142	0.0042	1.091E-05	4.455E-09
96	16.436	16.454	-0.177	-0.017	0.593	175.692	0.0032	3.747E-05	1.188E-08
24	16.606	16.613	-0.066	-0.006	0.599	124.362	0.0047	5.503E-05	2.530E-08
6	16.677	16.679	-0.018	-0.002	0.601	52.4916	0.0112	5.946E-05	6.546E-08

			Comments:
Cc:	0.130		Cc:
Cr:	0.028		Cr:
P'c:	510.000	Corr. OCR	P'c:
OCR:	0.20	0.17	OCR:
P'o	3063		P'o

Atlantic Geoscience Centre
Marine Geomechanics Laboratory
Consolidation Data Sheet 1 of 3

Sample Identification

Cruise ID:	ODP Leg 146	Description of Sample:	olive-green clay
Borehole/Core:	891B	Condition of Sample:	stiff, fractured
Sample No:	56x02		pulling from sides
Depth:	65-69cm	Consolidometer ID:	A
Date:	94/01/14	Double or Single Drainage:	double

Initial Water Content / **Final Water Content**

Tare Id:	L4	Tare Id:	A65
Tare Weight (g):	1.584	Tare Weight (g):	1.537
Wet Wt. of Sample + Tare (g):	51.740	Wet Wt of Sample + Tare (g):	101.894
Dry Wt of Sample + Tare (g):	38.888	Dry Wt of Sample + Tare (g):	78.264
Salinity (ppt):	35.000	Salinity (ppt) :	35.000
Water Content (%):	36.153	Water Content (%):	32.275

Initial Void Ratio

Specific Gravity:	2.727	Initial Dial Reading (div):	2055.0
Diameter of Sample (cm):	6.200	Area of Sample (cm2):	30.191
Ht of Sample measured (cm):	1.909	Volume of Sample (cm3):	57.622
Wet Wt of Sample + Filters (g):	102.497	Bulk Density (g/cm3):	1.772
ditto + ring (g):	138.603	Unit Weight:	17.388
Wt of Ring (g):	36.515	Effective Unit Weight:	7.333
Wt of 2 Filter Papers (g):	0.409	Dry Wt of Solids (g):	74.980
Computed Wet Wt (g):	102.088	Computed Ht of Solids (cm):	0.889
Dry Wt of Sample + Filters (g):	76.727	Initial Height of Voids (cm):	1.020
Computed Dry Wt (g):	76.318	Initial Void Ratio:	1.147

Loading Information

Backpressure (kPa):	300.000	DCDT Calibration (mm/mv):	375.900
Dial Reading at Contact (div):	1995.000	DCDT Calibration (mm):	10.756
DCDT at Contact (mm):	18.483	XDCR Calibration (kPa/mv):	103404.000
Dial Rdg after Saturation (div):	2055.000	XDCR Calibration (kPa):	-31.800
DCDT after Saturation (mm):	19.086	System A or B?:	A

Atlantic Geoscience Centre
Marine Geomechanics Laboratory
Consolidation Data Sheet 2 of 3

Sample Identification

Cruise ID: ODP Leg 146
Borehole/Core 891B

Sample No: 56x02
Core Depth: 65-69cm
mbsf Depth: 447.23

Stress Level (kPa)	Load Pressure (kPa)	High Low?	DCDT (mm)	Dial Reading (div)	Sample H end of load (mm)	Comment
0	0.0		19.086		19.086	
6	99.6	low	18.047	1951	18.047	17-Jan
12	109.6	low	18.071	1945	18.071	
24	129.6	low	17.973	1936	17.973	
48	169.7	low	17.768	1920	17.768	18-Jan
96	249.7	low	17.519	1895.5	17.519	21-Jan 40 min
192	409.9	low	17.12	1855	17.12	40 min
384	730.1	low	16.626	1806	16.626	40 min
384	131.7	high	16.104	1754	16.104	
768	200.8	high	15.735	1718	15.735	50 min
1536	339.2	high	15.254	1670	15.254	24-Jan 45 min
3072	615.9	high	14.595	1604	14.595	26-Jan 45 min
6144	1169.0	high	13.722	1516.5	13.722	30-Jan
1536	339.2	high	13.905	1537	13.905	2-Feb 20 min
384	131.7	high	14.195	1564.5	14.195	35 min
384	730.1	low	14.358	1581.5	14.358	25 min
96	249.7	low	14.805	1626	14.805	81 min
24	129.6	low	15.08	1654.5	15.08	100 min
6	99.6	low	15.222	1669	15.222	144 min
Start	DCDT	dial	Start	DCDT	dial	
6	19.091	2055.000	1536	15.723	1717.000	
12	18.047	1951.000	3072	15.243	1669.000	
24	18.064	1945.000	6144	14.602	1604.000	
48	17.973	1949.500	1536u	13.703	1517.500	
96	17.922	1936.000	384hu	13.913	1538.000	
192	17.528	1896.000	384lu	14.195	1565.000	
384lo	17.118	1855.000	96u	14.367	1582.000	
384hi	16.654	1806.000	24u	14.810	1626.500	
768	16.100	1754.000	6u	15.082	1654.500	

Atlantic Geoscience Centre
Marine Geomechanics Laboratory
Consolidation Data Sheet 3 of 3

Sample Identification

Cruise ID:	ODP Leg 146	Sample No:	56x02
Borehole/Core:	891B	Core Depth:	65-69cm
		mbsf Depth:	447.23

Load increment (kPa)	H90 by sqrt (mm)	H100 by sqrt (mm)	Delta H (mm)	Delta e	e at end of load	t90 (sec)	Cv from t90 (cm2/sec)	mv coefficient of volume change (per kPa)	K (hydraulic conductivity) change (cm/sec)
6	18.140	18.034	1.057	0.119	1.028	52.4916	0.0139	9.227E-03	1.260E-05
12									
24	18.018	18.013	0.051	0.006	1.023	76.518	0.0090	4.792E-04	4.238E-07
48	17.827	17.811	0.162	0.018	1.004	76.518	0.0089	3.760E-04	3.270E-07
96	17.593	17.556	0.366	0.041	0.963	84.612	0.0079	4.275E-04	3.300E-07
192	17.218	17.184	0.344	0.039	0.924	117.75	0.0054	2.056E-04	1.094E-07
384	16.748	16.707	0.411	0.046	0.878	148.914	0.0041	1.252E-04	5.060E-08
768	15.878	15.853	0.247	0.028	0.803	179.694	0.0030	3.947E-05	1.166E-08
1536	15.415	15.381	0.342	0.039	0.765	191.988	0.0027	2.780E-05	7.284E-09
3072	14.842	14.797	0.446	0.050	0.714	160.116	0.0030	1.849E-05	5.419E-09
6144	14.133	14.081	0.521	0.059	0.656	108.168	0.0040	1.113E-05	4.402E-09
1536	13.858	13.875	-0.172	-0.019	0.675	59.226	0.0068	2.539E-06	1.695E-09
384	14.100	14.121	-0.208	-0.023	0.699	167.814	0.0025	1.211E-05	2.929E-09
96	14.538	14.557	-0.190	-0.021	0.733	222.24	0.0020	4.336E-05	8.487E-09
24	14.857	14.862	-0.052	-0.006	0.739	61.5576	0.0076	4.709E-05	3.510E-08
6	15.093	15.094	-0.012	-0.001	0.740	19.2762	0.0250	4.393E-05	1.074E-07

			Comments:
Cc:	0.170		Cc:
Cr:	0.036		Cr:
P'c:	125.000	Corr. OCR	P'c:
OCR:	0.04	0.03	OCR:
P'o	4655		P'o